ABSTRACT

Title of dissertation: MODELING THE INFLUENCE OF PHASE
                           BOUNDARIES AND OXYGEN INTERSTITIALS
                           ON THE NUCLEATION AND GROWTH
                           OF DEFORMATION TWINS IN THE
                           ALPHA-PHASE OF TITANIUM ALLOYS

                           William Joseph Joost, Doctor of Philosophy, 2015

Dissertation directed by: Professor Sreeramamurthy Ankem
                           Professor Maija M. Kuklja
                           Department of Materials Science and Engineering

Twinning is an important deformation mechanism in many hexagonal close packed metals, including α-titanium alloys. However, the processes of twin nucleation, growth, and interaction with other defects are not well understood. Further, many aspects of deformation twinning are difficult to interrogate experimentally owing to the small time and length scales of the governing mechanisms. In this study we apply a combination of theoretical and computational materials science techniques, leveraged with experimental data, to quantify the effects of α-β phase boundaries and oxygen interstitials on twin nucleation, twin growth, and ultimately mechanical behavior in titanium alloys.

Combined results from finite element method and analytical dislocation modeling demonstrate that elastic and plastic interaction stresses across the interface between the α- and β-phases are responsible for the experimentally observed anisotropy in the deformation behavior of dual-phase alloys. Interaction stresses also promote

slip and twinning at up to 30% lower applied stress than predicted from Schmid's Law, significantly affecting performance in many applications. The complex interactions of phase boundaries, dislocations, and deformation twins modify the preferred deformation mechanism and promote twinning for some loading orientations.

In order to quantify the interaction between oxygen interstitials and $(10\bar{1}2)$ twin boundaries, we employ atomistic simulations using a newly developed modified embedded atom method potential and density functional theory. Our investigation reveals that a twin boundary alters interstitial formation energy by as much as 0.5 eV while also stabilizing a tetrahedral interstitial, which is unstable in the bulk. Further, the activation barriers for diffusion in the region near a twin are uniformly lower than in the bulk; an atom diffusing across the twin boundary moves through several paths with peak activation barriers more than 0.3 eV lower than for comparable diffusion far from the twin. Despite accelerated kinetics, oxygen diffusion still occurs much more slowly than twin growth, suggesting that oxygen interstitials contribute to experimentally observed time-dependent twinning.

Together, these results provide new insight while enabling predictive modeling and purposeful development of improved titanium alloys across a wide range of applications.

MODELING THE INFLUENCE OF PHASE BOUNDARIES AND
OXYGEN INTERSTITIALS ON THE NUCLEATION AND
GROWTH OF DEFORMATION TWINS IN THE ALPHA-PHASE
OF TITANIUM ALLOYS

by

William Joseph Joost

Dissertation submitted to the Faculty of the Graduate School of the
University of Maryland, College Park in partial fulfillment
of the requirements for the degree of
Doctor of Philosophy
2015

Advisory Committee:
Professor Sreeramamurthy Ankem, Chair
Professor Maija M. Kuklja, Co-chair
Professor Abhijit Dasgupta, Dean's Representative
Professor Yifei Mo
Professor Lourdes G. Salamanca-Riba

Acknowledgments

LH

All the Js and Bs

SA and MK

LS, AD, and YM

CS, EM, EO, and PD

TA, BM, and DD

FCJ and ACJ

And all you other wonderful people

Thanks!

Table of Contents

List of Tables

List of Figures

Chapter 1:   Introduction

Titanium (Ti) alloys exhibit excellent specific strength, toughness, high temperature stability, and corrosion resistance, among other characteristics [1, 2]. This unique set of properties enables use in applications as varied as jet engines [3], artificial hip joints [4], offshore oil drilling equipment [5], and suspension components for the Spirit and Opportunity Mars rovers [6]. Pure Ti exhibits an isomorphous phase transformation from the hexagonal close packed (hcp) α-phase to the body centered cubic (bcc) β-phase at 682° C [7], enabling a wide range of microstructures in alloyed products. The crystal structure and microstructure of Ti alloys contributes significantly to material performance; alloying and thermo-mechanical processes are applied to produce single phase hcp α-Ti alloys, which exhibit high elastic stiffness and relatively low yield strength; single phase bcc β-Ti alloys which have a lower elastic modulus compared to α-Ti alloys but have a higher yield strength; or dual-phase α-β Ti alloys which exhibit a wide range of properties dependent on the phase volume fraction and microstructure. However, despite their various applications, many deformation characteristics of Ti alloys are poorly understood. For example, nucleation and growth of twins in Ti alloys, particularly in the α-phase, remains an active research area in the materials science community; behavior includ-

ing non-Schmid deformation [8, 9, 10, 11], non-Hall-Petch twin nucleation [12, 13], apparent oxygen (O) interstitial limited twin growth [14, 15, 16, 17], and even as-yet undefined conditions for twin nucleation all confound our understanding and the predictive capability necessary to develop higher performance Ti alloys. Twin growth is an important deformation mechanism in Ti alloys and a more complete understanding of the governing characteristics will support improved creep resistance, greater strength and ductility, and superior fatigue behavior across a wide range of applications.

1.1 Interaction Stresses at Microstructural Interfaces

Interaction between two volumes with different elastic properties, for example across a phase boundary or grain boundary, produces an elastic interaction stress. A schematic representation of the stress-strain curves for α- and β-Ti alloys in Figure 1.1 provides a indication of the source of this stress. The strain far from the interface due to an applied stress σ_{App} is different in each phase due to the different elastic moduli. However, the displacement compatibility requirement at the interface produces an intermediate strain $\epsilon_{interface}$ which in higher than the α-phase strain far from the interface and lower than the β-phase strain far from the interface. The end result is a compressive interaction stress in the β-phase and a tensile interaction stress in the α-phase.

Elastic interaction stresses have been modeled and measured in Ti alloys as shown in Figure 1.2. Although initials studies of specific conditions report the
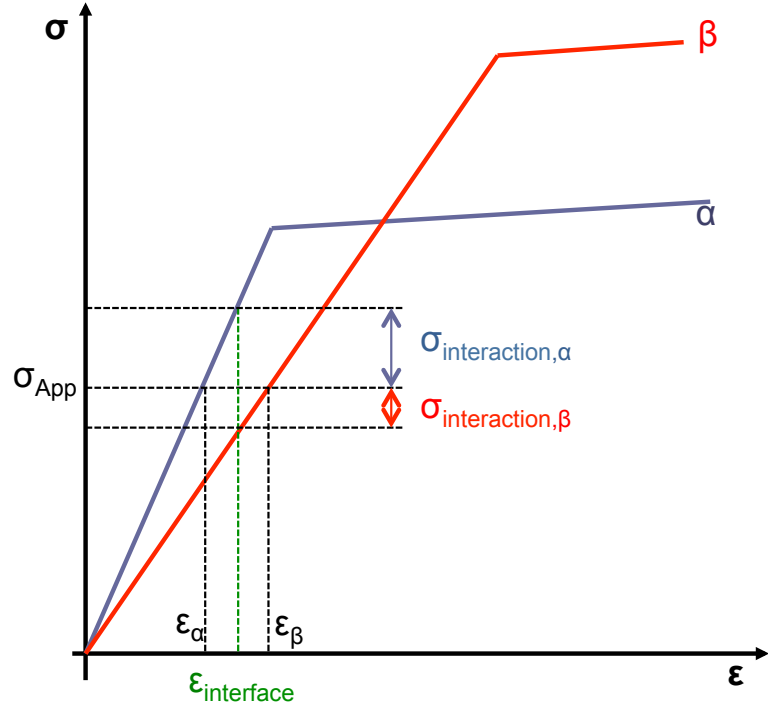
Figure 1.1: Schematic stress-strain curves for α- and β-Ti phases, demonstrating the source of elastic interaction stresses. Applied stress σ_{App} produces strains ϵ_α and ϵ_β in the α- and β-phases (respectively) far from the interface and $\epsilon_{interface}$ at the interface. The difference between $\epsilon_{interface}$ and $\epsilon_\alpha/\epsilon_\beta$ produces a tensile interaction stress in the α-phase, $\sigma_{interaction,\alpha}$, and a compressive interaction stress in the β-phase, $\sigma_{interaction,\beta}$.

degree to which interaction stresses resolve onto certain slip systems [18], no systematic effort to quantify interaction stress effects during twinning exists. It is not known whether resolved interaction stresses are sufficient to explain non-Hall Petch and non-Schmid behavior during twin nucleation and growth, nor is it understood how interface orientation affects the development of interaction stress. Quantifying the effects of these stresses on deformation in Ti alloys would provide invaluable information for alloy and process design.

1.2 Interaction Between O Interstitials and Deformation Mechanisms in Ti

The Ti-O system is unique from most metal-gaseous element combinations in several important ways. For example, a large number of phases exist – structural information is reported for at least 26 different Ti-O structures – and the solubility of O in hcp Ti is up to 33 atomic percent at room temperature [7].

Though an increase in hardness with interstitial impurity content was reported as early as 1951 [21], perhaps the earliest effort to understand the relationship between interstitial elements and deformation mechanisms in α-Ti was reported by Churchman based on observations that samples with combined O and N concentration of approximately 0.01 wt% exhibited prismatic $\langle a \rangle$ slip and small amounts of basal $\langle a \rangle$ slip while samples with a combined O and N concentration of approximately 0.1 wt% deformed by a combination of basal $\langle a \rangle$, prismatic $\langle a \rangle$, and pyramidal $\langle c + a \rangle$ slip [22]; a hard-sphere model suggested that while interstitials

a)

b)

c)
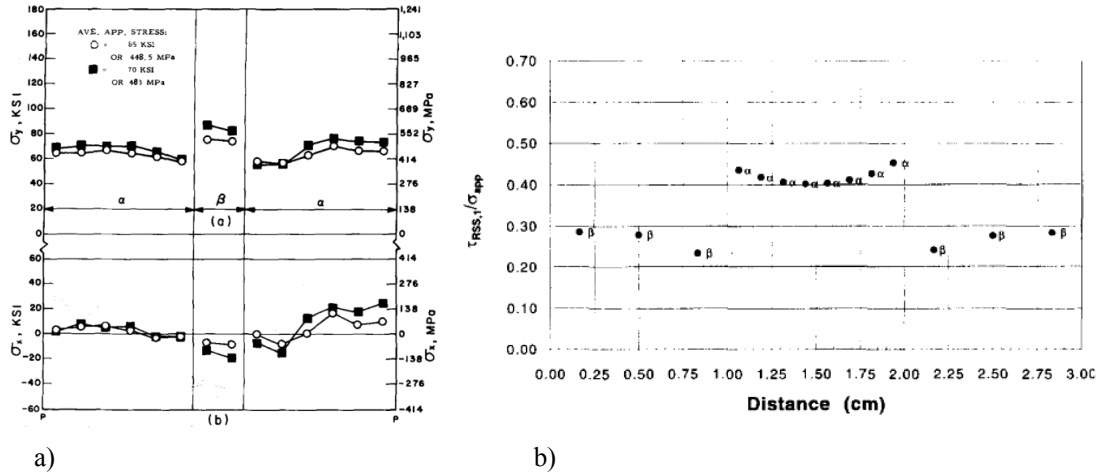
Figure 1.2: a) Example interaction stress calculated by Ankem & Margolin [19] where the x-axis is distance across a β-platelet surrounded by an α-matrix, and the y-axis is transverse and longitudinal stress; b) Example interaction stress calculated by Ankem & Greene [18] where the x-axis is distance across an α-platelet surrounded by a β-matrix, and the y-axis is the resolved shear stress on the prismatic slip system in the α-platelet; (c) Experimental measurements by Guo, Britton, & Wilkinson [20] for two α-grains and a grain boundary. Slip has occurred along the solid line in the top grain (left), but not in the lower grain along the dashed line; this causes an interaction stress in the lower grain along the dashed line, shown in the plot (right, blue dots are measurements, red line is a simple model).

in either octahedral position are out of plane with basal and prism planes (and therefore able to act as a barrier to both slip systems), only one of the octahedral positions is out of plane with a given pyramidal plane, and $\langle c+a \rangle$ slip should thus become more likely as interstitial content increases. Similar behavior was identified in Ti-6Al-4V by Welsch [23] where an alloy containing 0.07 wt% O deformed by fine prismatic $\langle a \rangle$ slip in most heat treatments, while an alloy containing 0.19 wt% O deformed by a combination of fine prismatic $\langle a \rangle$ slip, fine pyramidal $\langle c+a \rangle$ slip, and coarse prismatic $\langle a \rangle$ slip. Systematic measurements of temperature and strain rate effects on flow properties provide further insight into the importance of thermally activated processes during interaction of deformation products and interstitials in Ti: the strengthening effect of O, N, and C interstitials in α-Ti is largest at very low temperatures with almost no difference in yield stress between samples with 0.04 at% and 0.48 at% O above 350°C; the strain rate sensitivity of the same Ti-O samples is zero both for temperatures near 0 K and temperatures above 350°C [24].

There are two plausible mechanisms through which O interstitials could affect dislocation activity: size misfit and chemical misfit. Size misfit, where an interstitial modifies the strain field of a nearby dislocation and the local stiffness of the lattice, is well understood and described through elasticity theory [24], though studies involving atomistic calculations are lacking. Chemical mistfit is due to changes in the stacking fault energy (SFE), where lower SFE promotes the formation of partial dislocations which are unable to climb thereby increasing strength and improving local hardening. Analysis of x-ray diffraction (XRD) results from deformed samples suggests that SFE does in fact decrease with increasing O, though this technique

6

can not differentiate between different (e.g. basal vs. prismatic) stacking faults [25].
More recent DFT calculations of generalized stacking fault energy (GSFE) for the
$(0001)[1\bar{1}00]$ system in pure Ti along with supercells containing approximately 1
at.% O, carbon (C), and hydrogen (H) confirm that the presence of O impurities
(as well as C and H) decreases the basal SFE in Ti [26]. Recent application of DFT
calculations to the Ti-O system indicate that low-energy O interstitial sites exist
in the core of prismatic edge dislocations and that the presence of these defects
increases Peierls stress for slip by a factor of 4 [27].

While significantly less studied than O interactions with dislocations in Ti,
the presence of O interstitials may also impede the growth of twins. Observation of
slow twin growth despite prevailing belief that twins grow very quickly provoked an
analysis suggesting that O interstitials may result in time-dependent twinning by
obstructing the twin shearing/shuffling process [28]. Both high purity α-Ti with 250
parts per million (ppm) O and commercial purity α-Ti with 2500 ppm O exhibit a
peak in twinning activity (measured as the twin volume fraction at 5% strain) be-
tween 400°C and 600°C however twin volume fraction in the lower purity material
trends towards zero nearing 0°C while twin volume fraction at the same temperature
in the higher purity material exceeds 35 volume percent. A study on the fatigue
strength of α-Ti showed reduced twinning and improved fatigue strength with in-
creasing O content, though no mechanism was proposed [29]. A simple analysis
of $(10\bar{1}2)$ and $(11\bar{2}1)$ twin growth in zirconium (Zr, an hcp metal with a crystal
structure similar to Ti) demonstrates longer shuffle distances for the interstitials to
reach twinned sites, as compared to the metal atoms, which could cause interstitial-

7

twin interaction in Ti and Zr [30]. A more complete effort combining experimental work with a crystallographic model suggested that O interstitial sites are not conserved during the shearing process associated with twin growth and the interstitials thus interfere with twin growth in bcc Ti [14]. Experimentally, time dependent $\{10\bar{1}2\}$ twinning (Figure 1.3b) and strain-rate sensitive twin growth (Figure 1.3a) is obersverd in α-Ti which may be due to the presence of O interstitials [15, 16, 17]. O interstitials are also found to impede other shear-dominated processes such as the martensitic $\alpha \rightarrow \omega$ transformation in Ti [31] and Zr [32]. Recent DFT calculations by Ghazisaeidi and Trinkle provide additional clarity on the relationship between O interstitials and twins in hcp Ti, demonstrating that both attractive and repulsive O octahedral interstitial sites exist in the vicinity of a twin boundary [33].

While crystallographic modeling suggests plausible mechanisms for twin-O interaction, a thorough investigation and quantification is required to enable purposeful development of improved alloys. The continued evolution and maturation of computational materials science techniques provides a promising avenue for exploring this system and developing quantitative, mechanistic descriptions of the effects of O interstitials on twin growth and mechanical behavior in Ti alloys.

1.3   Research Summary

The overall objective of this research is to apply a combination of theoretical and computational techniques, along with experimental data, to produce new insight into how phase boundaries and O interstitials affect the nucleation and growth of
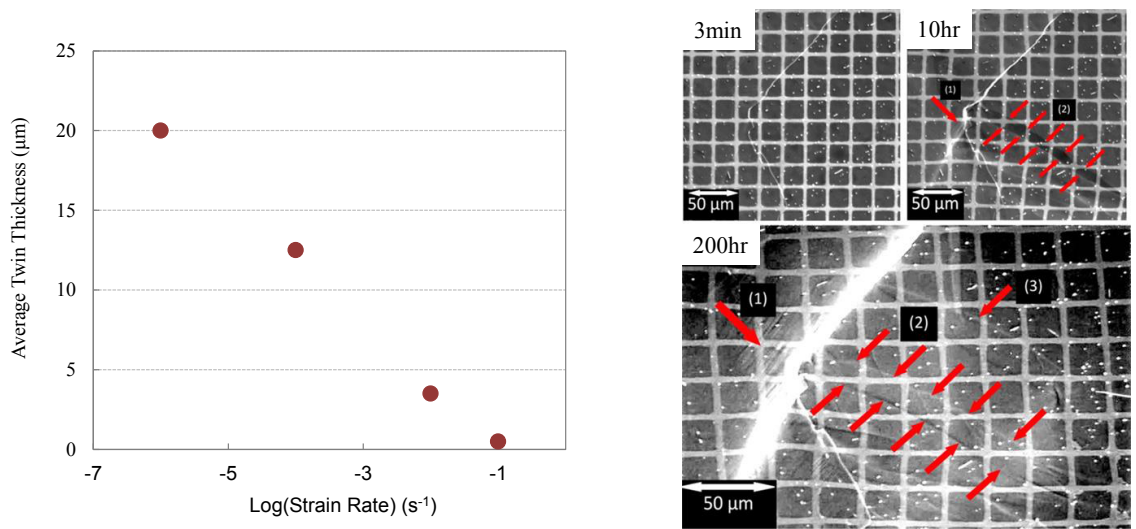
Figure 1.3: a) The average twin thickness varies as a function of strain rate after quasi-static tensile testing to 3% total strain (data from [17]). b) Growth of twins is observed to occur slowly over several hundred hours during creep testing, where the twin boundaries are indicated with red arrows [16]. Both a) and b) report results for α-Ti-1.6 V (wt%).

twins in Ti. Ultimately, the goal of this work is to enable the development of new, high-performance Ti alloys based on a clearer understanding of defect interactions with twins. Based on the background described above, this research is pursued in three phases:

1. Quantify the development and effects of elastic and plastic interaction stresses during twin nucleation in the α-phase of Ti alloys

2. Establish a Modified Embedded Atom Method (MEAM) potential for the Ti-O system as a tool to thoroughly investigate O interstitial interactions with deformation twins in the α-phase of Ti alloys

3. Identify and characterize the as-yet unreported critical interactions between O interstitials and growing twins in the α-phase of Ti alloys through a combination of MEAM, density functional theory (DFT), and experimental data

First, in order to improve our understanding in the area of twin nucleation, we apply a combination of the finite element method (FEM) and dislocation theory to quantify the development of elastic and plastic interaction stresses in dual-phase α-β Ti alloys and to explore the effect of these stresses on experimentally observed non-Schmid and non-Hall-Petch twin nucleation. Chapter 2 presents the FEM model development and validation process, while chapter 3 presents the integration of these models with various analytical techniques to systematically quantify the effects of the α-β interface on the development of interaction stresses and the nucleation of deformation twins. These results demonstrate for the first time that the combination

of elastic and plastic interaction stresses is responsible for the measured variability in the critical resolved shear stress for slip and twinning in α-Ti. Further, the local stress fields due to interaction stress initiate slip at up to 30% lower applied stress than is expected based on Schmid's Law. In some orientations, the primary deformation mechanism changes from slip to twinning as a result of the α-β interface.

Second, in order to improve understanding in the area of twin growth, we utilize DFT and MEAM calculations while leveraging earlier experimental results to explore the interactions between O interstitials and growing twins in the α-phase of Ti alloys. Chapter 4 presents a new MEAM potential for the Ti-O system developed during this research, which has been published [34], and which supports our own effort as well as research on atomistic interactions of Ti and O throughout the scientific community. Chapter 5 presents an application of the Ti-O MEAM potential in combination with DFT calculations to quantify the effect of a $(10\bar{1}2)$ twin boundary on the formation energy of O interstitials and the activation barriers for diffusion between interstitial sites. These results provide the first reported quantification of interstitial behavior near any twin boundary (in Ti or otherwise) as well as demonstrating that diffusion of O across the twin boundary is easier than in the bulk.

Finally, chapters 6 and 7 provide concluding remarks and a discussion of future opportunities. Overall, this research demonstrates and quantifies the effects of two important defects (microstructural boundaries and O interstitials) on the nucleation and growth of twins in the α-phase of Ti alloys. Given the breadth of Ti applications and the importance of twin growth in the mechanical properties of Ti alloys, these

results enable improved alloy, process, and component design for many products that affect our lives every day.

Chapter 2:   Finite Element Model Development and Testing

Finite element method (FEM) modeling is a powerful technique for interrogating material behavior. Material characteristics and geometry can be controlled directly, and simulation results can be read from nearly any position in the sample. FEM modeling is also an intriguing platform for developing models of elastic-plastic behavior in materials; new material models can be implemented in a FEM solver and compared to experimental data as a method of model validation. However FEM simulations are sensitive to the model set-up and features such as model construction, mesh characteristics, and mesh constraints. These model/mesh characteristics, which are not present in "real" samples, can drive undesirable deviation from reality hence it is important to validate that models used for research behave as desired. In this study, results published by Greene and Ankem [18] are treated as a "baseline" and reproduced using new finite element models to validate model behavior. The choice of material and model parameters is carefully considered; particular focus is given to the construction of the finite element model and the meshing parameters, including model constraints.

2.1 Baseline Model

Greene and Ankem explored the behavior of α-Ti platelets in a β-Ti matrix in four scenarios represented schematically in Figure 2.1: bicrystal, tricrystal, single inclined plate, and triple inclined plate [18]. For this study, only the bicrystal, single inclined plate, and triple inclined plate are tested; the tricrystal model produces results quite similar to the bicrystal model [18]. For each scenario, the top surface of the sample is displaced such that the material remains in the elastic regime and the shear stress resolved onto the $\langle 1\bar{2}10\rangle(0001)_\alpha$ and $\langle 1\bar{1}1\rangle(110)_\beta$ slip systems is measured across the interface between the α and β-phases.
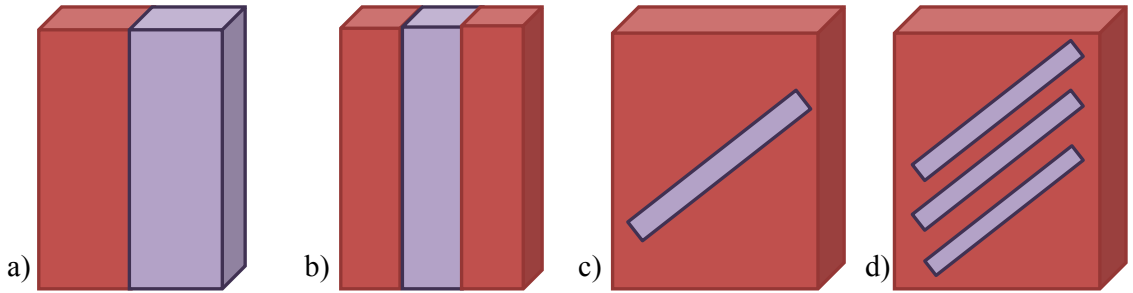
Figure 2.1: Test scenarios from [18]: a) bicrystal, b) tricrystal, c) single inclined plate, and d) triple inclined plate. The α-phase is shown in purple and the β-phase is shown in red.

2.2 Establishing Materials Parameters

Material characteristics such as the Young's Modulus or stiffness matrix are a critical input into a finite element model. A single, isotropic modulus value may be

Table 2.1: Compliance tensor component values for the α- and β-phases in Ti ($\times 10^{-11}$ Pa).

Phase	s_{11}	s_{33}	s_{44}	s_{12}	s_{13}	s_{66}
α [35]	0.9581	0.6980	2.1410	-0.4623	-0.1893	2.8410
β [19]	1.8570	1.8570	2.3420	-0.7741	-0.7741	2.3420

representative of a large collection of randomly oriented grains, however the intent of these models is to explore the deformation behavior of Ti at a microstrucural scale, across the boundary between two phases. The stiffness or compliance matrix is therefore required in order to accurately describe the anisotropic elastic behavior of individual α- and β- grains. The stiffness matrices for the α-phase [35] and β-phase [19] of Ti have been converted to compliance values and are shown in Table 2.1. The values shown for α-Ti are for pure Ti. The values shown for β-Ti were measured from a Ti-10%Cr sample, which is necessary because pure β-Ti is not stable at room temperature.

The relative orientation of the α- and β-phases in Ti is not arbitrary. Rather, the two phases have a well-documented relative orientation with a $(\bar{5}140)_\alpha||(\bar{3}34)_\beta$ interface plane and a $\langle 1\bar{2}10\rangle(0001)_\alpha||\langle 1\bar{1}1\rangle(110)_\beta$ Burgers orientation relationship [36]. To reflect this in the finite element models, the stiffness matrices for each phase must be rotated accordingly. In addition, the direction of the applied load must be considered; as in [18], the orientation of the phases in each the test scenario is set such that shear stress is maximized on the $\langle 1\bar{2}10\rangle(0001)_\alpha$ and $\langle 1\bar{1}1\rangle(110)_\beta$ slip

systems. Maximizing the shear stress on these slip systems is necessary to determine the influence of interaction stresses on slip behavior in the worst-case scenario. The angles between the various planes and directions of interest are required in order to perform the necessary tensor rotations. As a tool for representing orientation and angles in the α-β system, we construct a composite stereographic projection which overlays the $(0001)_\alpha$ and $(110)_\beta$ stereographic projections. Overlapping the $(\bar{5}140)_\alpha$ and $(\bar{3}34)_\beta$ poles implements the correct interface plane alignment as in Figures 2.2a and 2.2b. We then calculate the locations of the remaining points on the stereographic projection as angles from the $(\bar{5}140)_\alpha$ and $(\bar{3}34)_\beta$ poles, ϕ, using the relationships

$$\cos(\phi_{Cubic}) = \frac{h_1 h_2 + k_1 k_2 + l_1 l_2}{\sqrt{(h_1^2 + k_1^2 + l_1^2) + (h_2^2 + k_2^2 + l_2^2)}} \tag{2.1}$$

$$\cos(\phi_{Hex}) = \frac{h_1 h_2 + k_1 k_2 + \frac{1}{2}(h_1 k_2 + h_2 k_1) + \frac{3a^2}{4c^2} l_1 l_2}{\sqrt{(h_1^2 + k_1^2 + h_1 k_1 + \frac{3a^2}{4c^2} l_1^2)(h_2^2 + k_2^2 + h_2 k_2 + \frac{3a^2}{4c^2} l_2^2)}} \tag{2.2}$$

where $(h_1 k_1 l_1)$ and $(h_2 k_2 l_2)$ are the planes of interest and a and c are the hexagonal lattice constants for α-Ti ($a = 0.29512$ nm and $c = 0.46845$ nm) [37]. There are three coordinate systems that are relevant to the test scenarios outlined above: (1) the standard orientation directions of the unrotated compliance tensors, x_0^α, y_0^α, z_0^α and x_0^β, y_0^β, z_0^β; (2) the coordinate system for the test scenario, x', y', z'; (3) the coordinate system for the $\langle 1\bar{2}10 \rangle (0001)_\alpha$ and $\langle 1\bar{1}1 \rangle (110)_\beta$ slip systems (which are aligned due to the Burgers orientation relationship), x'', y'', z''. Equations 2.1 and 2.2 are used to identify the locations of these poles on the stereographic projection in Figure 2.2.
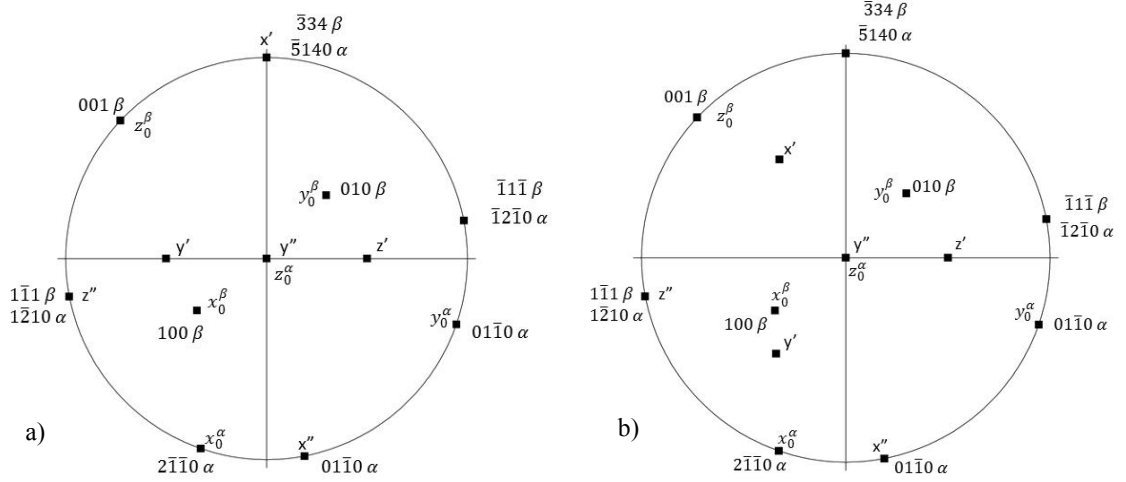
Figure 2.2: Composite $(0001)_\alpha$ and $(110)_\beta$ stereograpic projections rotated to represent the a) bicrystal and b) inclined plate test scenarios

The stereographic projections in Figure 2.2 provide the angles between the planes of interest which can then be used to calculate the direction cosines. Two tensor rotation operations are necessary in this study: rotating the original compliance matrices into the (x', y', z') system (see Figure 2.4) for input into ANSYS, and rotating the resulting stress tensors to evaluate resolved shear stress on the slip plane. Both the compliance and stress tensors can be rotated as second rank tensors using the relationship

$$T'_{ij} = a_{ik}a_{jl}T_{kl} \tag{2.3}$$

where T'_{ij} is the ij component of the rotated tensor, a_{ik} and a_{jl} are components of the direction cosine matrix, and T_{kl} is the kl component of the original tensor; this equation is written in the conventional dummy suffix notation and can be expanded accordingly. The final direction cosines used to perform the necessary tensor rotations are shown in Tables 2.2 and 2.3.

17

(a) x_0^α, y_0^α, z_0^α and x', y', z'

	x_0^α	y_0^α	z_0^α
x'	-0.946	-0.326	0.000
y'	0.242	-0.669	0.707
z'	-0.242	0.669	0.707

(b) x_0^β, y_0^β, z_0^β and x', y', z'

	x_0^β	y_0^β	z_0^β
x'	-0.500	0.530	0.707
y'	0.857	0.122	0.500
z'	0.156	0.848	-0.500

(c) x', y', z' and x'', y'', z''

	x_0'	y_0'	z_0'
x''	-0.990	-0.105	0.105
y''	0.000	0.707	0.707
z''	-0.174	0.682	-0.707

Table 2.2: Direction cosines between coordinate systems for the bicrystal test scenario

(a) x_0^α, y_0^α, z_0^α and x', y', z'

	x_0^α	y_0^α	z_0^α
x'	-0.530	-0.695	0.500
y'	0.819	-0.259	0.500
z'	-0.242	0.669	0.707

(b) x_0^β, y_0^β, z_0^β and x', y', z'

	x_0^β	y_0^β	z_0^β
x'	0.208	0.454	0.857
y'	0.956	-0.276	-0.122
z'	0.156	0.848	-0.500

(c) x', y', z' and x'', y'', z''

	x_0'	y_0'	z_0'
x''	-0.778	0.616	0.104
y''	0.500	0.500	0.707
z''	0.342	0.616	-0.707

Table 2.3: Direction cosines between coordinate systems for the inclined plate test scenario
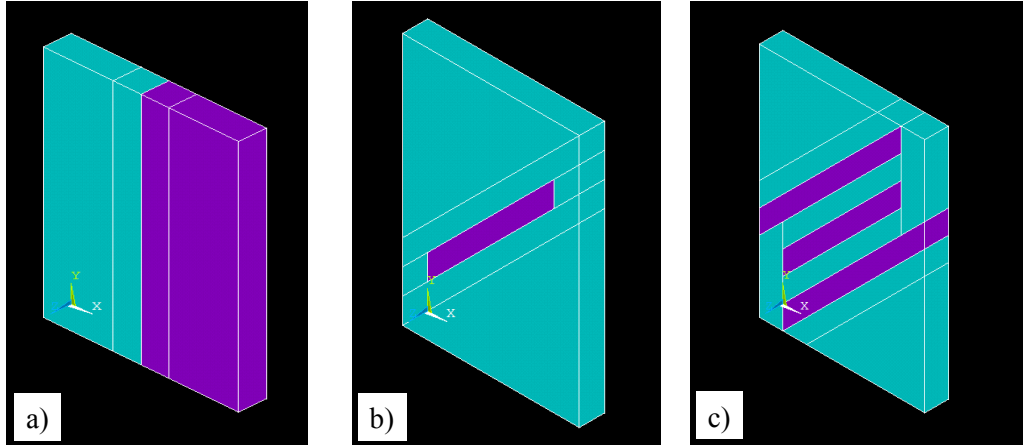
Figure 2.3: Final solid models for the a) bicrystal, b) single inclined plate, and c) triple inclined plate scenarios.

2.3 Model and Mesh Testing

In constructing a finite element model it is important to recognize that most model and mesh characteristics, such as mesh size or element type, do not exist in the real, physical scenario that is being simulated. Hence these characteristics must be chosen such that they provide accurate simulation results in a manner that is computationally efficient. The element type, model details, and mesh parameters for these simulations were selected to assure accuracy and model performance. Figure 2.3 shows the final models for the bicrytsal, single inclined plate, and triple inclined plate scenarios.

Having established the models, the simulation constraints were developed to mimic a standard tensile test, with the bottom of the model acting as the center of a real-world tensile bar. The test scenario and notation convention for the points in the models is shown in Figure 2.4. All nodes on plane EFGH are constrained in
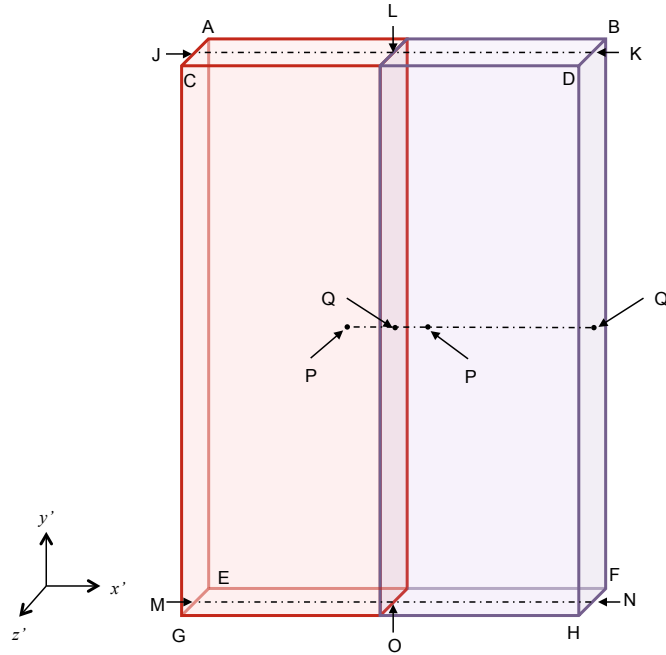
Figure 2.4: Test scenario schematic showing coordinate system orientation and reference points A-N.

the y direction; all nodes along lines JK and MN are constrained in the z direction; the node a point L is constrained in the x and z directions; the node at point O is constrained in all directions; the nodes on plane ABCD are coupled to displace the same distance in the y direction.

An important and useful feature of the ANSYS postprocessor is path operations. The stress state after simulation is reported (as a tensor) at each corner node in the mesh; one way to increase the spatial resolution of the stress results is to refine the mesh size however this requires additional computational effort. Path operations offer a second option for reading stress results from the simulation by interpolating the stress results between nodes. There are a variety of path operation options that must be set correctly prior to reading path data. The following text

provides the ANSYS Parametric Design Language (APDL) code necessary to set up the path options for these test scenarios; the APDL code is commented to provide insight into each option.

```
PATH,SPATH,2,,500    !Creates a path called SPATH with 500 divisions
PPATH,1,,0,50,5      !Sets the starting point at (0,50,5)
PPATH,2,,70,50,5     !Sets the end point at (70,50,5)
PMAP,,MAT            !Path option for use with material discontinuities
PDEF,XSTRS,S,X       !Store the x-stress results to the variable XSTRS
PDEF,YSTRS,S,Y       !Store the y-stress results to the variable YSTRS
PDEF,ZSTRS,S,Z       !Store the z-stress results to the variable ZSTRS
PDEF,XYSHR,S,XY      !Store the xy-shear results to the variable XYSHR
PDEF,YZSHR,S,YZ      !Store the yz-shear results to the variable YZSHR
PDEF,XZSHR,S,XZ      !Store the xz-shear results to the variable XZSHR
RSYS,0               !Report results in the global coordinate system
```

Considerable effort was applied towards optimization to provide an accurate, computationally efficient model for further use. While the computation times of the non-optimized models/meshes described below are not exceptionally long, these test scenarios only require simulation of elastic properties. Future work may include plasticity and twin formation which requires considerable added computational time. Starting with an optimized baseline model will help to ensure that the computational expense is minimized for these more complex scenarios. The ANSYS program offers more than 100 different element types, including elements for simulating thermal, electrical, mechanical, and multi-physics problems. The test scenarios outlined above represent mechanical problems, and solid elements are required to avoid restricting the test to plane strain (as would be the case for 2D elements). These restrictions reduce the number of available element types to nine. Of these nine, six are either restricted to special applications (such as SOLID65

which is intended for modeling reinforced concrete) or are limited in their solution capabilities (such as SOLID45 which does not have plasticity and creep functionality). The three remaining elements are SOLID185, SOLID186, and SOLID187. For computational efficiency and potential improvement in accuracy, a brick element is generally used whenever possible; SOLID187 is a 10 node tetrahedral element and does not support brick geometry. Both SOLID185 and SOLID186 support brick geometry with the only major difference being the number of nodes: SOLID185 has 8 nodes per element while SOLID186 is a higher order element with 20 nodes per element. Higher order elements support non-linear displacement between corner nodes, which could improve accuracy in some scenarios. Alternatively, lower order elements require substantially less computation time. The test scenarios in this study operate in the elastic regime and do not deform substantially so it is unlikely that higher order elements are necessary. However, to confirm that the SOLID185 element performs adequately, a comparison test was run where the single inclined plate scenario was modeled using the SOLID185 and SOLID186 elements. The results of the SOLID185-SOLID186 comparison test are shown in Figure 2.5 with the calculation time for each simulation shown in parentheses; simulation with the SOLID185 element achieves comparable results when compared to simulation with the SOLID186 element, but at lower computational cost. Based on these results, the SOLID185 element was used for the remaining scenarios.

The mesh size for these models is expected to have a significant effect on both model accuracy and computational requirements so a study was conducted to determine the appropriate mesh size for the inclined plate models. Before considering
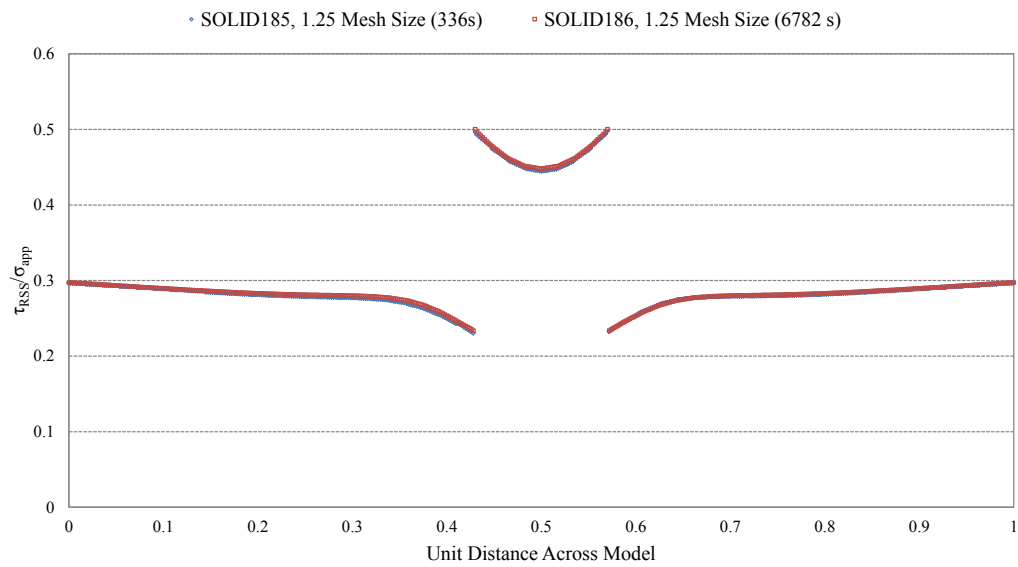
Figure 2.5: SOLID185-SOLID186 element comparison test results for the single inclined plate model. Computation time is shown in parentheses in the legend. Note that the results are very similar for both element types but the SOLID186 element requires significantly more processing time.

the use of a variable-size mesh (where the mesh size varies throughout the sample), a baseline mesh size was determined as a reference point for model performance. To determine the baseline, simulations with increasingly fine mesh sizes were run until the results converged with respect to mesh size. The mesh size study was conducted using the single inclined plate model meshed at four different sizes: 1, 1.25, 2.5, and 5 units (versus the total model height of 100 units). The simulation results and computer time are summarized in Figures 2.6 and 2.7. These results show that changes to mesh size have a significant effect on model performance when decreasing from 5 to 2.5 units and from 2.5 to 1.25 units. Conversely, the decrease from 1.25 to 1 units has a very small effect on model accuracy but a significant effect on computation time. Based on these results, a mesh size of 1.25 has been selected for the models; this mesh size serves as a measure of baseline performance (both for accuracy and computation time) as well as establishing an upper limit on mesh size for the area near the platelet.

To further reduce computational requirements, a composite mesh was developed with variable mesh size throughout the sample as shown in Figure 2.8. Using variable mesh size allows sufficient resolution in the regions of interest (near the α-β interface) without high resolution in areas of less interest (far from the interface in the β-phase). In order to build a composite mesh from the single platelet model in Figure 2.3b, the corner volumes (away from the platelet) were constructed with a mesh size of 2.5 units (versus a model height of 100 units). The volumes near the platelet have a mesh size of 0.75 units. The single plate test scenario using the composite mesh is compared to the results from the uniform 1.25 mesh size test

scenario in Figure 2.9. These results show that the models produce similar results, particularly near the interface, but the variable mesh simulation required only 21 seconds of simulation time versus 336 seconds for the uniform mesh.

The results from the single inclined plate scenario provide an indication of the model and mesh properties required for efficient, accurate simulation in the triple inclined plate test scenario. The triple inclined plate model in Figure 2.3c was built specifically to accommodate a variable mesh by including large corner sections and small regular diagonals through the platelets. A mesh size of 2.5 in the corner sections and 0.75 in the platelet diagonals (compared to a model height of 100 units) was used based on the results from the single inclined plate optimization tests. The plot of normalized resolved shear stress versus distance along line Q-Q is shown in Figure 2.10; this is similar to the results published in [18] but with considerable improvement in resolution.
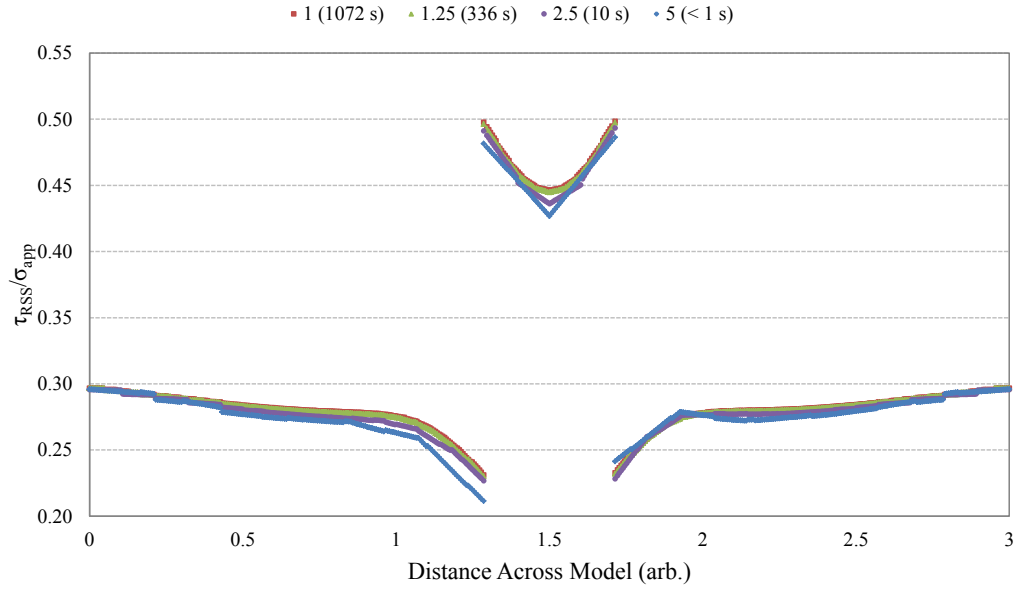
Figure 2.6: Shear stress resolved onto the $\langle 1\bar{2}10 \rangle (0001)_\alpha$ and $\langle 1\bar{1}1 \rangle (110)_\beta$ slip systems, normalized to the applied stress, versus distance along line Q-Q (Figure 2.4) on the single inclined platelet model. Results are shown for four different mesh sizes as indicated. Computation time for each simulation is shown in parentheses in the legend.
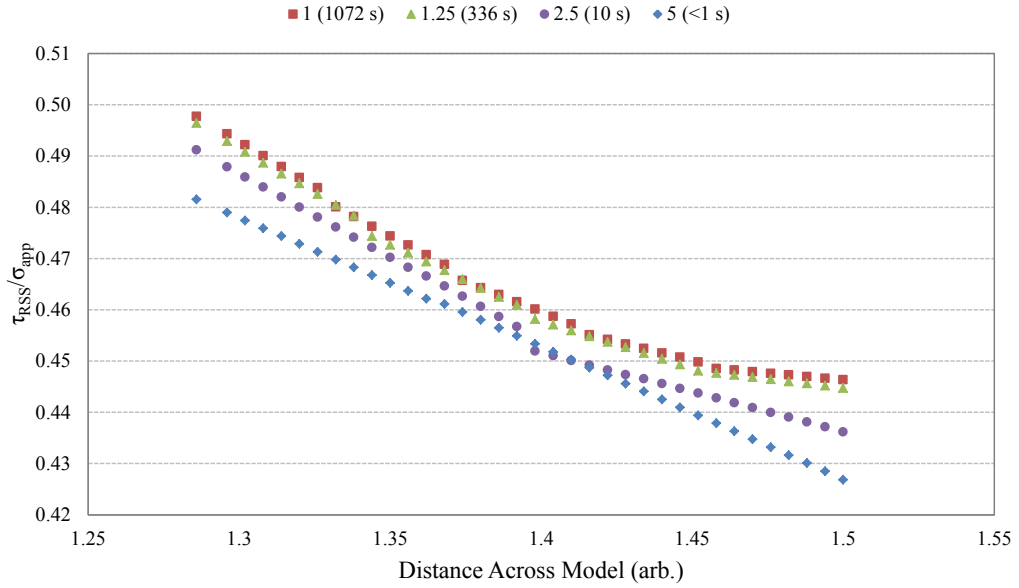
Figure 2.7: Close-up view of the results from Figure 2.6 showing normalized re-solved shear stress through the first half of the platelet. Results are shown for four different mesh sizes as indicated. Computation time for each simulation is shown in parentheses in the legend.
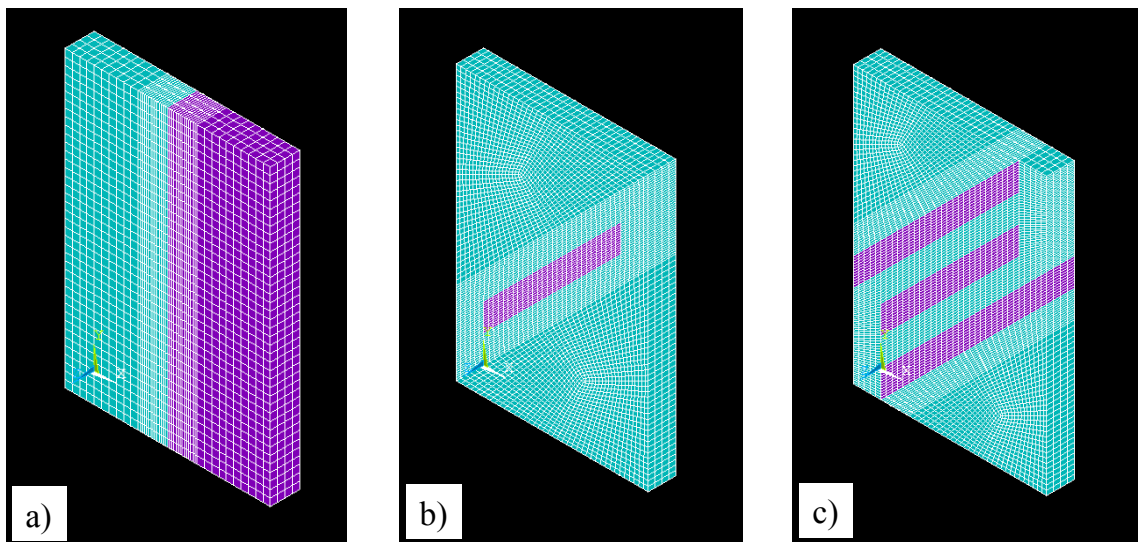
Figure 2.8: Final meshes for the a) bicrystal, b) single inclined plate, and c) triple inclined plate scenarios.
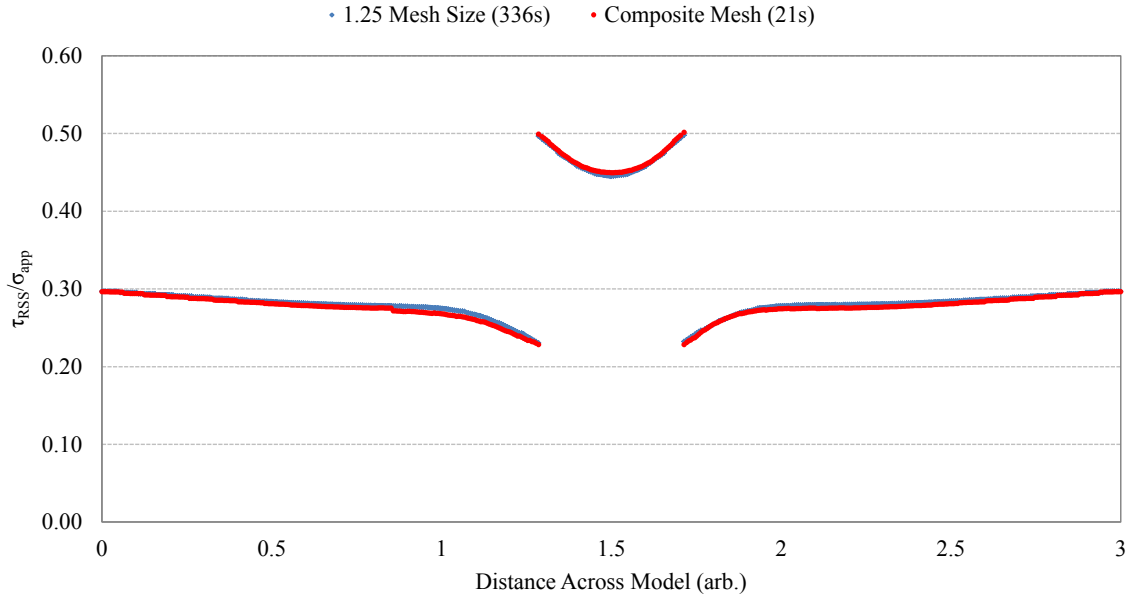
Figure 2.9: Shear stress resolved onto the $\langle 1\bar{2}10\rangle(0001)_\alpha$ and $\langle 1\bar{1}1\rangle(110)_\beta$ slip systems, normalized to the applied stress, versus distance along line Q-Q in the single inclined platelet model. Results are shown for the uniform 1.25 mesh size and the composite mesh.
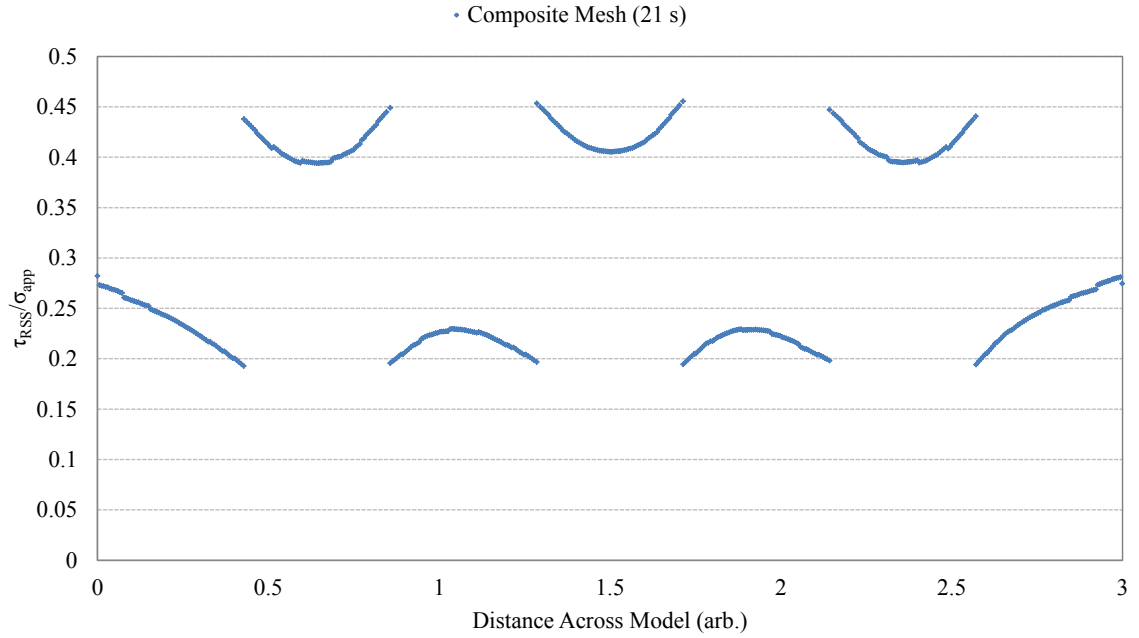
Figure 2.10: Shear stress resolved onto the $\langle 1\bar{2}10 \rangle (0001)_\alpha$ and $\langle 1\bar{1}1 \rangle (110)_\beta$ slip systems, normalized to the applied stress, versus distance along line Q-Q in the triple inclined platelet model using the composite mesh shown in Figure 2.8c.

2.4 Conclusion

While finite element modeling is a useful tool for studying material behavior, the characteristics of the model, mesh, and simulation constraints have significant effects on the model accuracy and computation time. Optimization of these characteristics is an important aspect of FEM model/mesh development. In this study, three test scenarios from previously published research are replicated using updated models and meshing. The results are compared to the published results as a measure of model accuracy. Model characteristics such as mesh size and element type are optimized to establish a combination of model, mesh, and constraint features that provide sufficient accuracy at minimal computational cost.

Chapter 3:   The Effect of Microstructural Interaction Stress on Nucleation and Growth of Deformation Twins

Though dual-phase Ti alloys are a composite of the single-phase constituents, their mechanical behavior cannot always be predicted by a simple rule of mixtures. For example, Jaworski & Ankem [13] demonstrated that a dual-phase Ti-8.1 wt.% V alloy with a Widmansttaten microstructure deformed by twinning in the α-phase and stress-induced martensite (SIM) transformation in the β-phase during tensile testing, whereas a single phase alloy with the same α-phase composition and comparable grain size deformed by slip in the α-phase and slip and twinning in the β-phase. This behavior indicates that the phases interact during deformation to affect the preferred deformation mechanisms and the resulting mechanical behavior in the dual-phase system. One result of the interaction between the constituent phases is the interaction stress, which develops due to differences in the elastic or plastic properties of the two phases [19, 38]. During elastic deformation, the displacement compatibility requirement across the interface of the phases causes the elastically softer β-phase to impart a tensile interaction stress on the elastically stiffer α-phase. Previous research shows that these elastic interaction stresses can resolve onto the deformation systems and increase the total resolved shear stress beyond the contri-

bution from the applied stress alone [19, 18]. Plastic interaction stresses have also been observed using FEM modeling of plastic deformation in dual-phase Ti alloys, showing clear evidence of load shedding (a type of plastic interaction stress) where a higher stress is observed in the high strength phase, a higher strain is observed in the low strength phase, and significant stress and strain gradients are observed at the interfaces [39]. More recently, a time dependent crystal plasticity finite element model (CPFEM) was used to simulate the compressive creep behavior of a hard-oriented α Ti grain embedded in a soft-oriented α-Ti grain; this model predicted load shedding onto the hard-oriented phase with a considerable stress gradient developing near the interfaces [40].

More generally, experimental investigations of the mechanical behavior of dual-phase Ti alloys suggest that the applied stress is not the sole contributor to the activation of specific deformation mechanisms. The activation of a deformation mechanism in many crystalline materials is often modeled to follow Schmid's law where deformation occurs when the resolved shear stress exceeds the critical resolved shear stress (CRSS). However, the reported behavior of dual-phase Ti alloys does not always obey Schmid's law. In-situ scanning electron microscopy (SEM) observations of a tensile deformed polycrystalline dual-phase Ti alloy (93% volume fraction α) indicate that deformation by basal $\langle a \rangle$, prismatic $\langle a \rangle$, and pyramidal $\langle a \rangle$ slip is correlated with Schmid factor, however favorably oriented systems are occasionally not activated while unfavorably oriented systems occasionally slip [10]. Experimental results using single colony samples of α-β Ti deformed at different orientations suggest that slip parallel to the long axis of the platelets obeys Schmid's Law while

slip in other directions does not [8]. Plane strain compression testing of commercially pure (CP) Ti at different orientations demonstrates that the Schmid factor is an effective though imperfect indicator of slip and twinning activity in polycrystalline α-Ti alloys [11]. Interaction stresses were not accounted for in any of these studies due to difficulty measuring the detailed stress state at the grain boundary or phase interfaces. A review of the CRSS for different slip systems measured from single crystal and polycrystalline HCP Ti alloys further reinforces that elastically and plastically anisotropic materials exhibit variability in CRSS and hence deviation from Schmid's Law, which may be attributed to the effects of the local stress state [41]. The significance of interaction stresses during deformation in Ti alloys has been the subject of some debate [8, 42] with a particular emphasis on the importance of yield anisotropy within a deformation system (e.g. CRSS anisotropy within the prismatic $\langle a \rangle$ system); this type of analysis captures the α-β interaction effects by modifying the critical resolved shear stress for directions within a slip system which improves model accuracy but does not demonstrate or discount the significance of interaction stresses.

Despite the focus on predicting the tensile response of Ti alloys, a thorough exploration of the relationship between microstructure, crystallographic/loading orientation, and the development of interaction stresses is not reported in the literature. In this study we apply a combination of finite element method (FEM) models and analytical dislocation-boundary interaction models to quantify the effect of interaction stresses on the onset of plastic deformation in α-β Ti alloys. To assist the reader, standard terminology used in this chapter is clarified here. The term "de-

formation mechanism" refers to general categories such as slip, twinning, or stress induced martensite. The terms "slip system" and "twinning system" refer to symmetrically identical sets of mechanisms such as prismatic $\langle a \rangle$ slip, basal $\langle a \rangle$ slip, or $(10\bar{1}2)$ twinning. The terms "independent slip system" and "independent twinning system" refer to a single, specific direction/plane combination within a slip or twinning system, such as $(1\bar{1}00)[11\bar{2}0]$ prismatic $\langle a \rangle$ slip or $(\bar{1}012)[10\bar{1}1]$ twinning.

3.1   Elastic Interaction Stresses

FEM modeling is a powerful tool for predicting the complicated stress field that arise, for example, from the interaction of the elastically anisotropic α-phase with the elastically anisotropic β-phase in dual-phase Ti alloys. Elastic interaction stresses impact deformation in dual-phase systems, and in order to quantify this impact we compare the Schmid factor, calculated geometrically and therefore ignoring interaction stress, and an "effective Schmid factor", based on FEM results and including interaction stress. Here, the standard Schmid factor is defined as usual per

$$S_{std} = \cos(\phi)\cos(\lambda) = \frac{\tau_{res}}{\sigma_{app}} \tag{3.1}$$

where ϕ is the angle between the applied stress direction and the slip/twinning direction, and λ is the angle between the applied stress direction and slip/twinning plane normal; this is, by definition, the ratio of the resolved shear stress on a slip/twinning system, τ_{res}, and the applied stress, σ_{app}. We define the effective Schmid factor as

$$S_{eff} = \frac{\tau_{tot}}{\sigma_{app}} \tag{3.2}$$

where the total resolved shear stress, τ_{tot}, is the value obtained from FEM simulation and thereby includes contribution from both the applied stress, σ_{app}, and the interaction stress between the α- and β-phases. We further define an interaction Schmid factor, S_{int}, as

$$S_{int} = S_{eff} - S_{std} \tag{3.3}$$

The value of S_{int} provides a measure of the impact of interaction stress on deformation in a particular system: a very large magnitude of S_{int} (which can be positive or negative) indicates that the interaction stress resolves strongly onto a particular deformation system, while a very small magnitude of S_{int} indicates the opposite. Finally, by incorporating the CRSS for deformation in the α-phase we also explore how interaction stresses can contribute to the activation of specific deformation mechanisms, such as by promoting twinning in the α-phase of dual-phase structures instead of slip as found in single α-phase alloys [13].

3.1.1 Model Development

We use two model microstructures to explore the development of interaction stresses: a "bicrystal" model (Figure 3.1) which considers the interaction between the two phases at a single interface, and a "platelet" model (Figure 3.2) which incorporates interactions from multiple adjacent interfaces, such as in a Widmanstätten or lamellar microstructure. We construct finite element models for each of these microstructures using ANSYS® Release 11.0 and SOLID186 elements (hexahedral 20-node quadratic elements). The mesh size and model characteristics are based on
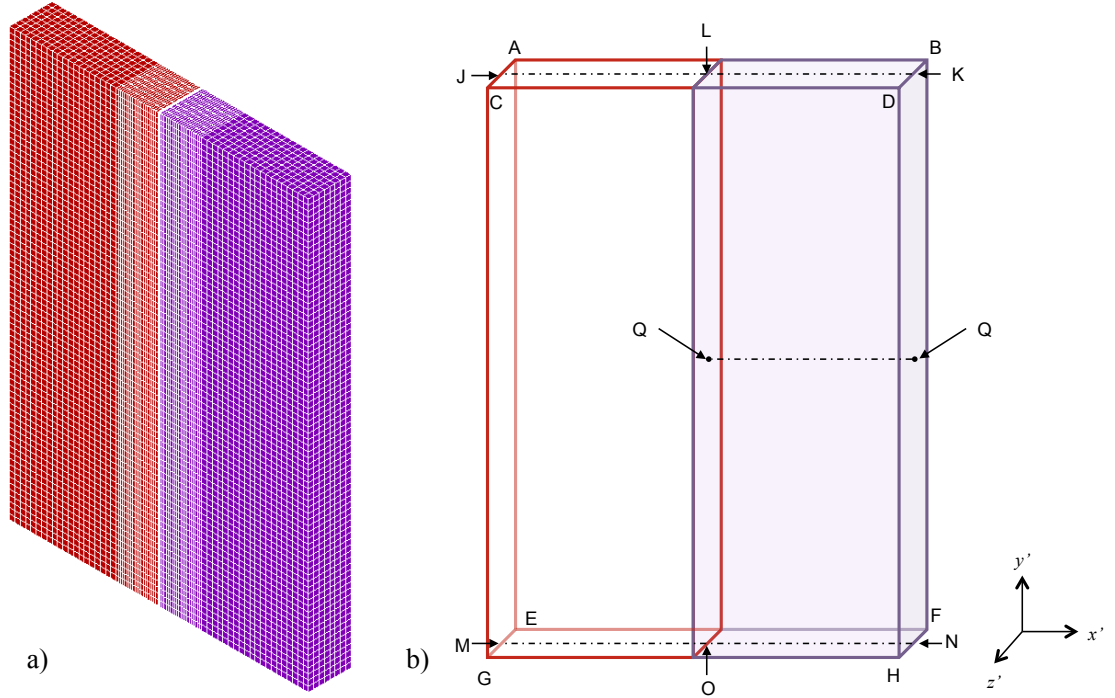
Figure 3.1: a) Finite element model for the "bicrystal" microstructure. b) Model layout and coordinate system convention for the platelet microstructure. The α-phase is shown in purple and the β-phase is shown in red. The interface areas that appear to be white solids are areas with a very fine mesh.

the results described in Chapter 2.

The models are constrained to simulate uniaxial tensile deformation, with the detailed model layout shown in Figures 3.1b and 3.2b. Nodes on face EFHG are constrained in the y' direction, nodes along lines MN and JK are constrained in the z' direction, the node at point L is constrained in the x' and z' directions, and the node at point O has all degrees of freedom constrained. The nodes on face ABDC are constrained such that all nodes displace the same amount in the y' direction. A tensile force along the y'-axis, is applied on the node at point L such that the stress
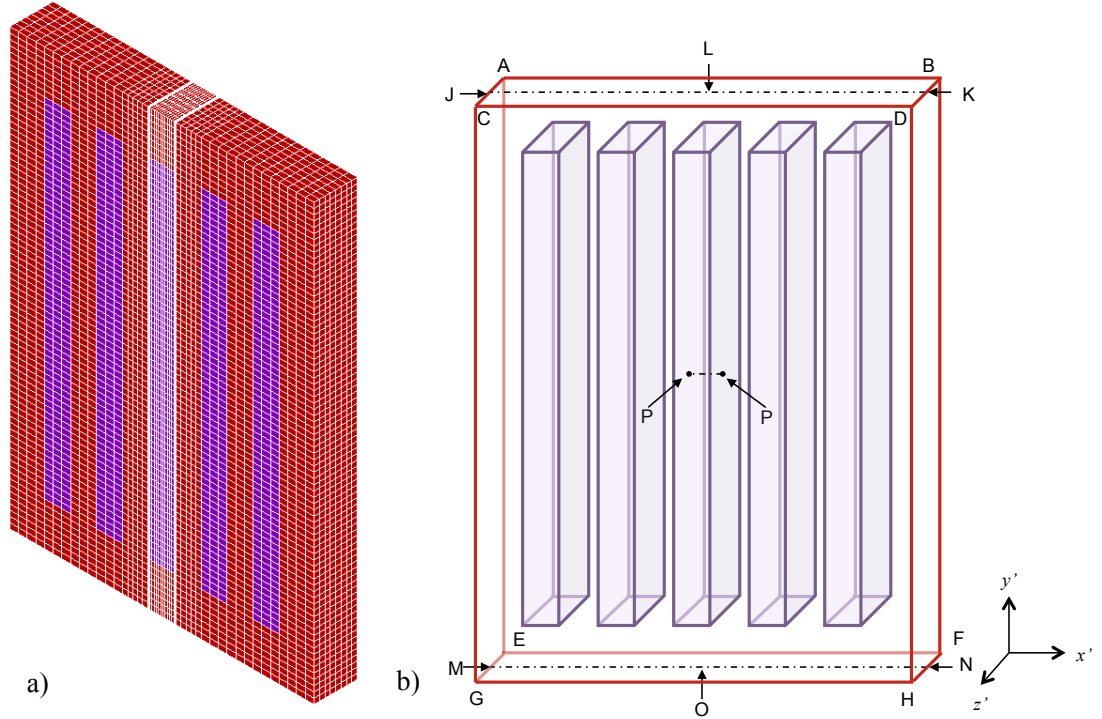
Figure 3.2: a) Finite element model for the "platelet" microstructure. b) Model layout and coordinate system convention for the platelet microstructure. The α-phase is shown in purple and the β-phase is shown in red. The interface areas that appear to be white solids are areas with a very fine mesh.

is below the yield point. The results from the bicrystal simulations are read along the line Q-Q (Fig. 3.1b), which spans the entire width of the α-phase. The results from the platelet simulations are read along the line P-P (Fig. 3.2b), which spans the entire width of the center α-phase platelet only.

The elastic anisotropy of the system suggests orientation dependence in the mechanical response hence we systematically adjust the relative orientation of the loading axis and the α-β interface (which we call the "loading orientation") as well as the relative orientation of the loading axis and the c-axis of the hexago-

nal close packed α-phase (which we call the "crystallographic orientation"). Dual phase α-β Ti alloys maintain an approximate $(\bar{5}140)_\alpha||(\bar{3}34)_\beta$ interface plane and a $\langle 1\bar{2}10\rangle(0001)_\alpha||\langle 1\bar{1}1\rangle(110)_\beta$ Burgers orientation relationship (BOR) which establishes a limited set of independent crystallographic and loading orientations for the system. Our previous work explored a scenario with the loading direction perpendicular to the interface plane normal and the c-axis of the HCP α-phase oriented at 45° to the loading direction [18] while our current effort includes a wide range of loading and crystallographic orientations. We vary the loading orientation by rotating the interface plane in 10° increments (green arrow in Figure 3.3) between 0° and 90° beginning with the loading direction perpendicular to the interface plane normal and finishing with the loading direction parallel to the interface plane normal. For each loading orientation we vary the crystallographic orientation of the α and β-phases in 10° increments (red arrow in Figure 3.3) between 0° and 90° beginning with the c-axis of the HCP α-phase in the x'-y' plane and finishing in the x'-z' plane; the β-phase is rotated in lockstep with the α-phase owing to the BOR. Variation of both loading orientation and crystallographic orientation in 10° increments yields 91 simulations each for the bicrystal and platelet microstructures. The finite element model and mesh size/shape near α-β interface are identical for all loading orientations to maintain consistency; however, the mesh characteristics far from the interface vary between models as necessary to accommodate the different geometries.

The 91 combinations of loading and crystallographic orientations are represented on one quarter of the α (0001) stereographic projection in Figure 3.4 by

39
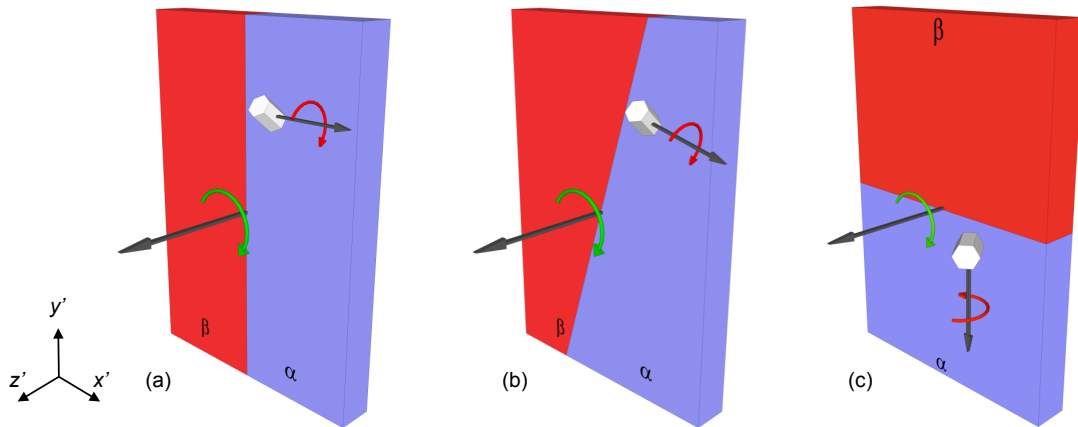
Figure 3.3: Schematic of the rotation scheme used in this study. The interface plane is rotated in $10°$ increments from the y'-z' plane to the x'-z' plane, as indicated by the green arrow. As examples, 3 of the 9 interface plane rotations are shown: (a) $0°$ (b) $30°$ and (c) $90°$. For each interface plane rotation, the c-axis direction of the HCP α-phase is rotated in $10°$ increments from the x'-y' plane to the x'-z' plane (red arrow).

indicating the orientation of the loading axis (y'). The green and red arrows in Figure 3.4 correspond to the green and red arrows shown in Figure 3.3; as the loading orientation changes, the y'-axis shifts in 10° increments "down" the stereographic projection until it is parallel with the interface plane and the ($5\bar{1}\bar{4}0$) pole. As the crystallographic orientation changes, the y' axis shifts in 10° increments "left" on the stereographic projection until it is perpendicular to the (0001) pole. The positions of the x'- and z'-axes also change with each scenario but these are not shown for simplicity. The simulations performed during this study required a variety of crystallographic calculations such as rotating elastic compliance matrices, measuring angles between directions and planes within a dual-phase system, and calculating resolved shear stresses. The detailed calculation techniques for these operations are described in Appendix A.

3.1.2 Calculation of Resolved Shear Stress

The finite element simulation of each loading/crystallographic orientation generates the stress state of the model at each node reported in the (x', y', z') coordinate system from Figures 1 and 2. To explore the interaction stresses in the α-phase, we extract the stress state along line Q-Q (bicrystal) or line P-P (platelet) (these lines remain perpendicular to the α-β interface as the models are rotated). The resolved shear stress on the each of independent slip and twinning systems in Table 3.1 is determined by rotating from the (x', y', z') coordinate system to a new coordinate system with the x-direction parallel to the slip/twinning direction and
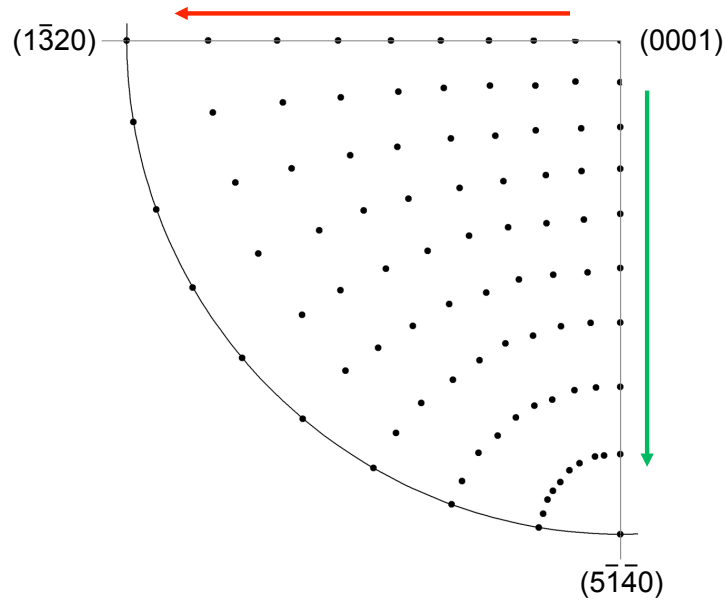
Figure 3.4: Orientation of the loading axis (y') for each of the 91 loading and crystallographic orientation combinations simulated in this study, shown on one quarter of the α (0001) stereographic projection. Each step in the green arrow direction represents a 10° rotation of the interface plane relative to the loading axis. Each step in the red arrow direction represents a 10° rotation of the c-axis of the α-phase relative to the loading axis. The arrow colors correspond to the arrows shown in Figure 3.3.

the z-direction parallel to the slip/twinning plane normal; the resolved shear stress is then the value of the xz shear stress (σ_{xz}) in the new coordinate system. For each loading/crystallographic orientation we then identify the independent system within each slip and twinning system with the highest resolved shear stress. Specifically, for a simulation represented by a single orientation in Figure 3.4 we find the basal $\langle a \rangle$ slip system with the highest resolved shear stress, the prismatic $\langle a \rangle$ slip system with the highest resolved shear stress, the pyramidal $\langle a \rangle$ slip system with the highest resolved shear stress, the pyramidal $\langle c+a \rangle$ slip system with the highest resolved shear stress, the $(10\bar{1}2)$ twinning system with the highest resolved shear stress, and the $(11\bar{2}1)$ twinning system with the highest resolved shear stress. The resolved shear stresses from the FEM calculations are then used to calculate the effective Schmid factor, S_{eff} following equation 3.2. An example result for a single simulation (a single point in Figure 3.4) using the platelet model is shown in Figure 3.5 where the x-axis is the unit distance along line P-P across the center platelet. The dotted lines show the effective Schmid factor calculated from FEM results using equation 3.2, which varies with distance from the α-β interface owing to the decay of the interaction stress [18, 39]; the solid lines show the standard Schmid factor, calculated using equation 3.1, which is determined geometrically and is therefore constant for a given loading/crystallographic orientation and independent slip or twinning system. The magnitude of S_{int} is shown as colored arrows next to the y-axis based on the difference between the effective Schmid factor and the standard Schmid factor. In Figure 3.5 it is evident that the interaction stress resolves significantly onto the pyramidal $\langle a \rangle$ and prismatic $\langle a \rangle$ systems with a smaller effect on other mechanisms

Table 3.1: α-Ti slip and twinning systems included in this study

Deformation Mode	Deformation Plane	Deformation Direction	Number of Independent Systems
Basal $\langle a \rangle$ Slip	$\{0001\}$	$\langle 1\bar{2}10 \rangle$	3
Prismatic $\langle a \rangle$ Slip	$\{10\bar{1}0\}$	$\langle 1\bar{2}10 \rangle$	3
Pyramidal $\langle a \rangle$ Slip	$\{10\bar{1}1\}$	$\langle 1\bar{2}10 \rangle$	6
Pyramidal $\langle c + a \rangle$ Slip	$\{10\bar{1}1\}$	$\langle \bar{1}\bar{1}23 \rangle$	12
$(10\bar{1}2)$ Twinning	$\{10\bar{1}2\}$	$\langle \bar{1}011 \rangle$	6
$(11\bar{2}1)$ Twinning	$\{11\bar{2}1\}$	$\langle \bar{1}\bar{1}26 \rangle$	6

for this particular orientation.

Similar calculations are performed for each of the 91 loading/crystallographic orientations. We consolidate the results for all of the orientations by plotting S_{eff} as a function of stress axis (y') on the α (0001) stereographic projection as shown in Figures 3.6 (a)–(f) (bicrystal) and 3.7 (a)–(f) (platelet). The magnitude of the interaction stress, S_{int}, as a function of loading and crystallographic orientation is shown in Figure 3.8 (a)–(f). Results for S_{int} are only shown for the platelet microstructure; the bicrystal interaction stress results are very similar.

Tables 3.2 and 3.3 provide a summary of the maximum value of S_{eff} across all orientations for each slip and twinning system, along with the corresponding value of S_{int} and the interaction contribution as a percentage of the total.
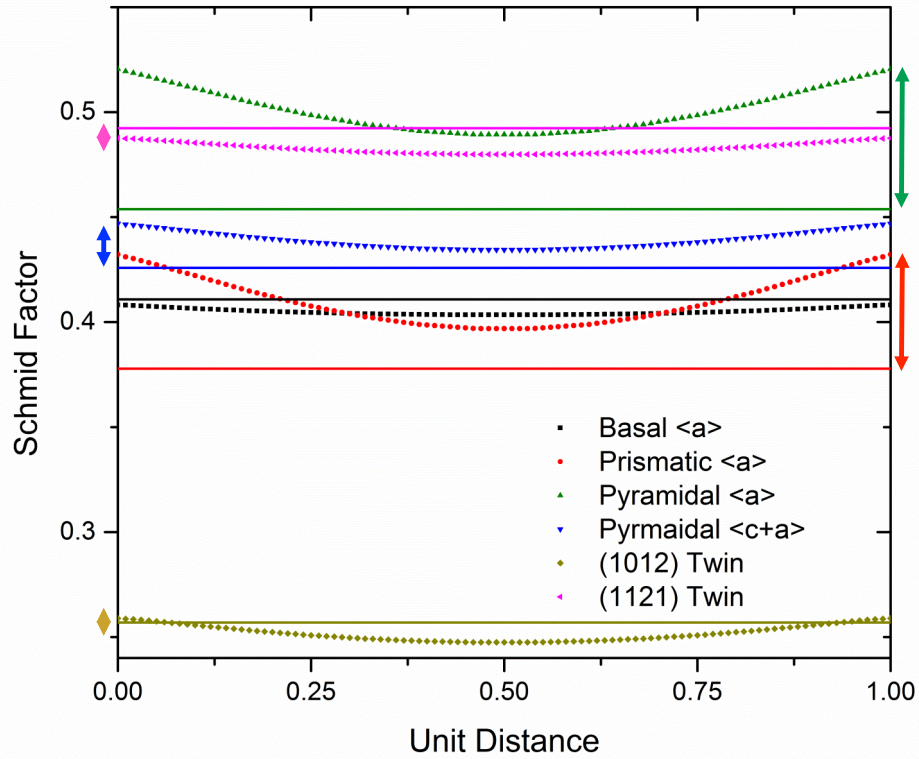
Figure 3.5: Schmid factor (solid lines) as defined in equation 3.1 and effective Schmid factor (symbols) as defined in equation 3.2, versus unit distance along line P-P (across the center platelet) in the platelet microstructure. Colored arrows indicate the magnitude of S_{int} at the α-β interface.
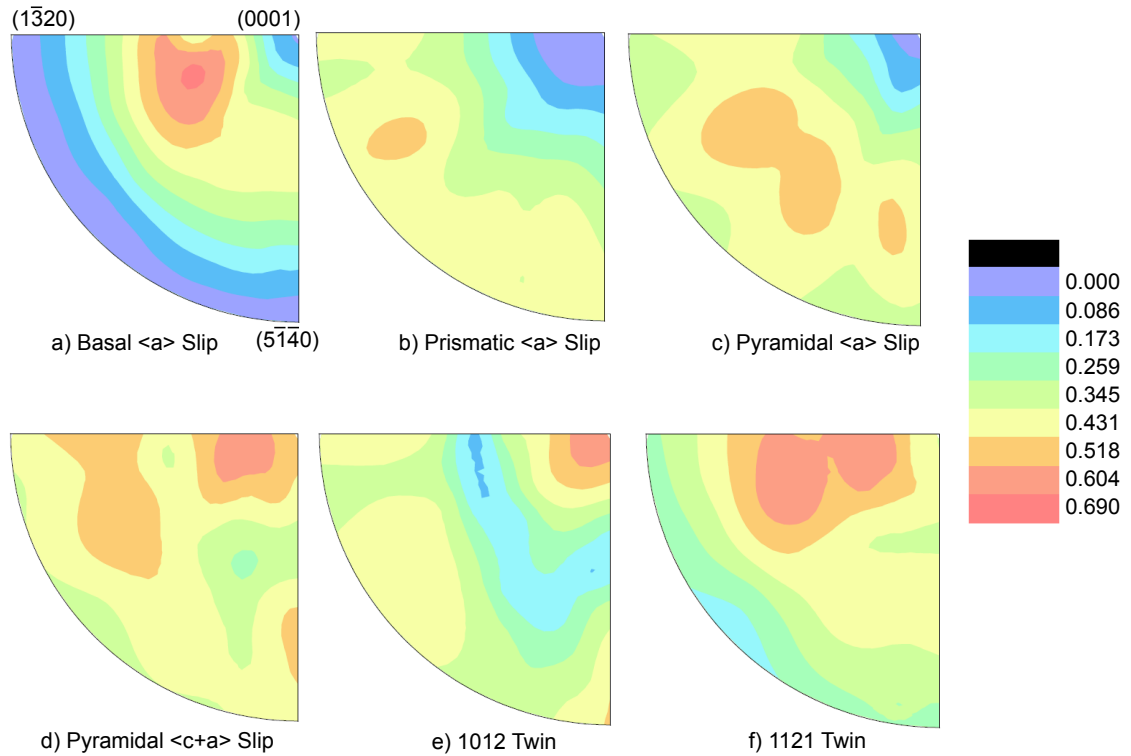
Figure 3.6: Bicrystal microstructure results showing effective Schmid factor, S_{eff}, for each slip and twinning system plotted as a function of loading axis (y') on one quarter of the α (0001) stereographic projection.
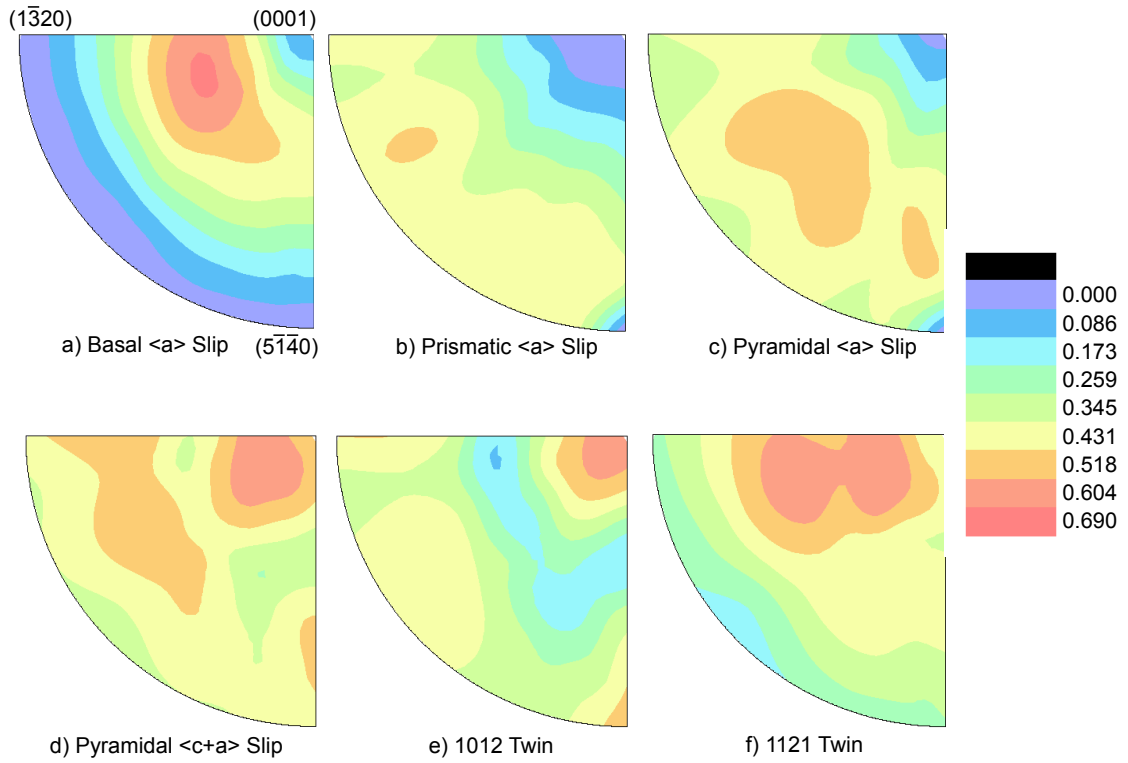
Figure 3.7: Platelet microstructure results showing effective Schmid factor, S_{eff}, for each slip and twinning system plotted as a function of loading axis (y') on one quarter of the α (0001) stereographic projection.
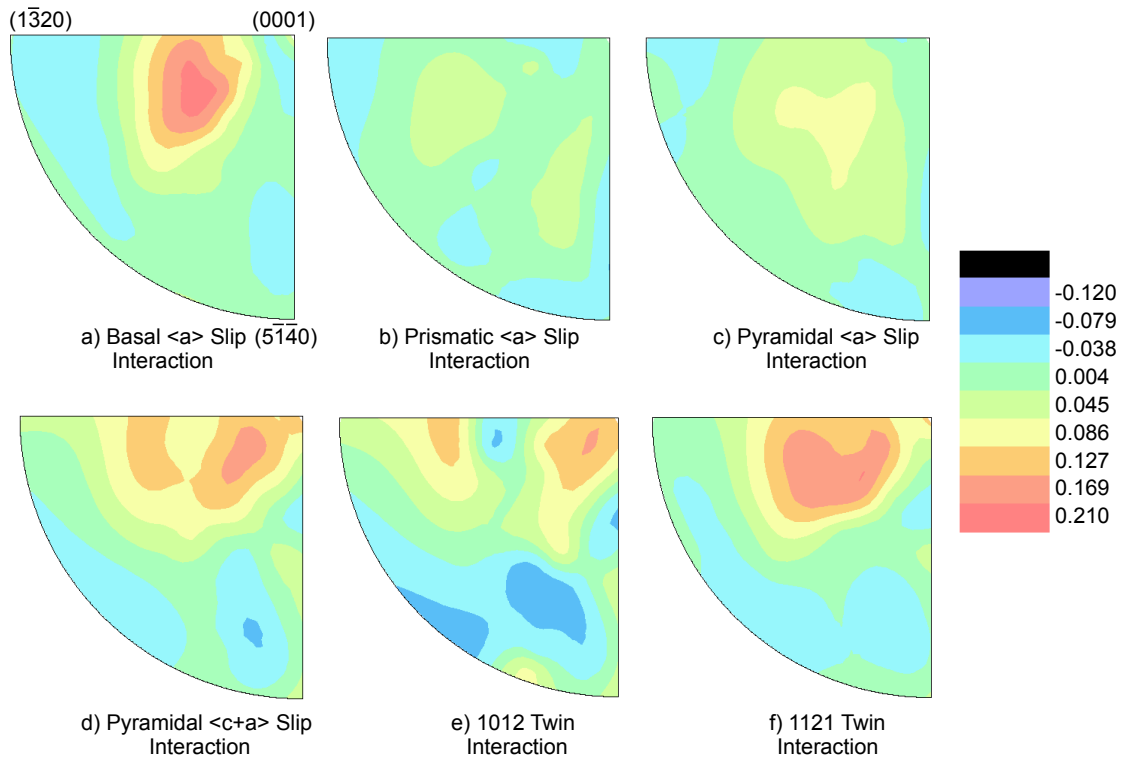
Figure 3.8: Platelet microstructure results showing the interaction stress contribution to the effective Schmid factor, S_{int}, for each slip and twinning system plotted as a function of loading axis (y') on one quarter of the α (0001) stereographic projection.

Table 3.2: Bicrystal results summary showing the maximum value of the effective Schmid factor, S_{eff}, for each slip and twinning system, the contribution from the applied stress, S_{app}, the contribution from the interaction stress, S_{int}, and the percentage of the total S_{eff} that is due to S_{int}

Deformation System	Max S_{eff}	S_{app}	S_{int}	Interaction Stress Contribution (%)
Basal $\langle a \rangle$ Slip	0.690	0.494	0.196	28.4
Prismatic $\langle a \rangle$ Slip	0.521	0.482	0.039	7.4
Pyram. $\langle a \rangle$ Slip	0.567	0.487	0.080	14.0
Pyram. $\langle c + a \rangle$ Slip	0.663	0.494	0.169	25.4
$(10\bar{1}2)$ Twinning	0.652	0.498	0.154	23.6
$(11\bar{2}1)$ Twinning	0.681	0.493	0.188	27.6

Table 3.3: Platelet results summary showing the maximum value of the effective Schmid factor, S_{eff}, for each slip and twinnig system, the contribution from the applied stress, S_{app}, the contribution from the interaction stress, S_{int}, and the percentage of the total S_{eff} that is due to S_{int}

Deformation System	Max S_{eff}	S_{app}	S_{int}	Interaction Stress Contribution (%)
Basal $\langle a \rangle$ Slip	0.708	0.494	0.214	30.2
Prismatic $\langle a \rangle$ Slip	0.517	0.482	0.035	6.8
Pyram. $\langle a \rangle$ Slip	0.576	0.492	0.084	14.6
Pyram. $\langle c+a \rangle$ Slip	0.686	0.495	0.191	27.8
$(10\bar{1}2)$ Twinning	0.653	0.498	0.155	23.7
$(11\bar{2}1)$ Twinning	0.676	0.461	0.215	31.8

3.2 Plastic Interaction Stress During the Onset of Deformation in the α-Phase

As the applied stress increases and a dual-phase Ti alloy begins to deform plastically, interaction stresses again play a role in promoting and suppressing different deformation mechanisms. The yield stress in the α-phase is typically much lower than the yield stress in the β-phase. For example, in our earlier work we heat treated a dual-phase α-β Ti-8.1 V (wt%) alloy such that the composition of the α-phase was Ti-1.6V and the composition of the β-phase was Ti-14.8V; in separate experiments we produced single phase α samples with composition Ti-1.6V, finding the yield stress to be 350 MPa [15], and single phase β samples with composition Ti-14.8V, finding the yield stress to be 900 MPa [43]. Hence under increasing load the yield stress in the α-phase is met while the β-phase is still deforming elastically, leading to plastic-elastic interaction stresses between the phases. The presence of the α-β phase boundary affects dislocation glide as well as twin nucleation and growth due to the elastic mismatch between the phases. As a dislocation in a low shear modulus material moves towards the boundary with a high shear modulus material, the dislocation experiences a repulsive image force imposed across the interface [44]; conversely, the image force is attractive for the case of a dislocation moving in a high shear modulus material towards the barrier with a low shear modulus material. Twin nucleation and growth is similarly affected, experiencing a repulsive/attractive force when nucleated at the barrier with a higher/lower shear modulus material (re-

spectively). Conceptually, this behavior stems from the energy cost of the strain field due to the dislocation or twin; strain energy (per unit strain) increases with shear modulus, and thus imparting the strain field from a defect partly onto a high shear modulus material increases energy of the system (and thus creates a repulsive force) while the opposite is true for a strain field imparted onto a low shear modulus material. In order to incorporate this effect into our calculations, we determine the barrier stress τ_B that each independent slip and twinning system experiences as a result of the α-β phase boundary.

3.2.1 Interaction of Dislocations with the α-β Interface

Stress fields due to dislocation interactions with a phase boundary have been studied for many decades, including early work by Head which suggested that the applied shear stress necessary to hold a dislocation in equilibrium at a distance c from a phase boundary increases with $1/c$ [45]; however this results in infinite stress for a dislocation at the interface. Using a perturbation analysis, Pacheco and Mura [46] determined that the resolved shear stress necessary to hold a dislocation at the interface of two phases, τ_{DB}, is a function of the shear moduli of the phases as

$$\tau_{DB} = -\frac{2KG_1}{\pi^2} \tag{3.4}$$

where

$$K = \frac{G_2 - G_1}{G_1 + G_2} \tag{3.5}$$

and G_i is the shear modulus of phase i. Thorough analysis of the Pacheco-Mura model demonstrates that the value of τ_{DB} is largely insensitive to the angle between

52

the dislocation line and the interface, and the model is effective for values of K up to 0.3 [47]. Further, atomistic studies of dislocation-boundary interactions produce values of τ_{DB} comparable to the Pacheco-Mura model [48].

Frequently shear modulus is treated as an isotropic property, which suggests that dislocations would always experience an attractive force when moving from the high modulus α-phase to the low modulus β-phase. However, shear modulus is anisotropic at the single crystal level of the interface between the α- and β-phases. In order to capture the effects of crystallographic anisotropy on the interaction of dislocations across the α-β interface, we include the variation in shear modulus of both phases as a function of orientation while incorporating the crystallographic alignment of the phases due to the BOR. The shear modulus for an arbitrary direction in the α-phase, G_{θ}^{α}, is given as a function of the elastic constants, s_{ij}, and the angle θ between the [0001] direction (for which the s_{ij} are reported) and the arbitrary direction as [49]

$$G_{\theta}^{\alpha} = [s_{44} + (s_{11} - s_{12} - \frac{1}{2}s_{44})(\sin^2 \theta) + 2(s_{11} + s_{33} - 2s_{13} - s_{44})(\cos^2 \theta \sin^2 \theta)]^{-1} \quad (3.6)$$

The shear modulus for an arbitrary direction $[hkl]$ in the β-phase, G_{θ}^{β}, is given by [50]

$$G_{\theta}^{\beta} = [s_{44} + 4(s_{11} - s_{12} - \frac{1}{2}s_{44})\Gamma]^{-1} \quad (3.7)$$

where Γ is

$$\Gamma = \frac{h^2k^2 + h^2l^2 + k^2l^2}{(h^2 + k^2 + l^2)^2} \quad (3.8)$$

Incorporating the values of G_{θ}^{α} and G_{θ}^{β} for each slip direction in the α-phase (and the parallel direction in the β-phase, as defined by the BOR) into equation 3.4

produces direction-specific values of τ_{DB}. For most directions the value of G_θ^α is greater than the value of G_θ^β, resulting in a positive τ_{DB} (dislocations are attracted to the interface). This attractive interaction stress extends for only about 10 lattice spacings [46] and we therefore suggest that the α-β interface does not dramatically affect dislocation motion for independent slip systems where $G_\theta^\alpha > G_\theta^\beta$; dislocations in α are able to approach the interface without any particular resistance until they are very close, at which point they are attracted to the interface. However, for some independent slip systems the value of G_θ^α is less than the value of G_θ^β, resulting in a negative value for τ_{DB} (dislocations are repelled by the interface). In these slip systems, dislocations in the α-phase require resolved shear stress τ_{DB} in addition to the critical resolved shear stress for dislocation motion in order to slip to the interface between the phases. While the range of the repulsive interaction stress is only about 10 lattice spacings, we suggest that the pileup of dislocations against this interaction stress causes the active slip system to harden quickly, making slip unlikely until after the barrier is overcome. Table 3.4 lists the 12 slip systems for which τ_{DB} is negative, indicating that $G_\theta^\alpha < G_\theta^\beta$ and that the α-β interface repels dislocations slipping on the indicated slip system.

Only 12 of the 24 independent slip systems in α Ti are shown in Table 3.4; for the remaining 12 systems $G_\theta^\alpha > G_\theta^\beta$ and there is only a very short range attractive force between the α-β interface and a dislocation. Of particular note is the distribution of which slip modes are most affected by the elastic-plastic interaction across the α-β interface. Only 4 of the 12 independent slip systems with a Burgers vector in the basal plane (e.g. $\langle a \rangle$ type) are repelled by the interface, requiring approxi-

Table 3.4: The independent slip systems in α for which the shear modulus in the α-phase, G_θ^α, is less than the shear modulus in the parallel direction in the β-phase, G_θ^β, repelling the dislocation and requiring an additional resolved shear stress $-\tau_{RSS}$ in order for the dislocation to slip to the interface.

Slip System	τ_{DB} (MPa)
Basal $\langle a \rangle (0001)[11\bar{2}0]$	-149.6
Prismatic $\langle a \rangle (1\bar{1}00)[11\bar{2}0]$	-149.6
Pyramidal $\langle a \rangle (1\bar{1}01)[11\bar{2}0]$	-149.6
Pyramidal $\langle a \rangle (\bar{1}101)[\bar{1}\bar{1}20]$	-149.6
Pyramidal $\langle c + a \rangle (01\bar{1}1)[1\bar{2}13]$	-631.2
Pyramidal $\langle c + a \rangle (\bar{1}101)[\bar{2}\bar{1}\bar{1}3]$	-870.3
Pyramidal $\langle c + a \rangle (0\bar{1}11)[\bar{1}2\bar{1}3]$	-631.2
Pyramidal $\langle c + a \rangle (1\bar{1}01)[\bar{2}113]$	-870.3
Pyramidal $\langle c + a \rangle (10\bar{1}1)[\bar{2}113]$	-870.3
Pyramidal $\langle c + a \rangle (\bar{1}101)[1\bar{2}13]$	-631.2
Pyramidal $\langle c + a \rangle (01\bar{1}1)[1\bar{2}13]$	-631.2
Pyramidal $\langle c + a \rangle (\bar{1}011)[2\bar{1}\bar{1}3]$	-870.3
Pyramidal $\langle c + a \rangle (1\bar{1}01)[\bar{1}2\bar{1}3]$	-631.2

mately 150 MPa of additional resolved shear stress in order to slip to the interface. However, 9 of the 12 independent slip systems with a Burgers vector that contains a c-axis component (e.g. $\langle c+a \rangle$ type) are repelled by the interface, requiring between 630 MPa and 870 MPa of additional resolved shear stress in order to slip to the interface. The α-β interface and the the anisotropy of the shear moduli in the α and β-phases thus result in two significant effects. First, anisotropy is expected within each slip system, for example making slip on the basal $\langle a \rangle$ $(0001)[11\bar{2}0]$ system more difficult while having little effect on the remaining two basal $\langle a \rangle$ systems as is observed experimentally [51, 52, 53]. Second, the interaction stress suppresses $\frac{3}{4}$ of the independent pyramidal $\langle c + a \rangle$ slip systems, which require additional resolved shear stress in excess of 600 MPa in order to slip to the interface. The latter effect is notable in particular because the pyramidal $\langle c + a \rangle$ system is the only slip system in α-Ti that is able to accommodate extension and contraction along the c-axis direction. By making slip with a c-axis component more difficult, deformation by twinning (which includes a c-axis component) may occur more readily in order to accommodate plastic deformation of the dual-phase material.

3.2.2   Interaction of Deformation Twins with the α-β Interface

Deformation twins introduce complicated stress fields in a material during deformation. While analytical solutions exist for stress due to twinning in an infinite matrix [54, 55], no such solutions exist for the stress field due to a twin near the boundary between two phases. Twin formation occurs via an eigenstrain, a stress-free strain

in the absence of a surrounding media, similar to a phase change or thermal expansion. However, deformation twins are surrounded by a matrix which results in a backstress in the twin and a forward stress in the matrix, illustrated in Figure 3.9. The backstress operates against the formation of the twin, modifying the critical resolved shear stress for twin growth as

$$\tau_{CRSS} = \tau_{DCRSS} + \tau_{BS} \qquad (3.9)$$

where τ_{CRSS} is the critical resolved shear stress for twinning, τ_{DCRSS} is the critical resolved shear stress necessary to move the twinning dislocations, and τ_{BS} is the backstress [56]. Similar to the above analysis of the effects of the phase boundary on dislocation motion, we study twin formation in an isotropic elastic medium using the values of G_θ^β is and G_θ^α that correspond to each independent twinning system. However, given the complexity of the twinning stress fields we rely on FEM models to extract values for τ_{BS}, again using ANSYS® Release 11.0 and SOLID186 elements (hexahedral 20-node quadratic elements).

First, we test a general approach for simulating twinning and capturing the correct backstress using FEM models by comparing to Eshelby's analytical solution for a oblate ellipsoidal volume undergoing shear eigenstrain in an infinite matrix [54, 55]. We model the twin as an oblate ellipsoidal volume that is 10 units on its long axis with a 10:1 aspect ratio, placed in the center of a cubic volume that is 100 units on each side. The nodes at $x = 0$ are constrained to 0 displacement in the x-direction, while the nodes at $x = 100$ (the opposite face of the cube) are coupled to all displace the same amount in the x-direction; the y- and z- cube faces are similarly
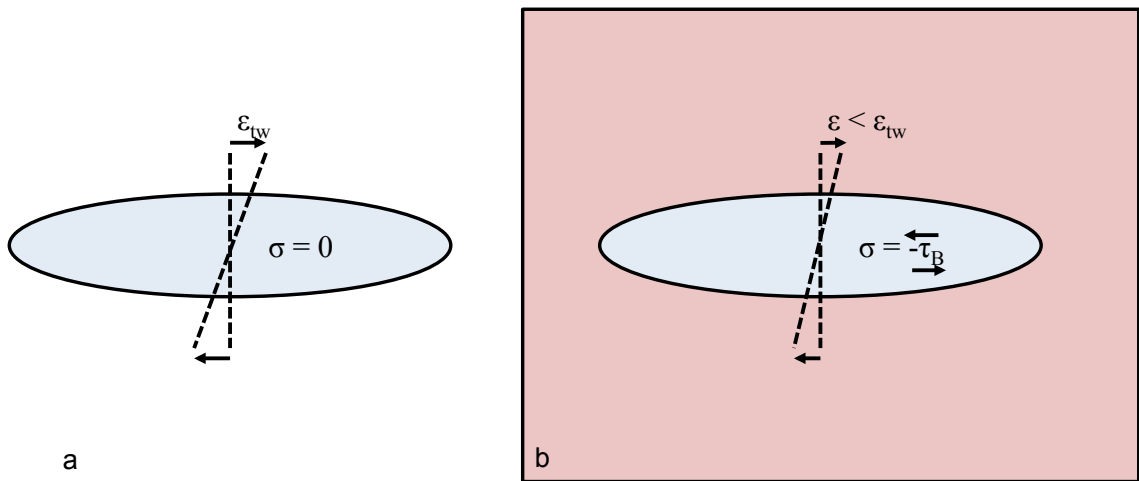
Figure 3.9: Schematic illustration of the source of backstress during twinning. a) A twin without a surrounding parent material undergoes a stress-free eigenstrain ϵ_{tw}. b) The same twin as a), surrounded by a parent material which constrains the twin and imposes a backstress $-\tau_B$ where the negative sign indicates that the stress works against the direction of ϵ_{tw}.

constrained in the y- and z- directions, respectively. The shear modulus for both the twin and matrix is set to 42 GPa, however the twin volume is also assigned thermal expansion characteristics which produce the correct twinning eigenstrain when the temperature of the model is raised to a certain point; the matrix material is not assigned thermal expansion properties and does not respond to the change in temperature; full details on the implementation of this technique are provided in Appendix B. Eshelby's solution [54, 55] for the backstress in this scenario is -1170.70 MPa while our FEM model estimates a backstress of -1174.8 MPa (the sign of the stress indicates that it works against the direction of twinning). The FEM approach and model constraints thus yield an error of less than 0.5% compared to the analytical solution, however the low aspect ratio results in unrealistically high values of backstress. Increasing the aspect ratio of the ellipsoid requires significantly more computational effort due to the meshing requirements; further, the shape of a twin nucleus near a phase boundary is not known to be exactly ellipsoidal. Thus for our study of the effect of the α-β interface on twinning backstress, we use a pseudo-ellipsoidal twin model shown in Figure 3.10 where the twin volume is a double-wedge with a 40:1 aspect ratio in the twinning direction. The additional barrier to twin growth due to the α-β interface, τ_{BT}, is the difference in backstress τ_{BS} between a twin in an infinite matrix and a twin near the interface between the two phases.

As with the dislocation-interface model described above, we calculate the values of G_θ^α and G_θ^β for each of the independent $\{10\bar{1}2\}$ twin systems in Ti; the $\{11\bar{2}1\}$ twin is omitted from these calculations as it was not observed in our experiments nor was it subjected to the highest effective Schmid Factor system for any of the orienta-
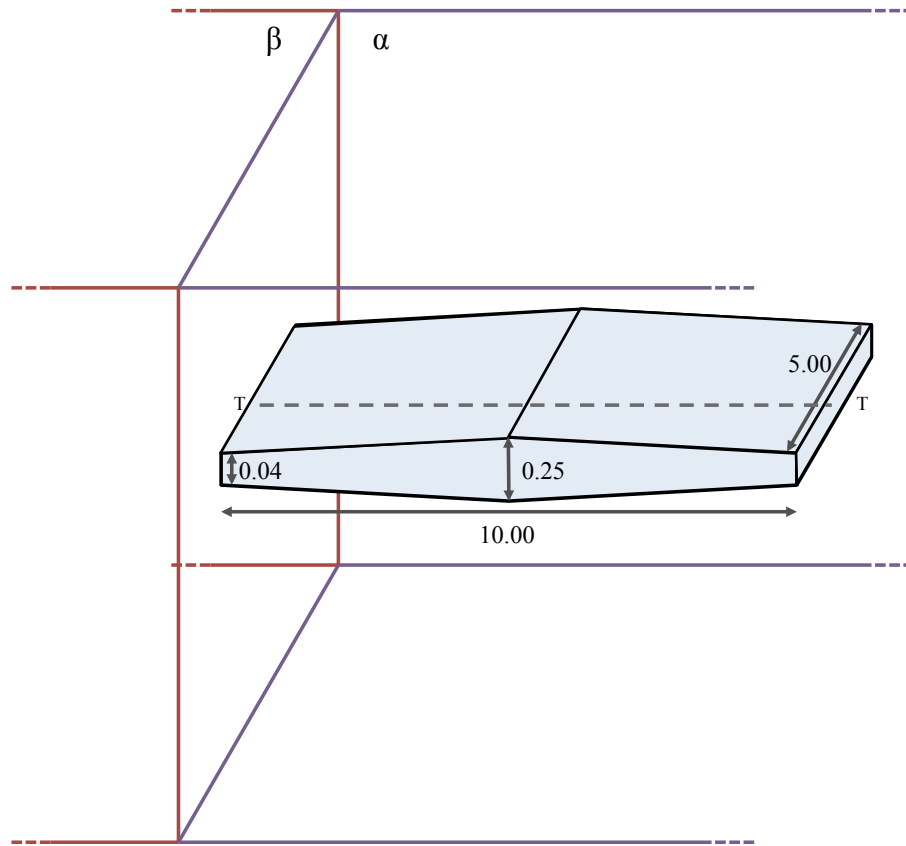
Figure 3.10: Pseudo-ellipsoidal twin shape and dimensions used for FEM simulations of twinning backstress τ_{BS}, including line T-T which spans the center of the twin. The dimensions of the α-β interface are not to scale.
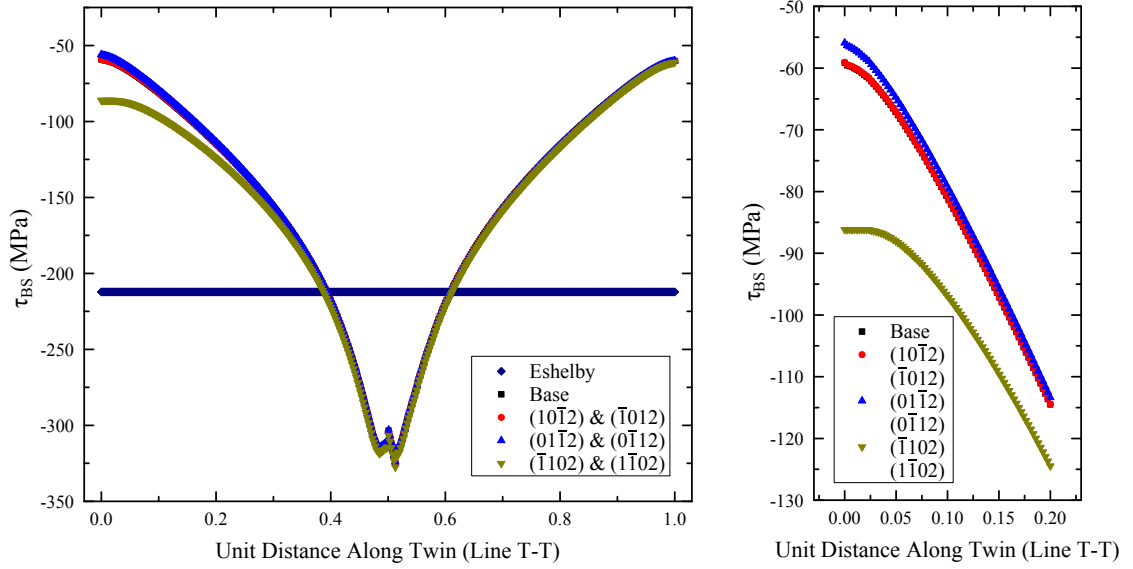
Figure 3.11: a) Backstress in a twin due to the α-β interface measured along line T-T (Figure 3.10) along with Eshelby's solution [55] for a comparable perfect oblate ellipsoid in an infinite matrix. b) Close-up view of a) showing backstress for the section of the twin closest to the α-β interface.

tions tested during the elastic interaction stress calculations. Table 3.5 summarizes the FEM simulation settings and results, including a "base" case scenario where $G_\theta^\alpha = G_\theta^\beta$, thereby approximating twinning in an infinite matrix. The backstress as a function of distance along line T-T (Figure 3.10) is reported in Figure 3.11 along with the analytical result for a perfect oblate spheroid of comparable size in an infinite matrix with shear modulus matching the base case simulations.

These calculations yield several interesting results. First, the pseudo-ellipsoidal twin produces backstress values reasonably similar to the perfect ellipsoidal results at much lower computational cost. Second, we see that the backstress on the twin is only affected at short distances from the interface and that the magnitude of the

Table 3.5: Summary of FEM twinning simulation settings and results

Simulation	G_θ^α (GPa)	G_θ^β (GPa)	τ_{BS} (MPa)	τ_{BT} (MPa)
Base	26.43	26.43	-59.17	0.00
$(10\bar{1}2)[\bar{1}011]$	26.43	26.38	-59.06	-0.10
$(01\bar{1}2)[0\bar{1}11]$	26.43	25.10	-55.92	-3.25
$(\bar{1}102)[1\bar{1}01]$	26.43	41.95	-86.17	27.01
$(\bar{1}012)[10\bar{1}1]$	26.43	26.38	-59.06	-0.10
$(0\bar{1}12)[01\bar{1}1]$	26.43	25.10	-55.92	-3.25
$(1\bar{1}02)[\bar{1}101]$	26.43	41.95	-86.17	27.01

effect is quite modest. The barrier to twin growth due to the α-β interface ranges from about -3 MPa (twinning is made easier) to about 27 MPa (twinning is made more difficult); this barrier only exists near the interface and thus as the twin grows beyond an initial nucleus it will no longer experience much influence.

3.3   Activation of Deformation Modes

Finally, we combine the effects of elastic and plastic interaction stresses in order to understand the overall impact of the α-β interface on the onset of deformation in dual-phase Widmanstätten Ti alloys. To determine the impact of interaction stresses on the activation of the deformation mechanisms we must incorporate critical resolved shear stress (CRSS); for this study we use the CRSS ratio, which we define as the ratio of the CRSS for a given deformation mode to the CRSS for pris-

matic $\langle a \rangle$ slip. Reported values of the CRSS for slip and twinning in α-Ti vary with the characteristics of the material and the measurement technique so we must first determine appropriate ratios. The model material for this study is Ti-8.1V (wt%) owing to our existing experimental data [13, 57].

Alloy chemistry is known to have a significant impact on the critical resolved shear stress for slip in α-Ti. The addition of Al, which is a solid solution strengthening element in Ti, increases the CRSS for prismatic [58] and basal [59] slip except at additions below 1 at% where moderate softening is observed. The CRSS ratio of basal $\langle a \rangle$ slip to prismatic $\langle a \rangle$ slip is significantly affected by alloying additions [59] and is expected to be near 1 for alloys containing solid solution strengthening elements such as Al, Mn, and V. Reported values for the CRSS ratio of pyramidal $\langle c+a \rangle$ slip to prismatic $\langle a \rangle$ slip vary considerably but are generally lower for alloyed systems when compared to pure Ti. Jones [60] suggests that the CRSS for pyramidal $\langle c+a \rangle$ slip depends on both shear and hydrostatic stress, increasing the effective CRSS by 30% for tensile versus compressive loading; our study only considers tensile loading so this effect is ignored. The strain rate sensitivity of CRSS is modest for TiAl alloys between 1 and 6 at% at room temperature and is not considered here [58, 61]. Alloy purity also has a significant impact on the magnitude of critical resolved shear stress for slip, particularly when considering interstitial elements such as oxygen, nitrogen, and carbon [58]. However the CRSS ratio between systems is generally not affected and hence impurity effects are not considered here.

Despite the significant contribution of twinning to the deformation behavior of Ti alloys [28], the mechanisms of twin nucleation and growth are not fully under-

stood. This lack of understanding has inhibited development of critical conditions for twinning and the use of a critical resolved shear stress criterion for twinning is debated. Mechanical testing of single crystal, pure Ti specimens at different orientations yielded significant variation in the measured CRSS for twinning [61]; however, mechanical testing of polycrystalline, Ti alloy specimens tested at different orientations suggests much smaller variation in CRSS [62]. Fitting crystal plasticity models to mechanical test results during creep of polycrystalline, pure Ti specimens indicates that the CRSS values for both $\{10\bar{1}2\}$ and $\{11\bar{2}1\}$ twinning modes are approximately the same [63, 64].

In all cases, the method used for measuring CRSS can impact the result. Mechanical testing of Ti or Ti alloy single crystals has been used by many researchers to determine CRSS however this method is susceptible to experimental error due to crystal misalignment, activity of multiple systems, and measurement inaccuracy. Crystal plasticity (CP) models have also been used to determine deformation resistance parameters that are analogous to CRSS though they include other artifacts [65]. For example, several crystal plasticity approaches use a Taylor plasticity assumption where the strain is uniform within grains of a particular phase [63, 64]. This approach allows for improved computational efficiency and produces reasonably accurate bulk deformation predictions, however CRSS values determined from Taylor-type crystal plasticity models may be artificially high (or low) if the actual strain distribution within the grains inhibits (or promotes) slip on a particular slip system. While the magnitude of CRSS values calculated using CP techniques generally do not match experimental results from single crystal tests, the ratios still

provide insight to the relative difficulty of activating deformation modes and are therefore included here.

A summary of several reported CRSS ratios is provided in Table 3.6. While the ratios vary by material characteristics and measurement technique, we must estimate appropriate CRSS ratios for this study in order to demonstrate the effects of interaction stresses on preferred deformation mode. This is particularly problematic for twinning and $\langle c+a \rangle$ pyramidal slip where non-Schmid deformation criteria may exist. In our own tests we found prismatic $\langle a \rangle$ slip and $\{10\bar{1}2\}$ twinning to be prevalent, while other deformation modes were rarely found [13, 57]; this suggests that for our model system basal $\langle a \rangle$ slip is somewhat more difficult that prismatic $\langle a \rangle$ slip, and $\{10\bar{1}2\}$ twinning is somewhat easier than $\{11\bar{2}1\}$ twinning. After consideration of the discussion above, we applied the CRSS ratios shown in Table 3.7.

Table 3.6: Summary of the reported critical resolved shear stress ratios in α-Ti. Values are normalized to the CRSS for prismatic $\langle a \rangle$ slip. The detail column indicates the chemistry, where Ti64 is T-6Al-4V (wt%), sc indicates measured from a single crystal, pc indicates measured from a polycrystal, mech. test indicates measured directly from a mechanical test using Schmid's Law, and cryst. pl. indicates fit to mechanical testing results using crystal plasticity modeling.

Prism. $\langle a \rangle$	Basal $\langle a \rangle$	Pyrm. $\langle a \rangle$	Pyrm. $\langle c+a \rangle$	$\{10\bar{1}2\}$ twin	$\{11\bar{2}1\}$ twin	Detail
1	2.2	-	-	-	-	Pure Ti, sc, mech. test[66]
1	-	-	-	1.83	1.1–3.5	Pure Ti, sc, mech. test[61]
1	1.32	-	5.32	5.76	5.76	Pure Ti, pc, cryst. pl.[63]
1	5	-	4	4.17	4.17	Pure Ti, pc, cryst. pl.[64]
1	1.16	1.06	1.66	-	-	Ti64, pc, mech. test[60]
1	1–2.5	-	4.2	-	-	TiAl, sc, mech. test[59]

Continued on next page

Table 3.6 – *Continued from previous page*

Prism. $\langle a \rangle$	Basal $\langle a \rangle$	Pyrm. $\langle a \rangle$	Pyrm. $\langle c + a \rangle$	$\{10\bar{1}2\}$ twin	$\{11\bar{2}1\}$ twin	Detail
1	-	1.64	< 2	-	-	Ti64, pc, cryst. pl.[67]
1	1	-	2.63	-	-	Ti64, pc, cryst. pl.[40]
1	1.7 - 2.0	-	2.8	1.3–1.9	-	TiAlV, pc, mech. test[62]
1	1.14	1.32	1.59	-	-	Ti64, pc, cryst. pl.[10]

Table 3.7: Critical resolved shear stress ratios for α-Ti used in this study. Values are normalized to the CRSS for prismatic $\langle a \rangle$ slip.

Prism. $\langle a \rangle$	Basal $\langle a \rangle$	Pyrm. $\langle a \rangle$	Pyrm. $\langle c + a \rangle$	$\{10\bar{1}2\}$ twin	$\{11\bar{2}1\}$ twin
1	2	3	3	1.6	2.5

Finally, we modify the CRSS ratio for each independent slip and twinning system in order to capture the plastic interaction stresses due to the α-β interface. In order to integrate our results for τ_{BD} (dislocation barrier stress) and τ_{BT} (twin

barrier stress), we use 60 MPa as the CRSS for prismatic $\langle a \rangle$ slip upon which the ratios are based [59, 66, 61]. The CRSS ratio for each independent system is adjusted from the value in table 3.7 based on the increase or decrease of CRSS due to the dislocation-boundary and twin-boundary interaction stresses calculated above.

The active deformation mechanism for each of the 91 orientations tested during elastic interaction stress calculations is the mechanism with the highest value of an activation parameter A_i, defined by

$$A_i = \frac{S_{eff}}{CRSS_{Ri}} \tag{3.10}$$

where S_{eff} is the effective Schmid Factor as defined in equation 3.2 and $CRSS_{Ri}$ is the CRSS ratio for deformation mechanism i. Results from elastic interaction stress calculations for each orientation contribute to the value of S_{eff}, while plastic interaction stress calculations contribute to the value of $CRSS_{Ri}$. Figure 3.12a provides the active deformation mechanism based only on the standard Schmid factor (S_{std}, equation 3.1) and thereby not accounting for elastic or plastic interaction stresses. Figure 3.12b provides the active deformation mechanism using the value of A_i, which includes elastic and plastic interaction stress.

It is important to note that while the CRSS ratios selected in table 3.7 have a significant effect on the active deformation mechanisms, they have a very minor effect on the differences observed between the standard Schmid factor results and the interaction stress results. For example, increasing the CRSS ratio for $(10\bar{1}2)$ twinning results in fewer orientations where $(10\bar{1}2)$ twinning is active in both Figures 3.12a *and* 3.12b, but the difference between the two is generally unchanged.
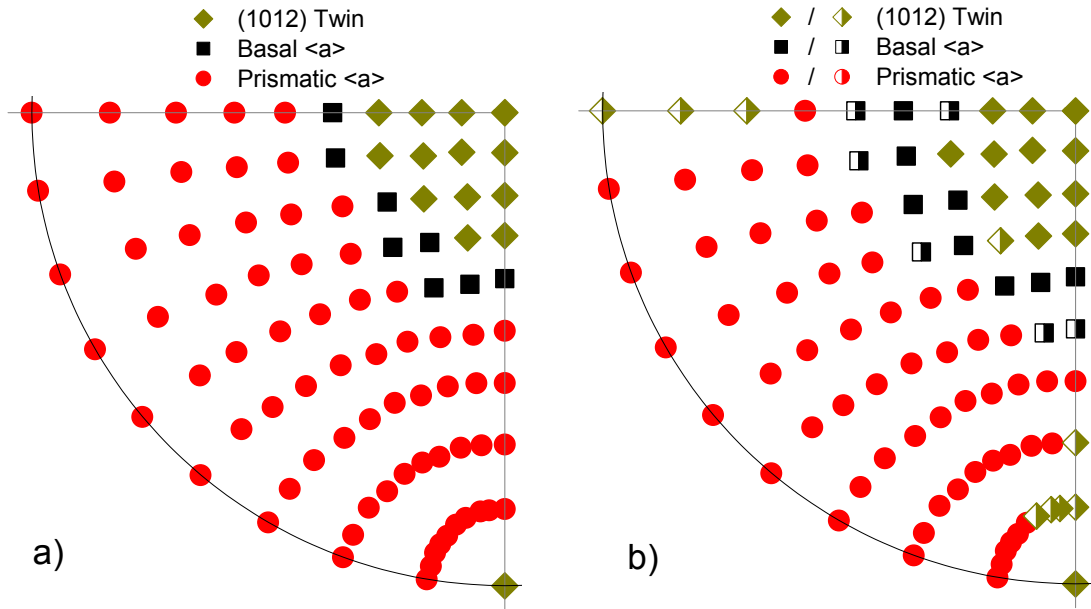
Figure 3.12: Deformation mechanisms activated at the lowest applied stress as a function of loading and crystallographic orientation. Results in a) are determined using the standard Schmid factor while results in b) include elastic and plastic interaction stress effects. Half-filled symbols indicate that the interaction stresses cause a change of deformation mechanism when compared to the standard Schmid factor result.

Similarly, $(1\bar{1}21)$ twinning along with pyramidal $\langle a \rangle$ and $\langle c + a \rangle$ slip are not observed in any orientation. Reducing the CRSS ratio for these mechanisms (as would be appropriate to model Ti alloy systems where they are observed experimentally) produces results with $(1\bar{1}21)$ twins, pyramidal $\langle a \rangle$ slip, and pyrmaidal $\langle c + a \rangle$ slip using standard Schmid analysis as well as when incorporating interaction stresses; however, the magnitude of the interaction stress effect on these deformation systems is comparable to the results in Figure 3.12.

3.4   Implications of Interaction Stress for Mechanical Behavior in α-β Ti Alloys

Overall, the results described above demonstrate two effects of elastic and plastic interaction stresses on the mechanical behavior of α-β Ti alloys during the onset of plastic deformation:

1. The effective Schmid Factor in the α-phase due to combined applied and elastic interaction stresses is generally larger than the standard Schmid factor. The magnitude of this increase can be up to 30% and the effect is anisotropic.

2. Elastic and plastic interaction stresses can change the preferred deformation mechanism, for example from prismatic $\langle a \rangle$ slip to $(10\bar{1}2)$ twinning, in some orientations.

The significant difference between the effective Schmid factor and the standard Schmid factor has implications for creep, quasi-static, and dynamic loading behavior.

For example, an α-β colony aligned for basal $\langle a \rangle$ slip can yield at 30.2% lower applied stress than a standard Schmid factor analysis would suggest. In some orientations prismatic $\langle a \rangle$ slip, which is the most common deformation mechanism, will begin at 6.8% lower applied stress than a standard Schmid factor analysis would suggest. The anisotropy of this behavior, illustrated in Figure 3.7, dictates that only some α-β colonies in a bulk material are affected, depending on their orientation relative to the loading direction. The resulting heterogeneity of the deformation behavior in bulk α-β alloys therefore requires careful consideration during component design and modeling.

The change in deformation mechanisms due to interaction stress also affects mechanical behavior. For the α-β variant tested in this study, we observe interaction stress driving an increase in basal $\langle a \rangle$ slip and $(10\bar{1}2)$ twinning at the cost of prismatic $\langle a \rangle$ slip. Twinning is observed to occur in tandem with stress induced martensite (SIM) as a creep deformation mechanism in certain α-β alloys, and hence increasing the propensity for twinning in certain orientations can affect creep performance [13, 57]; it is, however, noteworthy that twinning is very rarely observed in any Ti alloys containing more than 4 wt% Al. Activation of basal $\langle a \rangle$ slip near the interface may result in somewhat higher strength due to the higher CRSS for basal slip (as compared to prismatic slip) once the dislocation moves away from the interface.

Together, changes to the effective Schmid factor and the active deformation mechanism will result in variation of the measured CRSS for slip and twinning as a function of orientation. Such behavior is confirmed by comparison to experiment: compression testing of α-β Ti-8Al-1Mo-1V (wt%) samples with a wide range of

colony orientations (comparable to the range of orientations tested in this study) produced a wide range of measured CRSS values for basal, prismatic, and pyramidal slip [8]. Very detailed analysis for a much smaller range of orientations and samples also indicates that CRSS varies within a slip system [51, 52, 53]. As a direct comparison, calculated values of the apparent CRSS (as would be measured experimentally using the standard Schmid factor) for each activated deformation mode in Figure 3.12b and the experimental CRSS values measurements by Chan [8] are shown in Figure 3.13. Our calculations reproduce the experimentally measured range of CRSS for prismatic and basal $\langle a \rangle$ slip very closely. Further subtle behavior is also correctly reproduced, such as the larger range in CRSS values for prismatic $\langle a \rangle$ slip versus basal $\langle a \rangle$ slip. The experimentally measured magnitude of the change to CRSS is highly dependent on the loading orientation and orientation of the slip system with respect to the α-β interface as our model predicts.

This study represents a complete analysis of the possible orientations for the particular α-β variant used here, however other variants exist. The $[1\bar{2}10]_\alpha$ direction is perfectly aligned with the $[1\bar{1}1]_\beta$ direction per the BOR, however the angle between $\langle 1\bar{2}10 \rangle_\alpha$ directions is 120° while the angles between $[1\bar{1}1]_\beta$ directions are 70.5° or 109.5° resulting in a necessary mismatch between the remaining slip directions in each phase. The perfectly aligned slip systems can be oriented differently with respect to the interface plane, producing a total of 12 possible variants. Further, while an approximate $(\bar{5}140)_\alpha||(\bar{3}34)_\beta$ interface plane is observed macroscopically, it is in fact comprised of many steps of lower index α and β planes [68, 51] where the step height and width can affect the exact macroscopic habit plane and the
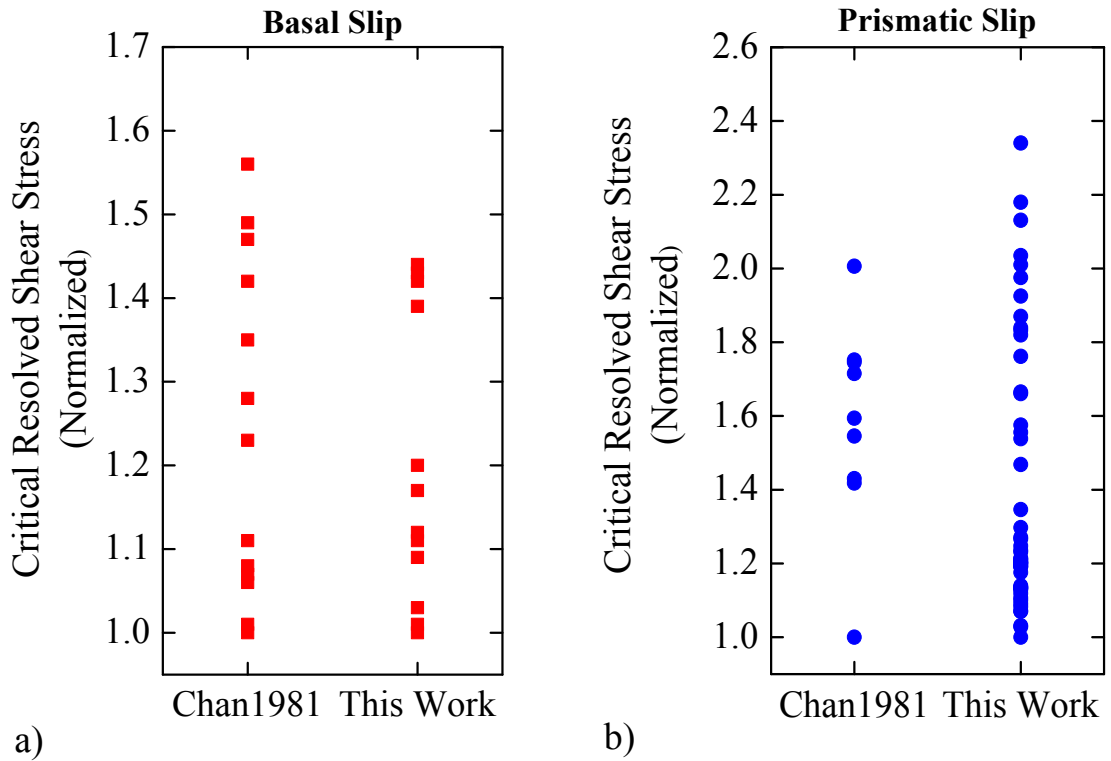
Figure 3.13: Comparison of experimental measurement from Chan 1981 [8] and model results for the range of observed CRSS for a) basal and b) prismatic slip across many different loading and crystallographic orientations.

angles between certain slip directions and the α-β interface [42]. Nonetheless, the symmetry of each variant is similar and the habit plane is experimentally observed to exist close to $(\bar{5}140)_\alpha||(\bar{3}34)_\beta$ in many cases, thus the results demonstrated here are qualitatively (and likely quantitatively) similar to behavior of all α-β colonies.

Our analysis pertains to the activation of deformation mechanisms beginning at zero strain, extending through purely elastic loading, and continuing only until the very first stage of plastic deformation in the α-phase. Calculations by Chan [42] indicate that the primary α deformation mechanism for plastic strains above 0.05% in α-β Widmanstätten alloys is determined by which mechanism most easily shears the β platelets, matching experimental observations [51, 52, 53]. Our analysis provides insight into the deformation mechanisms dominating only for the onset of plastic deformation in the α-phase, which may transition to other modes as stress increases. The activation of new deformation mechanisms with increasing stress will certainly be affected by the slip and twinning activity studied here. Dislocations and twins in the vicinity of the interface will act as barriers to motion of slip and twinning on other systems, while the local stress fields due to these defects will also play a role. Further, activation of otherwise unexpected deformation mechanisms due to interaction stress are significant for engineered systems where very small plastic strains critically affect performance.

3.5 Conclusion

Microstructural heterogeneity in engineering alloys gives rise to observed mechanical performance via the complicated interactions between phases, grains, and deformation products. For the case of Widmanstätten α-β Ti alloys, the α-β interface affects behavior during elastic and plastic deformation due to the development of interaction stresses. In this study we apply a combination of FEM modeling and dislocation theory to quantify elastic and plastic interaction stresses and their effects on the onset of deformation, finding several interesting features:

1. Elastic interaction stress significantly modifies the effective Schmid factor near the α-β interface. This interaction stress, due to the elastic mismatch and anisotropy of the α and β-phases, resolves onto the available slip and twinning systems in the α-phase, increasing the effective Schmid factor by up to 30% and causing slip to occur at lower applied stress than would be expected from Schmid's Law. The elastic interaction stresses are strongly anisotropic and affect independent slip and twinning systems differently.

2. As the α-phase begins to deform plastically, the relative shear moduli of the α- and β-phases produce a repulsive force against dislocation motion in some orientations. This repulsive force significantly increases the CRSS for slip near the boundary for particular independent slip systems. Deformation twins are similarly affected, although the magnitude of the effect is smaller

3. Interaction stress affects the active deformation mechanism for some orientations. For the α-β variant and CRSS ratios studied here, basal $\langle a \rangle$ slip and $(10\bar{1}2)$ twinning are promoted at the expense of prismatic $\langle a \rangle$ slip.

4. Combined, the interaction stresses affect the observed CRSS for each independent slip and twinning system. Our model results produce a distribution of observed CRSS for the basal and prismatic system that matches experimental results. This quantifies, for the first time, the source of CRSS varation and provides a clear mechanistic description of anisotropic plastic response in α-β Ti alloys.

By quantifying the elastic and plastic interaction stresses during the onset of deformation in α-β Ti alloy, this study provides a mechanistic understanding of orientation dependence and anisotropy of plasticity observed in engineered systems. Such behavior can be beneficial or detrimental and the concepts described here enable engineers to better predict and optimize component performance across the many applications of dual-phase Ti alloys.

Chapter 4: A Modified Embedded Atom Method Potential for The Titanium-Oxygen System

Titanium and its oxides have broad technical relevance as structural, electronic, and functional materials. Titanium oxides, particularly TiO_2, are used in many industrial and commercial applications including pigments and as electronic materials [69]. Structural Ti alloys exhibit excellent strength, toughness, corrosion resistance, and high temperature stability and have thus been the subject of extensive metallurgical research for several decades [1]. The Ti-O system is unique from most metal-gaseous element combinations in several important ways. For example, a large number of phases exist – structural information is reported for at least 26 different Ti-O structures – and the solubility of O in hcp Ti is up to 33 atomic percent at room temperature [7]. The high solubility of O in metallic Ti presents unique opportunities for tailoring the mechanical behavior of Ti alloys; O is a known α-stabilizer that generally increases strength while reducing ductility in Ti [24]. Further, the presence of O interstitials may affect the deformation characteristics of Ti alloys by impeding the growth of twins. Prior experimental work combined with a crystallographic model suggests that O interstitial sites are not conserved during the shearing process associated with twin growth and the interstitials thus inter-

fere with twin growth in bcc β-Ti [14]. In addition, recent experimental evidence indicates that $\{10\bar{1}2\}$ twin growth rate in hcp α-Ti is decreased by the presence of O interstitials, with implications for room temperature creep and structural performance [15, 16, 17]. Very recent DFT calculations by Ghazisaeidi and Trinkle provide additional clarity on the relationship between O interstitials and twins in α-Ti, demonstrating that both attractive and repulsive O interstitial sites exist in the vicinity of a twin boundary and the calculated energy of these sites is sensitive to supercell size [33]. Creep and deformation in Ti alloys is of critical importance for numerous applications and while many experimental measurements and *ab-initio* calculations have been dedicated to studying the Ti-O system, a gap exists in our ability to probe behavior at length and time scales below those accessible experimentally and above those accessible using first-principles techniques. Simulations using classical potentials provide an opportunity to explore material behavior at atomic length scales, while the modest computational requirements allow simulation of millions of atoms for practically meaningful times. Here we present a new modified embedded atom method (MEAM) potential that can be used for atomistic calculations of the Ti-O system. The potential is fit to the lattice constants, cohesive energies, and elastic constants of rock salt TiO, α-TiO (monoclinic), and Ti_3O_2 (hexagonal), the relative site energies of the three most prevalent O interstitial sites in hcp Ti, and the diffusion barrier for one of the many diffusion pathways of O in hcp Ti. The performance of the new potential is demonstrated by calculating the properties of many Ti-O structures and comparing to experimental and *ab-initio* results.

4.1 Computational Methods

We employed two computational techniques: the MEAM for which a Ti-O inter-atomic potential is the objective of this study, and DFT in order to produce fitting targets and validation tests for the MEAM potential. In total, we calculated properties for 11 different Ti-O structures in order to conduct a robust survey of bond distances, angles, O concentrations, and other important characteristics. The relevant input and output files for the DFT and MEAM relaxation calculations for all of the structures reported here are available via the NIST Computational File Repository [70].

4.1.1 Density Functional Theory

We performed all DFT calculations in the Vienna Ab-initio Simulation Package (VASP) [71, 72, 73, 74], employing projector augmented wave (PAW) psuedopotentials [75, 76] and the Perdew-Burke-Ernzerhof generalized gradient approximation (GGA-PBE) [77]. The cut-off energy for all calculations was held at 520 eV. For relaxation calculations we used a stopping criterion of < 5 meV/Å force on each atom in the system after finding that smaller values as stopping criterion did not produce significantly different results. All DFT calculations began with relaxation using Methfessel-Paxton smearing of 0.2 eV. Further, calculations of elastic constants employed a final, single-point calculation using the fully relaxed coordinates and the tetrahedron method with Blöchl corrections. Table 4.1 summarizes the supercell characteristics and DFT calculation settings including the number of k-points for

Table 4.1: Summary of structures and DFT settings used to determine fitting targets in this study. The k-point characteristics are indicated as (G) for gamma-centered.

Structure Name	Lattice System	Ti Atoms	O Atoms	k-point Mesh
Rock Salt TiO	Cubic	4	4	17 x 17 x 17 (G)
α-TiO	Monoclinic	10	10	7 x 5 x 11 (G)
Ti_3O_2	Hexagonal	12	8	3 x 3 x 11 (G)
hcp-Diffusion	Hexagonal	96	1	2 x 2 x 2 (G)

each of the structures used during the fitting process, while additional details for each calculation are provided in the text.

Calculating the cohesive energy of a system using DFT is typically accomplished by subtracting the sum of the single-atom energies from the calculated total energy of the system, however this produces an error of approximately 0.4 eV/atom for both Ti and O. Some of our MEAM fitting targets are calculated using DFT and so the systematic cohesive energy error from the DFT calculations would yield a MEAM potential with a relatively poor match to experimentally measured cohesive energies. To avoid this, we calculate "corrected" single-atom energies for Ti and O, E_{cs}, as

$$E_{cs} = E_{DFT} - E_{Exp} \tag{4.1}$$

where E_{DFT} is the converged total energy per atom for pure hcp Ti or an O_2 molecule and E_{Exp} is the experimental cohesive or binding energy per atom of the same pure system. For Ti we use the reported experimental cohesive energy of

hcp Ti, 4.871 eV/atom [78], as E_{Exp}. For O we define E_{cs} as one-half the binding energy of an O_2 molecule and thus E_{Exp} is the experimental binding energy of O_2, 2.558 eV/atom [79], and E_{DFT} is the converged total energy of an O_2 molecule in the triplet state. Based on these calculations $E_{cs}^{O} = 2.372$ eV/atom and $E_{cs}^{Ti} = 3.020$ eV/atom. All DFT calculated cohesive energies reported here use the corrected single-atom energies E_{cs} for O and Ti which reduces the error when comparing to experiment and yields a MEAM potential with reasonable fit to experimental cohesive energy data. Such an approach is not unprecedented; for example, Mishin et al. found that corrected DFT cohesive energies can support an effective EAM potential for studying Cu [80]. Comparison of our DFT calculated cohesive energies with experimental values for the range of structures and stoichiometries reported here further indicates the effectiveness of this approach.

We calculate elastic constants using the implementation of the "stress-strain" method outlined by Shang [81] for cubic materials, and Ganeshan [82] and Wang [83] for hexagonal materials. This approach begins by defining a set of strains, ϵ_i, and calculating the crystal lattice vectors after deformation, $\hat{\mathbf{Q}}$, from the lattice vectors of the relaxed structure, $\mathbf{Q}$, by

$$\hat{\mathbf{Q}} = \mathbf{Q} \begin{pmatrix} 1 + \epsilon_1 & \epsilon_6/2 & \epsilon_5/2 \\ \epsilon_6/2 & 1 + \epsilon_2 & \epsilon_4/2 \\ \epsilon_5/2 & \epsilon_4/2 & 1 + \epsilon_3 \end{pmatrix} \tag{4.2}$$

A DFT calculation for each independent strain, ϵ_i, without cell size of shape relaxation produces a corresponding stress, σ_i. Finally, the elastic constants are

calculated using Hooke's Law as

$$\mathbf{c} = \epsilon^{-1}\sigma \tag{4.3}$$

Calculation of elastic constants is also achievable using an "energy-strain" method by

$$c_{ij} = \frac{1}{V}\left(\frac{\partial^2 U}{\partial\epsilon_i\partial\epsilon_j}\right) \tag{4.4}$$

where V is the volume of material, U is the total energy of the system, and ϵ_k is a component of strain. Though VASP includes automated routines for performing these calculations, we found that the elastic constants calculated using the energy-strain approach did not match experimental values and behaved erratically as a function of calculation settings. All of the elastic constants reported here are calculated using the stress-strain approach.

4.1.2 Modified Embedded Atom Method

The Modified Embedded Atom Method was first proposed by Baskes [84, 85, 86] as a variation of the Embedded Atom Method (EAM) where the electron charge density surrounding an atom includes angular dependence. MEAM was further expanded for use with hcp metals, however the technique considered only first nearest neighbors and was unable to correctly predict some properties such as stacking fault energy [87]. Here we employ second nearest neighbor (2NN) MEAM, a modification to MEAM with improved predictive capability that includes interactions with atoms in the second coordination shell. Many variations on the MEAM exist with subtle differences in their implementation. We have generally followed the technique as

described by Lee et al [88, 89]. The overall approach is described here, with the mathematical details of the MEAM implementation used in this study provided in Appendix C.

In the MEAM the total energy of a system is represented as the sum of energy across all atoms, i, by

$$E_{Tot} = \sum_i \left[F_i(\rho_i) + \Phi_i(R_{ij}) \right] \tag{4.5}$$

where ρ_i is the charge density at the location of an atom and R_{ij} is the distance between atoms i and j; the energy of each atom is due to an embedding energy that varies with charge density at an atom's position, $F_i(\rho_i)$, and an interatomic potential that varies with the distance between neighboring atoms, $\Phi_i(R_{ij})$. Hence in general the MEAM requires a description of charge density throughout the system, an embedding energy functional for each type of atom in the system, and an interatomic potential for each atom-pair type. The implementation of the MEAM used here also employs a screening function such that nearby atoms screen interactions with more distant neighbors. Both the embedding term and interatomic potential term in the MEAM operate by comparing the energy of an arbitrary structure to the energy of a reference structure; in other words, after establishing the properties of a reference structure, some of which are used as input parameters for the MEAM potential, the MEAM allows calculation of total energy for an arbitrary structure based on the change in charge densities and nearest neighbor distances as compared to the reference structure.

The screening function applied in this study is a simple geometric method that

takes as parameters a minimum screening distance, C_{min}, and a maximum screening distance, C_{max}, for each atom that screens an interaction between two other atoms [88]. For a two-element potential like Ti-O, C_{min} and C_{max} must be established for all of the possible combinations, such as an O atom screening the interaction between two Ti atoms, or (Ti-Ti-O) (here the order of the elements follows the convention from the LAMMPS MEAM potential input files). The total possible combinations are (Ti-O-Ti), (Ti-Ti-O), (Ti-O-O), and (O-O-Ti) thereby requiring 8 screening parameters for the Ti-O system.

We performed all of the MEAM calculations using LAMMPS [90] with elastic constants computed using a script that is included with LAMMPS. In this study we use a MEAM potential for Ti from Kim, Lee, and Baskes [91] and a MEAM potential for O from Baskes [92]. A multi-element system such as Ti-O requires an additional 12 parameters, described with considerable detail in Appendix C, which must be determined in order to define the interaction of the dissimilar elements. Several parameters are physical properties of the reference structure that can be measured or calculated: cohesive energy, E_c, nearest neighbor distance, r_e, and α, which is function of the bulk modulus, atomic volume, and cohesive energy. The remaining parameters are the charge density scaling factor, $\bar{\rho}_0$, and the 8 screening parameters, which must be fit to reproduce known characteristics of the system. The reference structures for the Ti-Ti and O-O potentials are simply chosen to be the best-known structures (hcp and dimer, respectively), however a suitable reference structure for the Ti-O system is less obvious. We use rock salt as the reference structure for Ti-O which is relatively simple and has been used successfully as the MEAM reference

structure for similar potentials such as Ti-N and Ti-C [93], Fe-N [94], and Fe-C [95]. In addition, property data for other, distinct structures are required for fitting $\bar{\rho}_0$ and the 8 screening parameters. We use experimentally measured and DFT calculated lattice parameters, elastic constants, and cohesive energies of Ti_3O_2, a hexagonal close packed structure, and α-TiO, a monoclinic structure, as additional fitting targets. Further, we fit the relative energies of the three most prevalent O interstitial sites in hcp Ti as well as a diffusion activation barrier for an O interstitial in hcp Ti.

4.2 Determining MEAM Parameters

Our fitting process utilized property targets from two categories. First, the characteristics of several Ti-O structures provided fitting targets for varying compositions and crystal structures; second, the characteristics of O interstitials in hcp Ti provided targets for O defects in a metallurgically important structure. Our fitting calculations employed a version of LAMMPS compiled as a Python library along with a Python script written specifically for this fitting process, available via the NIST Computational Data Repository [70]. This script takes as input the desired test values for each MEAM parameter and produces a list of all possible combinations across the parameters. LAMMPS calculations of the target structures are performed for each parameter combination, the simulated characteristics are recorded, and the parameters producing the best fit are identified. Each screening parameter can have a value within a range of approximately 2 (e.g. between 0 and 2, or be-

tween 1 and 3) and with a resolution of approximately 0.02 (e.g. changing a value from 1.22 to 1.24 can have a meaningful impact on the calculated properties), while the charge density scaling parameter $\bar{\rho}_0$ can have a range of approximately 20 with a resolution of approximately 0.25. Running an exhaustive search across all of the possible combinations of parameter values would therefore require approximately 10^{17} LAMMPS calculations, which is not feasible. To avoid this, we performed the fitting process beginning with coarse resolution for each parameter, followed by local searches with increasingly fine resolution near the most promising parameter sets. We repeated this process using different starting parameters and search resolutions until the search identified parameters similar to those reported here. Following the brute force search, reaching the final parameter set required some manual fitting in the region near the final result. While this type of brute force searching process is not mathematically efficient, the thermodynamic and structural characteristics of the Ti-O structures studied here are not smooth functions of the input parameters; we explored the use of Nelder-Mead and Powell minimization methods, however these approaches tended to finish in local minima or produce erroneous parameter sets. Table 4.2 shows the best-performing Ti-O MEAM parameter set.

While a rock salt structure for TiO exists as γ-TiO, this structure includes somewhat complicated vacancy ordering and experimental values of lattice parameters vary across a wide range. Hence instead of γ-TiO, we use a perfect rock salt structure with no vacancies and supercell characteristics described in table 4.1. Convergence of elastic constants using the stress-strain method described above was relatively expensive, requiring a 17 x 17 x 17 gamma-centered k-point mesh that

86

Table 4.2: MEAM parameters for the Ti-O system

	Ti-O
E_c (eV/atom)	6.313
r_e (nm)	2.144
α	5.050
$\bar{\rho}_0$ O	2.20
C_{min}(Ti-Ti-O)(Å)	0.35
C_{max}(Ti-Ti-O)(Å)	1.27
C_{min}(Ti-O-Ti)(Å)	0.30
C_{max}(Ti-O-Ti)(Å)	2.80
C_{min}(Ti-O-O)(Å)	1.64
C_{max}(Ti-O-O)(Å)	3.14
C_{min}(O-O-Ti)(Å)	1.73
C_{max}(O-O-Ti)(Å)	2.85

we used for all subsequent rock salt calculations. The elastic constants of a cubic structure such as rock salt can be calculated using two-independent strains, ϵ_1 and ϵ_4, however several strain levels are required to demonstrate convergence with respect to strain. Rock salt TiO elastic constants reported here are averaged from calculations with ϵ_i equal to $\pm 1\%$, $\pm 0.7\%$, $\pm 0.5\%$, and $\pm 0.3\%$. In addition to our own calculations, the elastic constants of rock salt TiO have been the subject of several theoretical studies, producing the range of values shows in table 4.3. The elastic constants of the rock salt reference structure serve two purposes in the fitting process: as fitting targets themselves, and as input to calculating the value of the MEAM parameter α as described in the Appendix C. Included in table 4.3 are the bulk modulii, B, calculated using the standard definition $B = (c_{11} + 2c_{12})/3$, and the resulting values for α determined using our DFT calculated value of E_c; we allowed the value of α to vary between 4.500 and 5.170 during the fitting process based on the range in table 4.3. The elastic constants of rock salt TiO predicted using the MEAM potential are also shown, along with the resulting values for the bulk modulus and α; the value of α calculated from the simulated elastic constants is nearly identical to the input value of α in the MEAM potential (5.050), demonstrating self-consistency.

Robust experimental data is available for the crystal structures and thermodynamic properties of α-TiO and Ti_3O_2. A study by Watanabe using a combination of x-ray diffraction and transmission electron microscopy established that the low-temperature structure of α-TiO is monoclinic with space group $A2/m$ (no.12) and ordered vacancies on every 6th lattice site for both O and Ti [101]. Similarly, Ti_3O_2

Table 4.3: Calculated values of elastic constants for rock salt TiO using GGA-PBE, Ceperley-Alder local density dpproximation (LDA-CA), local density dpproximation with full-potential linear muffin tin orbitals (LDA-FPLMTO), the tight binding potential method (TBPM), and the MEAM potential from this study. Bulk modulus, B, and MEAM parameter α are calculated from the elastic constants.

Calculation Technique	c_{11}(GPa)	c_{12}(GPa)	c_{44}(GPa)	B (GPa)	α
GGA-PBE (this study)	503	84	18	223.7	4.542
GGA-PBE [96]	517	71	36	219.7	4.501
GGA-PBE [97]	-	-	-	221.8	4.524
LDA-CA [98]	612	129	123	290.0	5.172
LDA-FPLMTO [99]	693	73	130	279.7	5.079
TBPM [100]	650	72	145	264.7	4.940
MEAM (this study)	619	127	72	291.0	5.053

is known to be hcp with an ordered sub-lattice of interstitial O atoms and vacancies [102]. Thermodynamic properties such as the room-temperature enthalpy of formation, ΔH_f, for α-TiO and Ti_3O_2 are also reported [79, 103]. DFT calculations of the lattice parameters and cohesive energies of both structures using the supercell characteristics in table 4.1 established fitting targets and verified that these complicated structures were correctly captured in our structure-input files (which were similar for both MEAM and DFT) while also confirming the reported properties. Though experimental measurements are not available, we have also calculated the elastic constants c_{11}, c_{33}, and c_{44} for α-TiO and Ti_3O_2 for use as fitting targets. The experimental (where available), DFT calculated, and MEAM calculated properties of rock salt TiO, α-TiO, and Ti_3O_2 are provided in table 4.4. The quality of the fit is particularly good for the lattice parameters and cohesive energies of the three structures, with all of the MEAM results within 3.5% of experimental results. The MEAM results for elastic constants also fit well to DFT results with MEAM always reproducing the correct order of the elastic constants and yielding reasonable error considering the challenge of producing highly accurate elastic constants either experimentally or, as suggested in table 4.3, computationally.

In addition to the properties of the Ti-O structures described above, we employed the relative energies and a diffusion barrier for O interstitials in hcp Ti as fitting targets for the MEAM potential. We have closely followed earlier DFT calculations by Wu and Trinkle [104] using the "hcp-Diffusion" structure in table 4.1, reproducing their DFT calculations of site energy for the octahedral, hexahedral, and crowdion interstitial positions as well as the diffusion energy barriers between

Table 4.4: Experimental, DFT, and MEAM lattice parameters, elastic constants, and cohesive energies for the three Ti-O structures used for fitting in this study. DFT calculations of E_c use the corrected single atom energies described in equation 4.1.

	Experiment	DFT (this study)	MEAM (this study)
Rock Salt TiO			
a (Å)	-	4.288	4.288
E_c (eV/atom)	-	6.016	6.313
α-TiO			
a (Å)	5.855 [101]	5.854	6.060
b (Å)	9.340 [101]	8.910	9.098
c (Å)	4.142 [101]	4.171	4.033
γ	107.53° [101]	107.38°	105.91°
E_c (eV/atom)	6.511 [79]	6.248	6.511
c_{11} (MPa)	-	304	399
c_{33} (MPa)	-	427	450
c_{44} (MPa)	-	96	58
Ti$_3$O$_2$			
a (Å)	4.992 [102]	4.820	4.837
c (Å)	2.879 [102]	2.935	2.969
E_c (eV/atom)	6.196 [103]	6.037	6.230
c_{11} (MPa)	-	277	265
c_{33} (MPa)	-	357	289
c_{44} (MPa)	-	112	132

the sites. Climbing imagine nudged elastic band (NEB) calculations with five intermediate images and cell size/shape fixed to the relaxed hcp Ti structure with an octahedral O interstitial yield diffusion energy barriers for both DFT and MEAM [105, 106, 107]. For consistency with other calculations in this study we use a cutoff of 520 eV and PAW pseudopotentials; while Wu and Trinkle [104] used a lower cutoff energy, ultrasoft Vanderbilt pseudopotentials, and a single intermediate image for NEB calculations, our DFT results are nonetheless quite similar. After several iterations through the fitting process failed to produce MEAM parameters with reasonable diffusion energy barriers we opted to include the energy barrier of the octahedral site $\rightarrow$ octahedral site diffusion path as a fitting target. We note that only the peak energy of the diffusion barrier was included as a target and not the energy of the other NEB images. Including this energy barrier as a fitting target had the most significant effect on the value of the α parameter where higher values of α generally produced higher octahedral site $\rightarrow$ octahedral site diffusion energy barriers. Table 4.5 summarizes the DFT and MEAM calculated interstitial site energies relative to the octahedral site energy and the the octahedral site $\rightarrow$ octahedral site diffusion energy barrier. The MEAM potential is able to fit stable hexahedral and crowdion O interstitials with minimal error relative to DFT, indicating effectiveness for studying interstitials experiencing a variety of Ti-O bond distances and angles. Further, the comparison of the DFT and MEAM results for the octahedral site $\rightarrow$ octahedral site diffusion path demonstrates that the MEAM potential is capable of reproducing diffusion energy barriers with reasonable accuracy.

Table 4.5: Fitting results for the energy per O interstitial in hcp Ti relative to the octahderal interstitial energy; also included is the energy barrier for O diffusion between two octahedral sites (oct) in hcp Ti.

	DFT [104]	DFT (this study)	MEAM (this study)
Octahedral (eV)	0.00	0.00	0.00
Hexahedral (eV)	1.19	1.22	1.14
Crowdion (eV)	1.88	1.85	1.97
oct $\rightarrow$ oct (eV)	3.25	3.30	2.94

4.3 Validation and Transferability of the MEAM Potential

In order to test the effectiveness of the new MEAM potential we compare MEAM calculated results to DFT calculated results for a variety of structures and characteristics that were not included in the fitting process. Overall, we validated our MEAM potential by testing effectiveness in four areas: (1) diffusion energy barriers for O in hcp Ti, (2) accuracy of lattice parameters and cohesive energies of Ti-O structures and common oxides of Ti not included in the fitting process, (3) change in hcp Ti lattice parameters and elastic constants as a function of O concentration, and (4) change in cohesive energy with respect to hydrostatic strain for assorted Ti-O structures.

Again following earlier DFT calculations by Wu and Trinkle [104] using the "hcp-Diffusion" structure in table 4.1, we calculated the six diffusion energy barriers

not included as fitting targets between the octahedral, hexahedral, and crowdion interstitial sites. The results of these calculations shown in table 4.6 demonstrate that the MEAM potential is effective for predicting transition state energy in this system; the MEAM predicts energy barriers that are uniformly and modestly lower than the DFT predicted values, while the order of the MEAM barriers matches DFT. The largest error between the DFT and MEAM predicted diffusion energy barriers is for the two paths leaving from the crowdion site, however the MEAM also slightly overpredicts the crowdion site energy and hence the total energy required for diffusion of an atom to a crowdion site is still comparable to the DFT results. The MEAM is not able to comprehend significant charge transfer and so we performed Bader charge analysis for the O interstitials in the three stable interstitial sites and at the peak of each energy barrier using transition state tools available from the University of Texas [108, 109]. The Bader charge on the O interstitial varies only slightly between -1.4403 and -1.2753 across all of the base and peak positions for the diffusion barriers; significant charge redistribution, such as might negatively affect predictive capability of the MEAM potential, is not present.

DFT calculations using the settings described in table 4.7 along with experimental measurements of lattice parameters and cohesive energies of common Ti-O structures produced values for comparison with MEAM calculated characteristics. The "hcp" and body centered tetragonal ("bct") structures each include 4 at% O as octahedral interstitials; the hcp structure was not directly included in the fitting process as the formation energy of a single octahedral interstitial was not fit (only the relative energies of octahedral, hexahedral, and crowdion interstitials were in-

94

Table 4.6: Calculated diffusion energy barriers for various O diffusion pathways between octahedral (oct), hexahedral (hex), and crowdion (cr) sites in hcp Ti.

	DFT [104]	DFT (this study)	MEAM (this study)
oct $\to$ hex (eV)	2.04	2.05	1.98
hex $\to$ oct (eV)	0.85	0.83	0.84
oct $\to$ cr (eV)	2.16	2.15	2.04
cr $\to$ oct (eV)	0.28	0.30	0.07
hex $\to$ cr (eV)	0.94	0.91	0.85
cr $\to$ hex (eV)	0.24	0.28	0.02

cluded in fitting). The bct structure is the product of relaxing a body centered cubic (bcc) structure with a single octahedral interstitial; the relaxed structure yielded a bct cell in both DFT and MEAM calculations hence we report two independent lattice constants. Overall the MEAM, experimental, and DFT predicted values in table 4.8 compare favorably. The most significant errors between the MEAM potential results and DFT or experimental results are for the c-lattice constant of Ti_2O_3 and the cohesive energy of Rutile TiO_2; the stoichiometry of these compounds includes O concentrations well beyond the range included in the fitting procedure and hence larger error is expected. Notably, the MEAM potential reproduces the correct structures and qualitatively correct characteristics even in the case of these O rich chemistries.

Our DFT calculations of lattice parameters and elastic constants as a func-

Table 4.7: Summary of structures and DFT settings used to verify MEAM potential performance in this study; the characteristics of these structures were not included in the fitting process. The k-point meshes are indicated as (M) for Monkhorst-Pack and (G) for gamma-centered.

Structure Name	Lattice System	Ti Atoms	O Atoms	k-point Mesh
hcp-Elastic	Hexagonal	64	$0 - 4$	8 x 8 x 8 (G)
hcp	Hexagonal	24	1	3 x 5 x 3 (G)
bct	Tetragonal	24	1	3 x 5 x 5 (G)
TiO-CsCl	Cubic	1	1	15 x 15 x 15 (M)
TiO-ZincBlend	Cubic	4	4	11 x 11 x 11 (M)
Ti_2O_3	Rhombohedral	12	18	6 x 6 x 4 (M)
Rutile TiO_2	Cubic	2	4	8 x 8 x 8 (G)

Table 4.8: Experimental, DFT, and MEAM lattice parameters and cohesive energies for multiple structures not included in the fitting process.

	Experiment	DFT (this study)	MEAM (this study)
hcp			
a (Å)	2.954 [110]	2.944	2.956
c (Å)	4.699 [110]	4.672	4.708
E_c (eV/atom)	5.018 [111]	5.002	4.965
bct			
a (Å)	-	2.910	3.170
c (Å)	-	4.128	3.521
E_c (eV/atom)	-	4.951	4.927
TiO-CsCl			
a (Å)	-	2.651	2.608
E_c (eV/atom)	-	5.705	5.940
TiO-Zinc Blende			
a (Å)	-	4.645	4.614
E_c (eV/atom)	-	5.897	5.856
Ti$_2$O$_3$			
a (Å)	5.157 [112]	5.112	5.354
c (Å)	13.610 [112]	14.021	11.374
E_c (eV/atom)	6.618 [79]	6.387	6.899
Rutile TiO$_2$			
a (Å)	4.594 [113]	4.652	4.775
c (Å)	2.959 [113]	2.969	2.882
E_c (eV/atom)	6.576 [79]	6.349	6.100

tion of O concentration in hcp Ti used the "hcp-Elastic" structure described in table 4.7, with an example of the supercell containing four O interstitials shown in figure 4.1(a). We performed calculations using between zero and four O interstitials in the octahedral sites shown in red, producing supercells with 0 at% O, 1.54 at% O, 3.03 at% O, 4.48 at% O, and 5.88 at% O. Using a supercell with fixed size and increasing O content allows us to compare lattice parameters and energies as a function of O concentration calculated with identical supercell volume and k-point mesh, as opposed to using a single centered O interstitial and increasing the size of the supercell (and number of Ti atoms) and k-point mesh. Elastic constants were again calculated using the stress-strain approach with six independent strains, ϵ_i, and three strain levels of $\pm2\%$, $\pm1\%$, and $\pm0.5\%$. The MEAM calculated, DFT calculated, and experimental a-lattice parameter, c-lattice parameter, and cohesive energy as a function of O concentration are shown in Figures 4.1(b)–(d). The DFT and MEAM calculations correctly reproduce the experimentally measured increase in lattice parameter [110] as a function of O concentration along with a decrease in cohesive energy per atom [111]. While the MEAM calculations slightly overpredict the increase of the a- and c-lattice parameters with increasing O, the greatest error between MEAM and experimental values is less than 0.3%. The five independent elastic constants as a function of O concentration are shown in figure 4.2 along with the experimental values for pure Ti at room temperature and at 4 K [35]. The MEAM potential reproduces DFT predicted trends for the on-diagonal elastic constants, though it underestimates the increase in c_{33} with increasing O concentration. The MEAM calculated values for the off-diagonal elastic constants do not match the

DFT results with high accuracy, including an error in the trend of c_{13}, however the greatest error is still less than 13%. Unlike individual elastic constants, experimental measurements of Young's Modulus in hcp Ti as a function of O concentration are reported [24]; we calculate the Young's Modulus as a function of O concentration using the DFT and MEAM predicted elastic constants and the Voight model for Young's Modulus in polycrystalline materials

$$E_V = \frac{(A - B - 3\Gamma)(A + 2B)}{(2A + 3B + \Gamma)} \tag{4.6}$$

where $3A = c_{11} + c_{22} + c_{33}$, $3B = c_{23} + c_{13} + c_{12}$, and $3\Gamma = c_{44} + c_{55} + c_{66}$ [49]. Our predictions compare favorably with the experimental results as shown in figure 4.3. A recent DFT study of the elastic constants of hcp Ti as a function of interstitial O concentration by Kwasniak et al. [114] confirms the qualitative trends observed here, though we note that their study employs variable supercell size and k-point mesh in order to change O concentration which can be problematic given the extreme sensitivity of elastic constant calculations to the accuracy of the calculated energy.
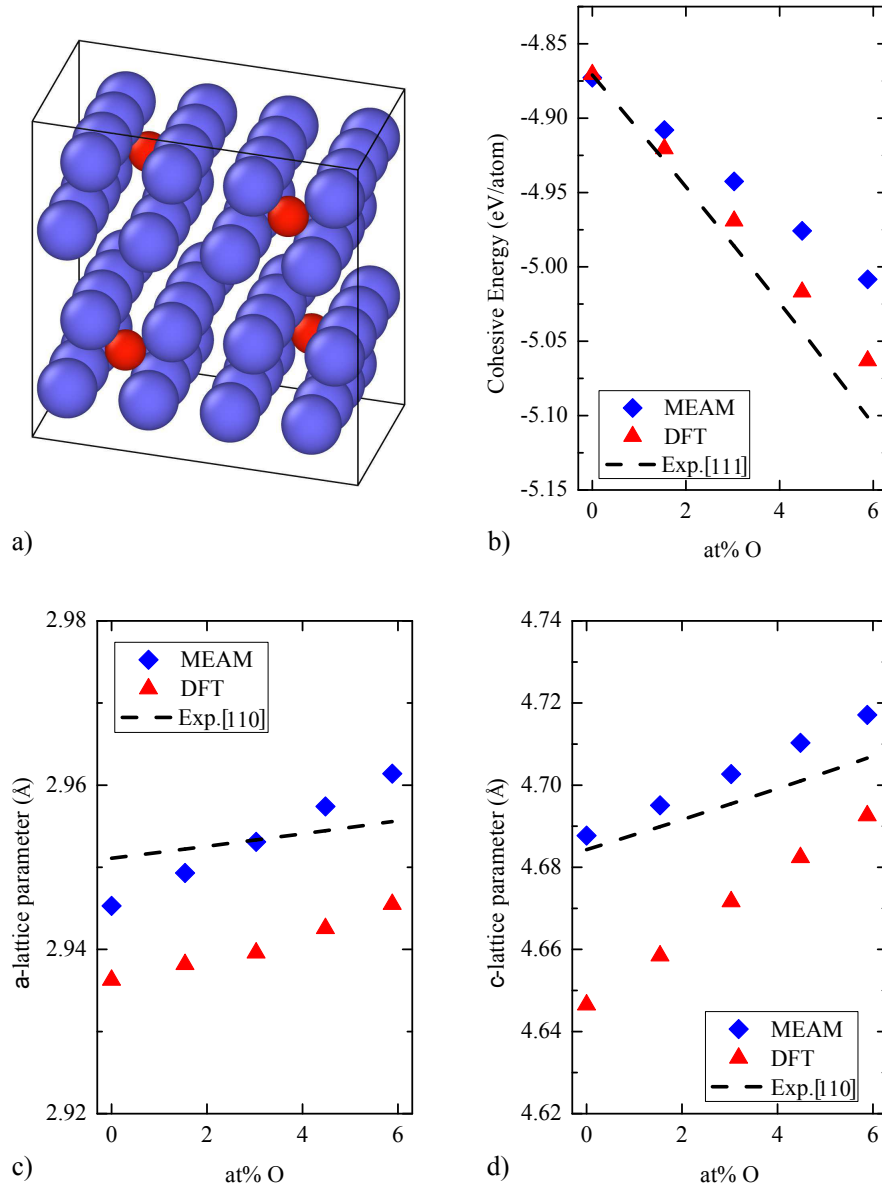
Figure 4.1: Validation testing of the MEAM potential by comparison to DFT and experimental (Exp) results for increasing octahedral interstitial concentration in hcp Ti. Both DFT and MEAM calculations used an identical supercell varying between 0 and 4 O interstitials, with an example in a) shown with Ti atoms in blue and four O interstitials in red. The MEAM results compare favorably to DFT and extrapolated experimental results for b) cohesive energy, c) *a*-lattice parameter, and d) *c*-lattice parameter.
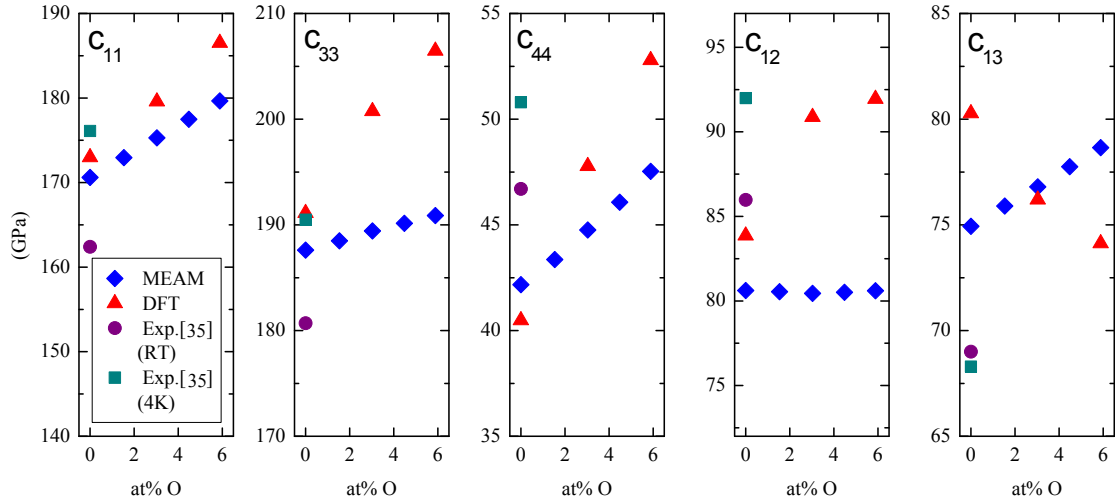
Figure 4.2: Elastic constants of hcp Ti with increasing concentrations of octahedral O interstitials. Experimental results are shown for pure Ti at room temperature (RT) and 4 Kelvin (4K). Results calculated using DFT and MEAM compare favorably for diagonal components. All elastic constants are reported in GPa.
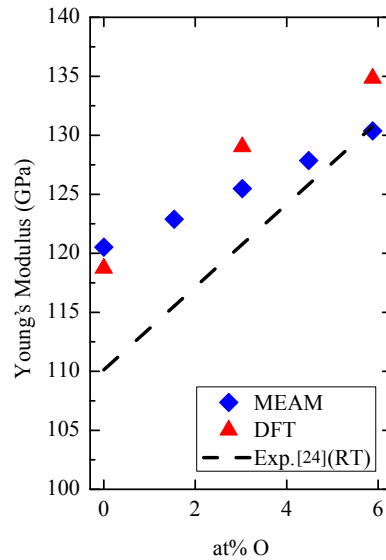
Figure 4.3: Young's Modulus versus O concentration calculated from simulated elastic constants using equation 4.6 and extrapolated from measured values.

In figure 4.4 we compare DFT and MEAM prediction of the change in cohesive energy with respect to hydrostatic strain in order to demonstrate that the MEAM potential correctly reproduces stiffness and stability for structures with a variety interatomic distances and angles. In addition to the rock salt TiO, α-TiO, and Ti_3O_2 structures used for fitting, we include the "CsCl", "hcp", and "bct" structures described in table 4.7. Both MEAM and DFT calculations begin with the fully-relaxed lattice parameters as the 0% strain condition, followed by relaxation of atomic positions at hydrostatic strains between -20% and 20%. Also shown in figure 4.4 are the experimental cohesive energies and unit cell volumes for the 0% strain condition of α-TiO, Ti_3O_2, and hcp Ti with 4 at% O. The offset between the DFT and MEAM calculated values for the four oxide systems in the lower, left-hand corner of figure 4.4 is due to the better accuracy of the MEAM potential in reproducing experimental results as compared to the DFT calculations. Both the MEAM potential and the DFT calculations produce very low error for cohesive energy and lattice parameters of the hcp structure while also capturing subtle behavior such as the overlap of the hcp and bct cohesive energies at high compressive strains. Overall, figure 4.4 demonstrates that the MEAM potential reproduces the DFT calculated energy curvature and stability of these structures when subjected to strain, while also yielding good accuracy when compared to experimental measurements.
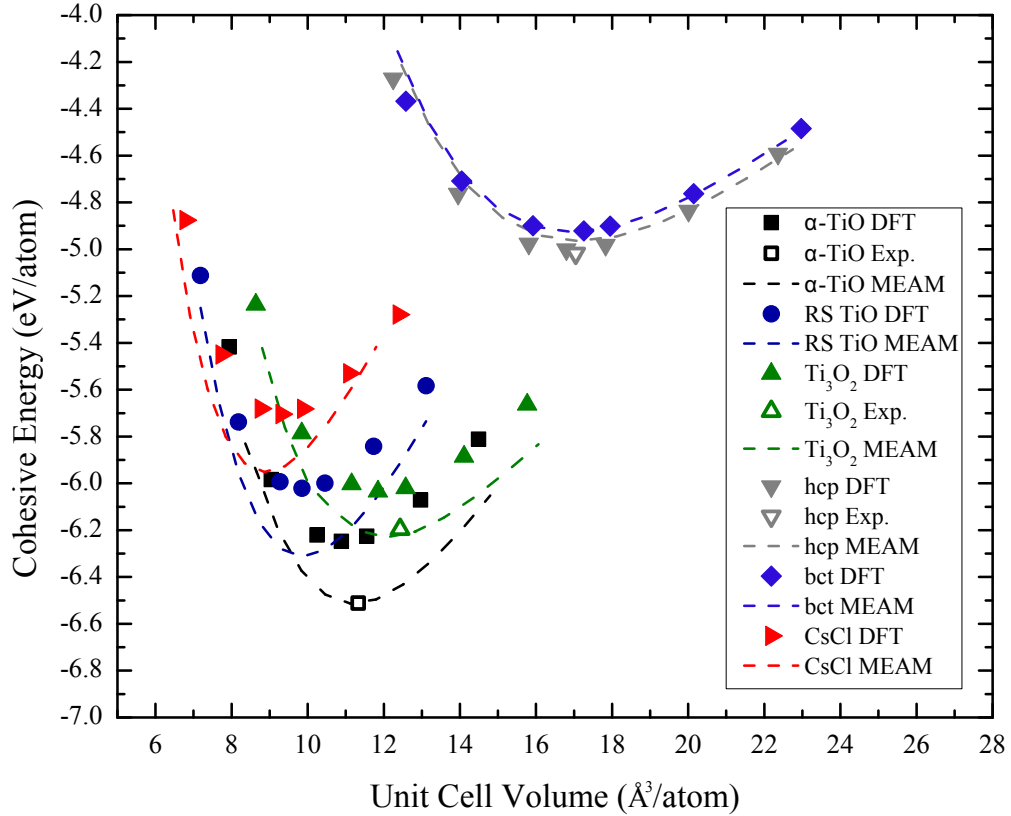
Figure 4.4: Cohesive energy per atom versus unit cell volume per atom for six Ti-O structures each subjected to hydrostatic strain between -20% and 20%

4.4 Conclusion

We have presented a new modified embedded atom method (MEAM) potential for the Ti-O system which is fit to DFT calculated lattice constants, cohesive energies, elastic constants, and a diffusion barrier for structures exhibiting a variety of bond distances, bond angles, and O concentrations. The potential is validated by successfully reproducing the diffusion barriers for O in hcp Ti, properties of hcp Ti as a function of increasing O concentration, the lattice parameters and cohesive

energies of many Ti-O structures, and the hydrostatic strain versus cohesive energy relationships for several structures. The new potential is effective for predicting structural and thermodynamic features of structures ranging from dissolved oxygen in a metallic titanium lattice to common oxides of titanium. The MEAM-predicted diffusion energy barriers for O in Ti are somewhat less than DFT predictions but correctly ordered with respect to the diffusion pathway. The lower computational cost of MEAM calculations when compared to DFT calculations enables simulation of the behavior of many thousands of atoms, allowing interrogation of large systems such as twins interacting with interstitials or interaction of multiple dislocations with interstitials. Further, the high space and time resolution of atomistic modeling can offer new insight when compared to experimental results for a wide range of characteristics.

Chapter 5: Interaction Between Oxygen Defects and Deformation Twins in α-Titanium

Oxygen (O) has up to 33 at% solubility in α-Ti [7] and is a common impurity and alloying element. Interstitial O is also believed to interact with deformation twins, and may result in time-dependent twinning by obstructing the shearing/shuffling process associated with twin growth [28]. Early work by Biget & Saada identified that the shuffle distance for interstitials impurities in Zr (an hcp metal with a similar structure to Ti) are larger than the shuffle distances for Zr atoms during $(10\bar{1}2)$ and $(11\bar{2}1)$ twinning, although the possibility for O-Zr interference during shuffling was not described [30]. More recent experimental measurements combined with a crystallographic model suggest that O interstitial sites interfere with the shuffle of Ti atoms during twin growth in body centered cubic (bcc) Ti, requiring O interstitial diffusion away from or across the twin to enable further twin growth [14]. In addition, a decrease in $(10\bar{1}2)$ twin growth rate during creep in α-Ti may be associated with the presence of O interstitials based on a similar crystallographic model [15, 16]. The width of $(10\bar{1}2)$ twins decreases with increasing strain rate during quasi-static loading, providing further evidence of time dependence of twin growth in α-Ti [17]. The measured activation energy for twin growth in α-Ti, calculated

using the diffusion coefficient for O diffusion in the bulk, is approximately 0.684 eV during creep loading [16]; the activation energy for O diffusion in bulk α-Ti was recently measured as 1.75 ± 0.52 eV using high purity samples and the nuclear resonance technique [115], while DFT calculations yield an activation barrier of 2.08 eV [104]. Historical measurements with reasonable results indicate activation energy for diffusion between 1.45 eV and 2.68 eV [116]. Should O interstitials interact with twin growth as crystallographic modeling suggests, the difference between the bulk diffusion activation barrier and the activation barrier for twin growth indicates that twin growth and O diffusion mechanisms interact in a complicated way. The length and time scales of these interactions make experimental measurement very difficult, while atomistic modeling provides an excellent tool set for gaining an improved, mechanistic understanding of the processes. Density functional theory (DFT) calculations by Ghazisaeidi and Trinkle demonstrate that a $(10\bar{1}2)$ twin boundary affects the formation energy of octahedral oxygen interstitials in the immediate vicinity of the twin [33], however the effect of the twin on formation energy of other sites and the activation barriers for diffusion between the sites is not known. Recent DFT calculations reveal that O diffuses readily along the core of a prismatic edge dislocation in α-Ti and that the presence of O increases Peirels stress and modifies dislocation core geometry [27], providing further indication of complicated interactions between Ti deformation mechanisms and O interstitials. In this study we interrogate the effect of $(10\bar{1}2)$ twin boundaries on the formation energies, activation barriers, and diffusion pathways for O. We report that the presence of a $(10\bar{1}2)$ twin boundary has a significant effect on the thermodynamics and kinetics

of nearby O interstitials.

5.1 Computational Techniques

Investigating material behavior often requires multiple computational techniques to properly address the range of relevant time and length scales. Directly simulating interactions of O defects with a crystallographically complicated planar defect such as a twin requires atomistic modeling, however many such techniques exist. In this study, we employ a combination of DFT and modified embedded atom method (MEAM) calculations to leverage the benefits and offset the disadvantages of each tool. DFT is an *ab-initio* technique that offers excellent predictive power but is limited to simulation of relatively few atoms for relatively brief periods. The MEAM is an empirical potential method that trades a loss of rigorous physical modeling for capability to simulate substantially larger systems for longer periods of time when compared to DFT. Our DFT calculations are performed in the Vienna Ab-initio Simulation Package (VASP) [71, 72, 73, 74], employing projector augmented wave (PAW) psuedopotentials [75, 76] and the Perdew-Burke-Ernzerhof generalized gradient approximation (GGA-PBE) [77]. The cut-off energy for all calculations was held at 520 eV. We apply Methfessel-Paxton smearing of 0.2 eV and use a $2 \times 1 \times 6$ Monkhorst-Pack k-point mesh. Relaxation calculations were stopped when the force on each atom in the system was < 5 meV/Å. Our MEAM calculations are performed in LAMMPS [90] using published MEAM potentials for Ti [91], O [92], and Ti-O [117], noting that the Ti-O potential was fit specifically to study the interaction

between O interstitials and twins in Ti alloys. Among several variations of the MEAM, we use the second nearest neighbor (2NN) technique as outlined by Lee et al. [88, 89], following the earlier work by Baskes [84, 85, 86, 87]. Activation barriers for diffusion are calculated using the climbing imagine nudged elastic band (CI-NEB) approach with three to seven intermediate images [105, 106, 107]. Creation of the supercells for these calculations, visualization of results, and production of several figures was accomplished using the Open Visualization Tool (OVITO) [118].

5.2   Structural Model

5.2.1 $(10\bar{1}2)$ Twin in Pure Ti

We produced several supercells to enable investigation of the effects of distance between twins and oxygen interstitials on the behavior of the system. Figure 5.1 shows our "short" and "tall" twin supercells, which vary in size along the y-direction, along with the coordinate system used in this study; two $(10\bar{1}2)$ twin boundaries are required in order to maintain periodicity in the y-direction. Cell depth in the z-direction (which corresponds to $[1\bar{2}10]$) varies in intervals of the lattice parameter of α-Ti, a, which is equal to 2.95 Å [119]. To create a supercell containing a $(10\bar{1}2)$ twin we first rotate the hcp titanium unit cell such that the $[1\bar{2}10]$ direction is aligned with the z-direction. One side of the twin is then rotated so that the normal to the $(10\bar{1}2)$ plane is aligned with the y-direction, while the second side of the twin is rotated so that the normal to the $(\bar{1}012)$ is aligned with the y-direction. Volumes of atoms rotated for each side of the twin are combined into a single supercell and

trimmed in the x- and z-directions for periodicity. Relaxation of the initial twin structure is accomplished in two steps: first, the cell is relaxed in the y-direction only while the atoms are allowed to relax completely, after which the cell and atoms are free to relax in all directions, although the cell is prevented from shear distortion.

We first compare the experimentally measured twin boundary structure [120] with the results of our DFT and MEAM calculations with $z = 2a$. Figure 5.2 compares the DFT, MEAM, and experimental structures, with the structure motif superimposed for clarity; the calculated $(10\bar{1}2)$ structures relax to a planar twin as found experimentally, while the angle between basal planes across the twin boundary, θ, is also correctly captured. The $(10\bar{1}2)$ twin energy is 0.301 J/m^2 calculated using DFT and 0.410 J/m^2 calculated using the MEAM. The relaxed structure and twin boundary energy is identical for the short and tall twin supercells and is not affected by changes to supercell depth in the x- or z-directions. While the MEAM overestimates the twin boundary energy by comparison to DFT, the formation energies of the many oxygen interstitials studied here are not significantly affected.

5.2.2   Octahedral O Interstitials Near a $(10\bar{1}2)$ Twin

Having obtained the correct $(10\bar{1}2)$ twin structure for pure α-Ti, we calculate the formation energy of octahedral O interstitials near the twin boundary following earlier work by Ghazisaeidi and Trinkle [33], employing our short supercell and their notation for the numbering of the octahedral sites. The five sites used to calculate interstitial formation energy are shown in Figure 5.3. Formation energy
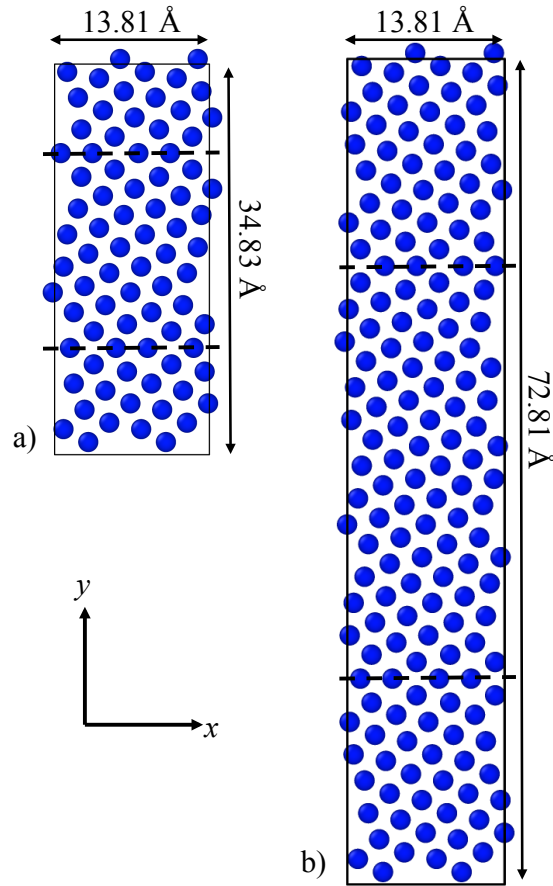
Figure 5.1: Front view of the a) "short" and 'b) 'tall" twin supercells along with the coordinate system used in this study. The twin boundaries are indicated with dashed lines. The supercells have variable depth along the z-direction (into the page), which corresponds to $[1\bar{2}10]$.
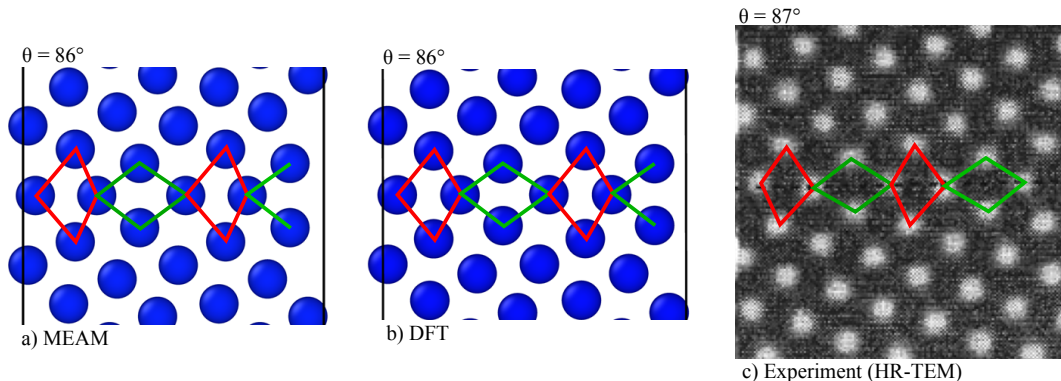
Figure 5.2: Relaxed $(10\bar{1}2)$ twin structure a) calculated using the MEAM, b) calculated using DFT, and c) measured experimentally using high-resolution transmission electron microscopy (HR-TEM) [120]. The angle between basal planes across the twin boundary, θ, is also reported.

of the interstitials near the twin is calculated relative to the energy of the system with an interstitial at site O0, where the cell size for calculation of all interstitials is fixed at the fully relaxed size with an interstitial at site O0. As shown in Table 5.1, despite a different supercell size and slightly different DFT calculation settings, our results are quite similar. The MEAM is also effective for calculating formation energy, with an error of less than 0.2 eV in all cases; while the formation energy of interstitial O2 is negative in the MEAM and positive in DFT, this difference is very small compared to the effect of the twin boundary on the energy of other sites and the diffusion activation barriers as discussed later.

A benefit of applying the MEAM is the capacity for large supercells at minimal computational cost. Hence while our DFT calculations are limited to the short twin with a depth of 5.90 Å, we can explore much larger systems using the MEAM.
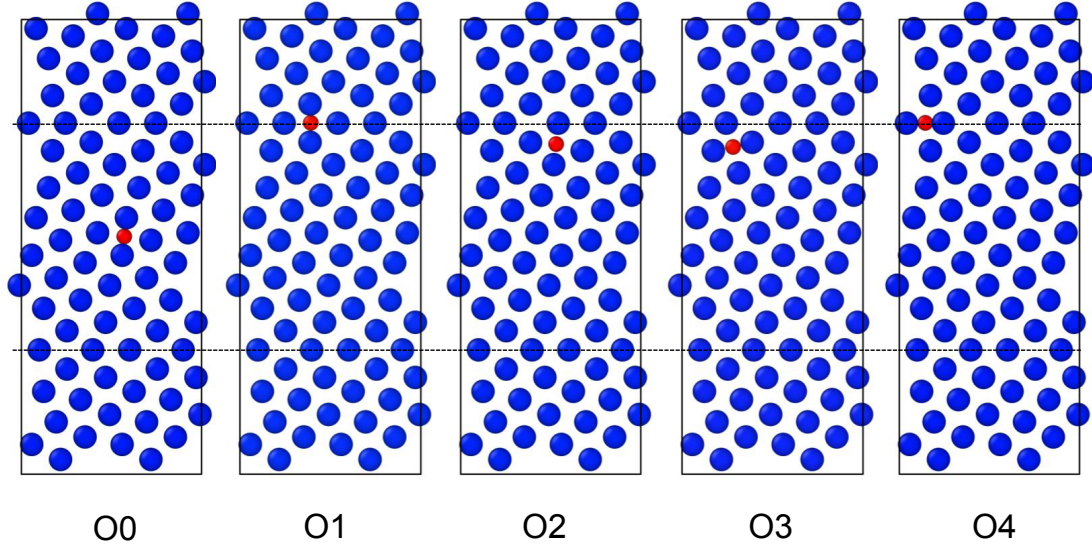
Figure 5.3: Octahedral interstitial sites O0 through O4, following Ghazisaeidi and Trinkle [33]. The depth of the supercell into the page is $2a$, approximately 5.90 Å, and the twin boundaries are indicated with dashed lines.

Table 5.1: Formation energy of octahedral interstitials 0 through 4 (O0 - O4, see Figure 5.3) calculated by DFT and MEAM using the short supercell with a z-dimension of 5.90 Å.

	DFT [33]	DFT (this study)	MEAM (this study)
O0 (eV)	0.0	0.0	0.0
O1 (eV)	-0.052	-0.082	-0.017
O2 (eV)	0.115	0.087	-0.118
O3 (eV)	0.193	0.177	0.077
O4 (eV)	-0.079	-0.109	-0.138

The formation energy of interstitials in positions 1-4 as well as the energy barriers for diffusion between the sites converge as cell size is increased in the x-, y-, and z- directions. Figure 5.4 demonstrates that the formation energy of the interstitial sites converges as thickness of the cell along the z-direction is increased to $6a$ (17.70 Å). Convergence with respect to the y-dimension of the cell is largely achieved using the short cell when considering the interstitial formation energies and activation barriers for diffusion at the twin boundary; however, the short cell limits the maximum possible distance from the twin boundary in the y-direction to about 8.7 Å, restricting our study of the effects of distance of the interstitial from the twin. Not shown are results for convergence with respect to supercell size in the x-direction, which was achieved at the size shown in Figure 5.1. Based on these results, we employ the tall twin structure with a depth in the z-direction of $6a$ (17.70 Å) for MEAM-only calculations along with the short twin structure with a depth in the z-direction of $2a$ (5.90 Å) for calculations utilizing both MEAM and DFT.

5.3 The Effects of a Twin Boundary on Interstitial Site Stability and Formation Energy

While the presence of a $(10\bar{1}2)$ twin boundary in Ti is known to affect the formation energy of octahedral interstitials in the immediate vicinity of the twin [33], the effects on the hexahedral and crowdion sites, as well as octahedral interstitials further from the twin, have not been previously explored in Ti or any other system. The distribution of O interstitial sites in the vicinity of a the twin is shown in Fig-
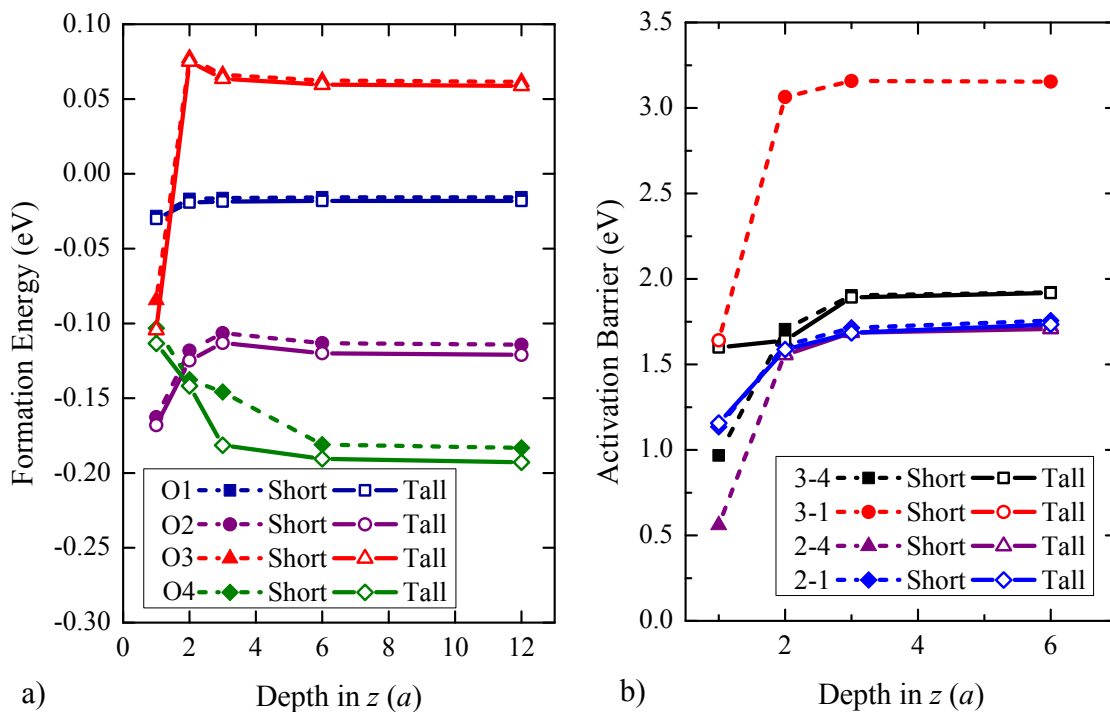
Figure 5.4: Convergence testing with respect to supercell size in the y- and z-directions (see Figure 5.1) for (a) interstitial formation energy and (b) diffusion activation barrier for octahedral sites 1 through 4

ure 5.5a) with an additional crowdion site located directly into the page behind each of the four octahedral sites. We refer to this distribution of sites as the "0th" layer (0L) from the twin; only unique interstitial sites are shown (unique with respect to both coordination and formation energy), and the remaining sites are obtained by translation and symmetry operations. As a first test, and for further validation of the MEAM potential, we calculate the formation energy of the octahedral, hexahedral, and crowdion interstitials in the 0th layer using both DFT and MEAM and the short supercell with a depth in the z-direction of $2a$ (5.90 Å). Fully relaxing the system yields the arrangement of sites in Figure 5.5b); the formation energies relative to the energy of a system with an interstitial in O0 are shown in Figure 5.6. The twin boundary has several important effects on the stability and formation energy of the defects. First, the hexahedral site nearest to the twin boundary, H1, and the crowdion site nearest to the twin boundary, C2, relax into stable tetrahedral interstitials, T1 and T2, directly at the twin boundary; both DFT and MEAM predict this behavior, however the MEAM potential produces slightly asymmetrical tetrahedral sites while DFT predicts perfect tetrahedral interstitials. Tetrahedral oxygen interstitials are not stable in bulk α-Ti and the $(10\bar{1}2)$ twin therefore introduces a new, previously unreported defect. Second, crowdion interstitials C7 and C8, directly behind octahedral sites O2 and O3, are not stable using DFT or the MEAM; the greater interatomic distances above and below the twin allow the system to relax by moving the twin boundary in response to the presence of these defects. Finally, while DFT predicts that all of the sites in Figure 5.5b) are stable, crowdion interstitials C3 and C4 are unstable when using the MEAM; this is
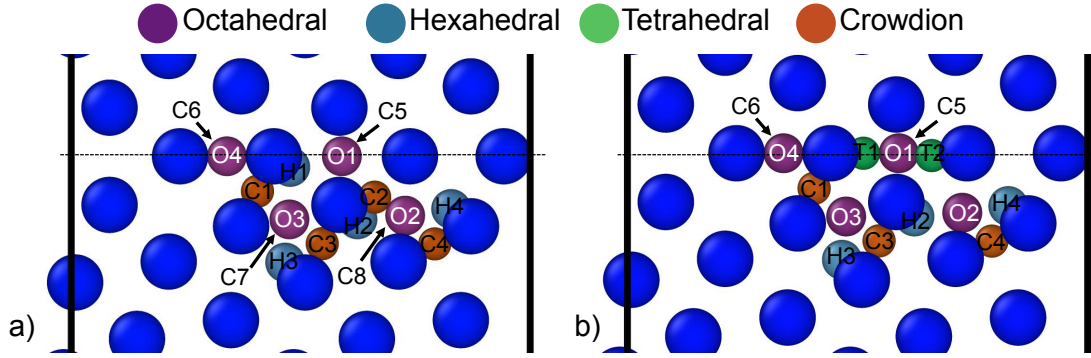
Figure 5.5: Unique interstitial sites in the 0th layer (0L) from the twin boundary (indicated by a dashed line) a)before and b)after relaxation; the Ti atoms are shown in their unrelaxed positions in both cases for clarity. Crowdion sites C5 - C8 are behind (into the page) octahderal sites O1 - O4, as indicated by arrows. After relaxation, hexahedral H1 and crowdion C2 relax to tetrahedral interstitials T1 and T2, respectively. The crowdion interstitials C7 and C8 are unstable.

likely due to the slight overprediction of crowdion interstitial energy and the slight underprediction of diffusion activation barriers for paths leaving the crowdion sites when using this MEAM potential [117], which causes the crowdion sites to be less stable. The energy of these sites is reported in Figure 5.6 using the peak position of the diffusion pathway through their location, which maintains the correct crowdion structure despite the instability.

The formation energies of oxygen interstitials continue to differ from the bulk values at greater distance from the $(10\bar{1}2)$ twin boundary. In order to study the effect of distance from the boundary on interstitial formation energy, we identify the interstitial sites matching those shown for the 0L layer in Figure 5.5 in subsequent layers. Figure 5.7 shows the position of these interstitials in the 0L layer
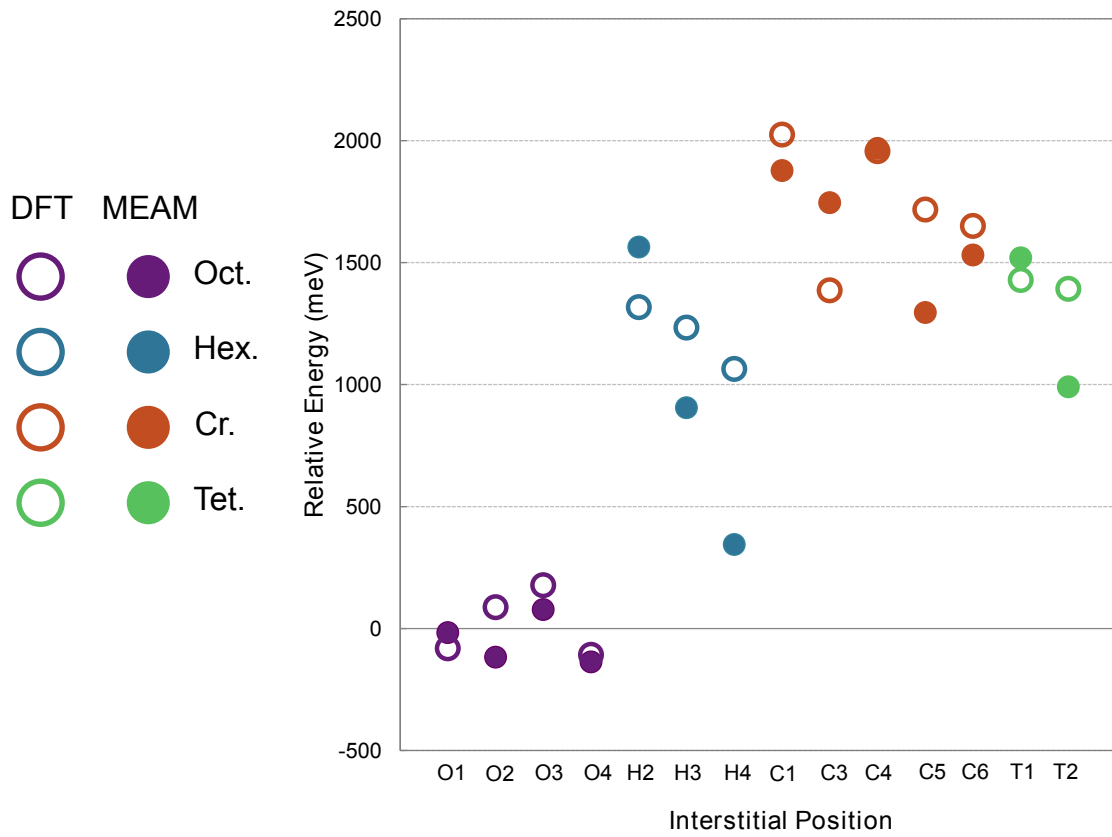
Figure 5.6: Formation energy of the octahedral, hexahedral, crowdion, and tetrahedral sites in the 0th layer from the twin. Position numbers are provided in Figure 5.5.

of the tall supercell as well as in the second (2L) and fourth (4L) layers from the twin. Equivalent sites also exist in the first (1L) and third (3L) layers from the twin and are included in our calculations; however the 1L and 3L sites are not shown in Figure 5.7 for clarity. The change in formation energy of the octahedral, hexahedral, and crowdion interstitials as a function of distance from the twin is shown in Figure 5.8a)–c) as calculated using the MEAM; the tetrahedral interstitial energy for the 0L interstitials is included in the hexagonal and crowdion plots to reflect the position that the tetrahedral defect replaces in diffusion paths near the twin. The formation energy of the octahedral defects varies between +0.05 eV and −0.19 eV at the twin boundary and returns to bulk-like behavior in the 3L layer at a distance of about 12 Å from the twin boundary.

The hexahedral defects behave similarly to the octahedral defects, although the formation energies vary across a wider range from +0.30 eV to −0.57 eV. The tetrahedral site that replaces the hexahedral site nearest to the twin has a formation energy 0.35 eV lower than the bulk value, although it is not the lowest energy hexahedral site in 0L. As with the octahedral interstitials, the hexahedral defects recover bulk like formation energy in the 3L layer.

The crowdion interstitials behave somewhat differently, with all sites having lower formation energy near the twin boundary than in the bulk and formation energy for several sites still lower than the bulk value in the 4L layer. The lowest energy crowdion site in the 0L layer has a formation energy 0.48 eV lower than the bulk value, while the tetrahedral interstitial that replaces a crowdion site nearest to the twin exhibits 0.79 eV lower formation energy.

Such changes in formation energy are quite large, particularly when considering that occupancy at thermal equilibrium is proportional to $\exp(-\Delta E_f/k_B T)$ where ΔE_f is the difference in formation energy of a defect relative to the average energy of the system, k_B is the Boltzmann constant, and T is the temperature. However, it is important to note that the greatest change in formation energy near the twin boundary occurs with the hexahedral and crowdion sites, which are still at least 0.5 eV above the bulk octahedral interstitial formation energy. The formation energy of the octahedral sites near the twin is not as dramatically affected. We therefore expect that the concentration of O near the twin will be comparable to the concentration in the bulk, with most interstitials occupying octahedral sites; however, a greater proportion of O near the twin will occupy hexahedral, crowdion, and tetrahedral sites owing to the lower formation energy of these interstitials.

5.4 The Effects of a Twin Boundary on Activation Barriers for Diffusion

Along with formation energy, the presence of a nearby $(10\bar{1}2)$ twin boundary also affects the activation barriers for diffusion of O through the lattice. Diffusion of O in bulk α-Ti is known to occur by movement between the octahedral, hexahedral, and crowdion interstitial sites with many possible paths contributing to diffusion [104]. There are four independent diffusion paths in the bulk: octahedral $\rightarrow$ octahedral, octahedral $\rightarrow$ hexahedral, octahedral $\rightarrow$ crowdion, and hexahedral $\rightarrow$ crowdion, and the MEAM potential used here is effective for reproducing the activation barriers for
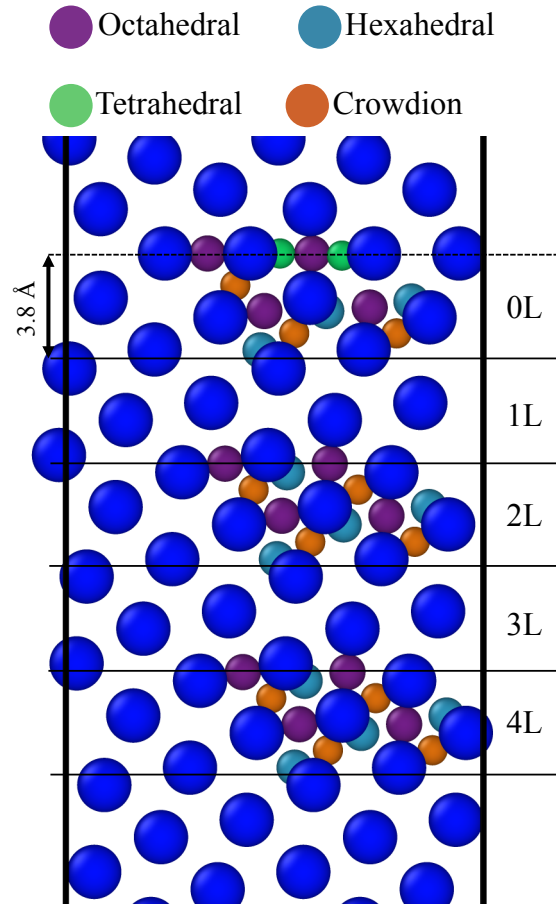
Figure 5.7: Location of O interstitial sites at increasing distance from a $(10\bar{1}2)$ twin, indicated by a dashed line. The layers are labeled as the 0th layer from the twin (0L) through the fourth layer from the twin (4L). Equivalent sites exist in 1L and 3L and have been included in the calculations described here, however they are not shown in the figure for clarity.
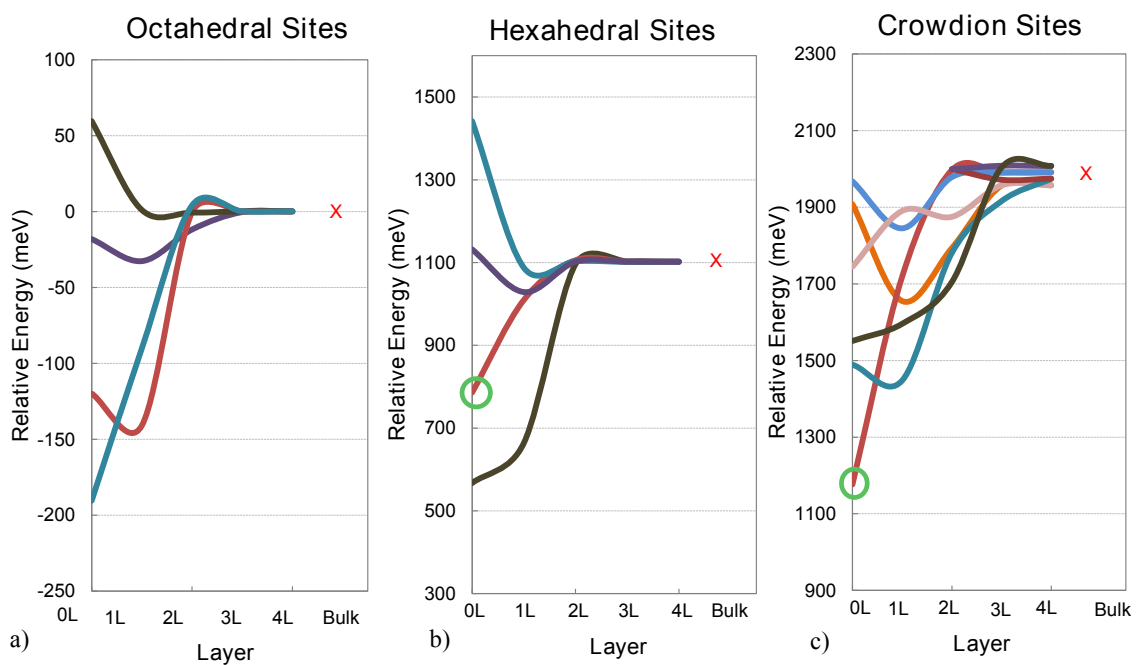
Figure 5.8: Formation energy of a) octahedral, b) hexahedral, and c) crowdion sites as a function of distance from the twin boundary, with distance reported in terms of layer from the twin (see Figure 5.5). Each line corresponds to a unique interstitial which repeats in each layer; for example, the O4 octahedral is represented by a single line in a). The hexahedral and crowdion interstitials which relax into a tetrahedral position in the 0L layer are indicated with a green circle. The bulk formation energy for each defect relative to the octahedral interstitial is shown with a red "X".

these paths [117]. The formation energy results in Figures 5.6 and 5.8 demonstrate that there are many more independent diffusion paths near the twin due to the increased number of unique interstitial positions. In order to conduct a complete assessment, we have calculated the diffusion activation barrier for every possible unique jump in layers 0L and 4L. Figure 5.9 provides the diffusion activation energy results for each unique path.

The 4L results are very bulk-like and generally collapse onto a single path matching the MEAM predictions of the bulk path. Conversely, the 0L results demonstrate very different behavior near the twin boundary when compared to the bulk. The nearby $(10\bar{1}2)$ twin boundary has a dramatic effect on some of the octahedral $\rightarrow$ octahedral jumps in 0L, reducing the peak energy by more than 1 eV. While direct octahedral $\rightarrow$ octahedral diffusion does not contribute significantly during bulk diffusion [104], a nearby twin reduces the peak energy of these paths making them comparable to octahedral $\rightarrow$ hexahedral and octahedral $\rightarrow$ crowdion jumps and indicating that direct octahedral $\rightarrow$ octahedral diffusion occurs near the twin.

The peak energy for the octahedral $\rightarrow$ hexahedral jumps is also reduced by up to 1 eV due the twin boundary, however the activation barriers are distributed over a wider range of energies when compared to the octahedral $\rightarrow$ octahedral jumps. The activation barriers for the octahedral $\rightarrow$ tetrahedral jumps in 0L to tetrahedral site T1 (paths highlighted in blue in Figure 5.9b), which relaxes from hexahedral site H1, are not significantly different from the bulk values.

The $(10\bar{1}2)$ twin boundary has a modest effect on the activation barrier of most octahedral $\rightarrow$ crowdion paths in the 0L layer. Although the peak energy of
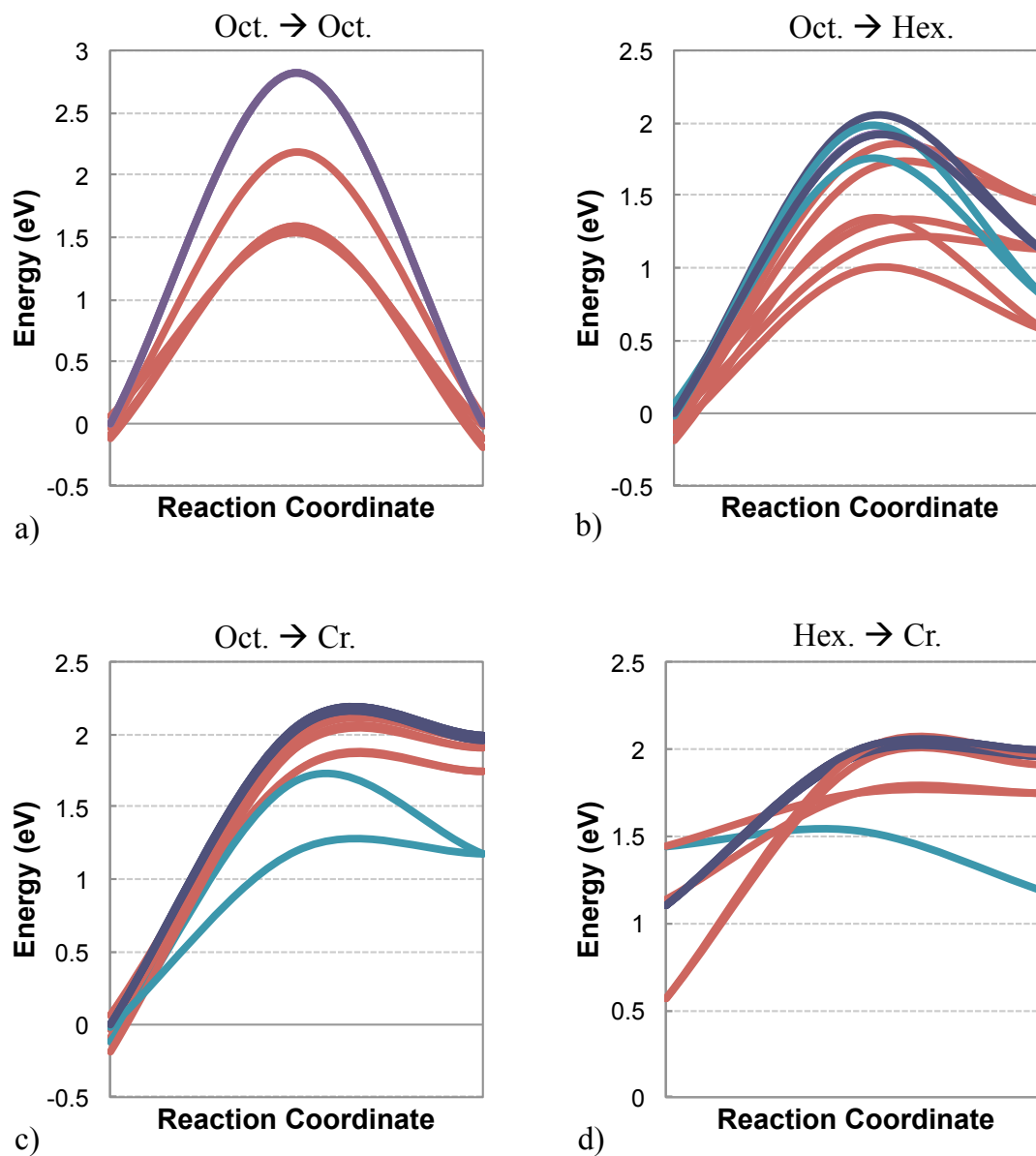
Figure 5.9: Site energy and activation barriers for diffusion paths in the 4L (purple) and 0L (red and blue) layers in Figure 5.7. The paths are grouped by the initial and final interstitial characteristics as a) octahedral → octahedral, b) octahedral → hexahedral, c) octahedral → crowdion, and d) hexahedral → crowdion. Paths in blue include a tetrahedral interstitial in the 0L layer.

some paths is reduced by about 0.4 eV, the peak energy for most paths near the twin is only slightly reduced. However, unlike the octahedral $\rightarrow$ hexahedral case, the octahedral $\rightarrow$ tetrahedral jump to tetrahedral site T2 (path highlighted in blue in Figure 5.9c), which relaxes from crowdion site C2, is significantly lower than other octahedral $\rightarrow$ crowdion paths in the bulk or near the twin. The formation of this tetrahedral interstitial in the twin therefore contributes to diffusion by providing a low energy path across the twin boundary.

Finally, the hexahedral $\rightarrow$ crowdion diffusion paths are also affected by the presence of the twin boundary. The peak energy for most of the paths near the twin is within 0.2 eV of the bulk case. The peak energy of the hexahedral $\rightarrow$ tetrahedral path to tetrahedral site T2 is much lower than the bulk equivalent, similar to the behavior of the octahedral $\rightarrow$ tetrahedral jump to the same site. On the other hand, the tetrahedral $\rightarrow$ crowdion path from T1 to C1 is unstable; the peak position relaxes into an neighboring octahedral interstitial and this path therefore does not appear in Figure 5.9d).

Having calculated the interstitial site formation energy and diffusion activation barriers for all sites and paths near the twin, we are able to assess the minimum energy pathways for diffusion. In bulk α-Ti the activation barrier for octahedral $\rightarrow$ octahedral diffusion is approximately 1 eV higher than the activation barriers for other paths [104, 117] and does not contribute significantly to diffusion. As a result, diffusion in the bulk as well as in the 4L layer proceeds by indirect jumps between the low energy octahedral sites via octahedral $\rightarrow$ hexahedral, octahedral $\rightarrow$ crowdion, and hexahedral $\rightarrow$ crowdion diffusion. The combinations of these jumps

yield the minimum energy paths far from the twin. Conversely, in the 0L layer there are several octahedral $\rightarrow$ octahedral jumps with activation barriers around 1.5 eV which contribute to diffusion along with the assorted low energy paths via other jumps. We have compiled the five lowest energy paths for a O interstitial to travel across 0L (to the twin boundary) for comparison with the lowest energy pathways for diffusion in the bulk. Other diffusion pathways near the twin exist, however the peak energy of the five paths selected here is about 0.3 eV lower than the next lowest energy path and thus this selection represents the most plausible options for O diffusion. Further, the structure is symmetrical about the twin boundary, so a diffusing O atom will experience the same energy landscape and activation barriers in order to diffuse away from the twin boundary.

A comparison of the lowest energy diffusion pathways across the twin with the lowest energy diffusion pathways in the bulk is provided in Figure 5.10. The peak energy of the bulk paths varies from 1.97 eV to 2.02 eV, closely aligned with both experimental [115] and DFT [104] results. The peak energy for diffusion across the 0L layer (and thus to, and across the twin boundary) varies from 1.53 eV to 1.68 eV, a reduction of $0.29 - 0.49$ eV. Diffusivity scales with $\exp(-\Delta E_B / k_B T)$, where E_B is the activation barrier energy, and a change in peak energy of this magnitude therefore has a large impact on the rate of O diffusion near and across the twin.

Unimpeded, twin growth is observed to occur at rates approaching the speed of sound in hcp metals (for example, [121, 122]). Hence despite accelerated kinetics, O diffusion near the twin is still comparatively slow and twin growth rate may be decreased by the presence of O. Compared to the activation barrier for O diffusion
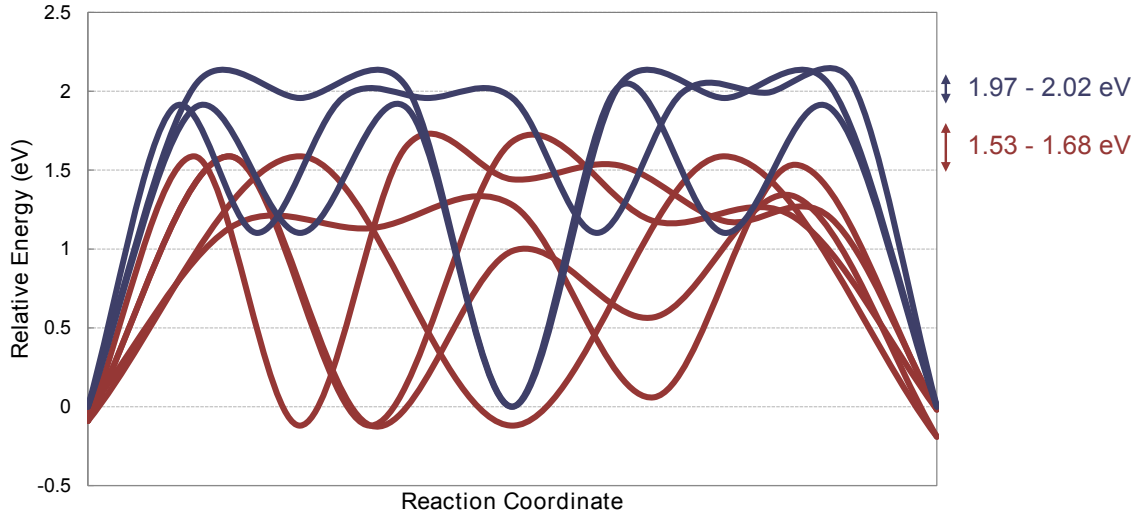
Figure 5.10: Minimum energy pathways for diffusion between two octahedral sites across the 4L layer (purple lines) and the 0L layer (red lines). The peak energy of the paths is also shown.

in the bulk, the reduced activation barrier for O diffusion across the twin boundary is closer to the experimentally measured activation energy for twin growth [16, 17]; however, the activation barriers for these processes still differ by almost 1 eV, and thus the interaction of twins and O interstitials likely occurs via a more complicated mechanism than serial twin boundary motion/oxygen diffusion. Nonetheless, the correct trend and relative similarity of the activation barrier for $(10\bar{1}2)$ twin growth and O diffusion near a $(10\bar{1}2)$ twin boundary suggests that the interaction mechanisms merit further study.

5.5 Conclusion

The interactions between alloying or impurity elements and twin growth are not well understood, despite opportunities for performance improvements across the many

hcp metals where deformation twinning is prevalent. In the case of α-Ti, experimental evidence suggests that O interstitials could result in time-dependent twinning by interfering with the twin growth process. As a first step towards understanding the mechanisms of these interactions, we have applied a combination of DFT and MEAM calculations to assess the effect of a $(10\bar{1}2)$ twin boundary on the formation energy of all unique O interstitial sites along with the diffusion activation barriers between the sites.

The formation energy of octahedral, hexahedral, and crowdion O interstitials is modified by as much as 0.5 eV near the twin boundary and returns to bulk-like values at a distance of about 10 Å from the twin. Two unique tetrahedral interstitials are stable in the twin boundary, despite being unstable in the bulk, with formation energies comparable to hexahedral interstitials. The effect of the twin boundary on formation energy is greatest for the hexahedral, crowdion, and tetrahedral sites, which are all higher energy when compared to the octahedral sites; as a result, O concentration near a twin boundary is similar to the bulk, however a larger fraction of interstitials near the twin will occupy non-octahedral sites.

The diffusion activation barriers for O near the $(10\bar{1}2)$ twin boundary are uniformly lower than in the bulk. In some cases the barriers are reduced by more than 1 eV due to a nearby twin boundary, creating many low energy diffusion pathways. Of the two unique tetrahedral interstitials in the twin boundary, only one contributes significantly to O diffusion while the other does not connect to a low energy diffusion path. Our MEAM calculations indicate that the peak energy for diffusion of O through bulk Ti is about 2 eV, corresponding well to measured

and DFT-calculated values. After reviewing the available paths for an O interstitial to move to and across a twin boundary, we find that the peak energy for diffusion is between 1.53 eV and 1.68 eV. Such a large reduction in peak energy indicates that O diffusion occurs much more readily across a twin boundary when compared to the bulk. However, accelerated O diffusion near the twin is still much slower than unimpeded twin growth and O is likely to play a role in strain-rate and time dependence in $(10\bar{1}2)$ twinning. That our newly reported activation barriers for diffusion near a $(10\bar{1}2)$ twin are still higher than the measured activation energy from twin growth indicates that the mechanisms of O-twin interaction are more complicated than a serial growth/diffusion process and merit further investigation.

Chapter 6: Conclusions

The research summarized in this dissertation provides new, quantitative insight into the interaction of phase boundaries and O interstitials with deformation twins in Ti. The detailed results are summarized here into key conclusions.

Elastic and plastic interaction stresses combine to produce anisotropic mechanical response during the onset of plasticity in the α-phase of dual-phase Ti alloys:

1. Elastic interaction stress significantly modifies the effective Schmid factor near the α-β interface. This interaction stress, due to the elastic mismatch and anisotropy of the α- and β-phases, resolves onto the available slip and twinning systems in the α-phase, increasing the effective Schmid factor by up to 30% and causing slip to occur at lower applied stress than would be expected from Schmid's Law. The elastic interaction stresses are strongly anisotropic and affect independent slip and twinning systems differently.

2. As the α-phase begins to deform plastically, the relative shear moduli of the α and β-phasees produce a repulsive force against dislocation motion in some orientations. This repulsive force significantly increases the CRSS for slip near the boundary for particular independent slip systems. Deformation twins are

similarly affected, although the magnitude of the effect is smaller

3. Interaction stress affects the active deformation mechanism for some orientations and promotes, for example, basal $\langle a \rangle$ slip and $(10\bar{1}2)$ twinning at the expense of prismatic $\langle a \rangle$ slip.

4. Combined, the interaction stresses affect the observed CRSS for each independent slip and twinning system. Our model results produce a distribution of observed CRSS for the basal and prismatic system that matches experimental results. This quantifies, for the first time, the source of CRSS varation and provides a clear mechanistic description of anisotropic plastic response in α-β Ti alloys.

A new validated and published modified embedded atom method (MEAM) potential for the Ti-O system is valuable for studying interactions of interstitial O with Ti:

1. The MEAM potential is fit to DFT calculated lattice constants, cohesive energies, elastic constants, and a diffusion barrier for Ti-O structures exhibiting a variety of bond distances, bond angles, and O concentrations. The quality of the fit is quite high across the fitting set, with most characteristics reproduced with less than 5% error.

2. The potential is validated by successfully reproducing the diffusion barriers for O in hcp Ti, properties of hcp Ti as a function of increasing O concentration, the lattice parameters and cohesive energies of many Ti-O structures, and the hydrostatic strain versus cohesive energy relationships for several structures.

3. The MEAM potential, fitting algorithms and Python scripts, and all related computational input and output files are available to the public via the NIST Computational Materials Data Repository, enabling other researchers to apply these tools and advance the state-of-the-art in empirical potential modeling.

The presence of a twin boundary in Ti affects the thermodynamic and kinetic properties of O interstitials with implications for twin-interstitial interactions and time-dependent twinning:

1. The formation energy of octahedral, hexahedral, and crowdion O interstitials is modified by as much as 0.5 eV near the twin boundary and returns to bulk-like values at a distance of about 10 Å from the twin. Two unique tetrahedral interstitials are stable in the twin boundary, despite being unstable in the bulk, with formation energies comparable to hexahedral interstitials.

2. The effect of the twin boundary on formation energy is greatest for the hexahedral, crowdion, and tetrahedral sites, which are all higher energy when compared to the octahedral sites; as a result, O concentration is unlikely differ significantly near a twin boundary as compared to the bulk, however a larger fraction of interstitials near the twin will occupy non-octahedral sites.

3. The diffusion activation barriers for O near the $(10\bar{1}2)$ twin boundary are uniformly lower than in the bulk. In some cases the barriers are reduced by more than 1 eV due to a nearby twin boundary, creating many low energy diffusion pathways.

4. Our MEAM calculations indicate that the peak energy for diffusion of O through a bulk Ti is about 2 eV, corresponding well to measured and DFT-calculated values. After reviewing the available paths for an O interstitial to move to and across a twin boundary, we find that the peak energy for diffusion is between 1.53 eV and 1.68 eV. Such a large reduction in the peak energy indicates that O diffusion occurs much more readily across a twin boundary when compared to the bulk. However, diffusion of O is still slower than unimpeded twin growth, suggesting that O interstitials can restrict twin growth rate.

Chapter 7:   Recommendations for Future Work

Several interesting opportunities exist for future exploration of interaction stress effects in α-β Ti alloys based on the results described in this work:

1. As plastic strain continues to increase, yield occurs in the β phase. The interaction of α plasticity with β plasticity is not well modeled or understood. Producing FEM models which include plastic response in both phases (e.g. twinning in α and stress induced martensite in β) will support interrogation of the system at large plastic strains.

2. A unique opportunity exists to apply atomistic modeling to the study of interphase interaction stress. The current work provides a systematic quantification of interaction stresses using continuum theory and modeling techniques; conducting a similar study using atomistic models (particularly MEAM potential models) would allow for local, atom-level redistribution of strains, development of misfit dislocations, and a thorough investigation of dislocation-boundary interactions without continuum theory assumptions.

Using the tools and techniques described here, continued work in MEAM potential development would be of great value to the materials science and engineering community:

1. The brute force MEAM fitting algorithm produced here is suitable for application to other elements and systems. There are no published ternary MEAM potentials for Ti-O, such as Ti-Al-O, Ti-V-O, Ti-Mo-O, or Ti-Mn-O. The practical relevance of these alloy systems suggests that they are worthy of further study requiring new MEAM potentials.

Due to the vast landscape of possibilities, many interesting features of Ti-O interaction are left unexplored:

1. Generalized stacking fault energy (GSFE) curves for the $(10\bar{1}2)$ plane are not reported in the literature. Calculating the GSFE as a function of O concentration would provide insight into the effects of interstitial impurities on the shear process during twin growth.

2. While the $(10\bar{1}2)$ twin nucleation and growth process has not been rigorously defined, MEAM simulations of twinning dislocation motion under an applied shear stress would provide the most direct insight into the effects of O interstitials on twin growth in Ti. These calculations are extremely challenging and should be approached with great care. The efficacy of the reported MEAM potential in reproducing the correct dislocation characteristics must be determined, and careful consideration of calculation setting must occur in order to model the real, physical system.

3. Experimental measurement of twin growth in Ti as a function of O concentration would be of great value. For example, statistically significant measurement of twin characteristics from samples of CP Ti grades 1 through 4

subjected to mechanical testing from creep through dynamic loading would provide unique and currently unreported insight into the relationships between twin growth and O interstitials.

Appendix A: Appendix A: Calculation of Elastic Properties as Function of Orientation

Implementing orientation changes in the finite element models requires that we calculate the correctly rotated elastic compliance tensors for each phase starting from reported values of α phase compliance at room temperature (S11=0.958, S33=0.698, S44=2.141, S12=-0.462, S13=-0.189, S66=2.841, x10-11 Pa) [35] and β phase compliance at room temperature, in this case measured using samples of Ti-10Cr (wt%) (S11=1.857, S44=2.3420, S12=-0.774, S66=2.342, x10-11 Pa) [19]. These compliance tensors must be rotated to the (x', y', z') coordinate system (Figure 3.3) for each scenario to be input into ANSYS®. Many aspects of this study – for example rotating the elastic compliance tensors and resolving the stress onto different deformation systems – require tensor rotations between coordinate systems using the corresponding direction cosines. However, the angles (and direction cosines) between two points on the stereographic projection are difficult to determine when the points are reported in different coordinate systems. To facilitate calculation of the direction cosines we perform three operations: (1) convert α indices from Miller-Bravais (α-hex) to α-orthorhombic (α-orth), (2) convert β indices from Miller (β-mil) to α-orth, and (3) calculate the α-orth indices of arbitrary points on the stereographic

projection.

A.1   Conversion of α-hex to α-orth

The Miller-Bravais four index notation for crystallographic planes and directions in hexagonal crystal structures is a useful system that accurately portrays the symmetry in hexagonal materials. However, the use of a four index non-orthogonal basis introduces significant complications where conventional tensor mathematics and linear algebra are widely employed. To enable straightforward crystallographic calculations in the hexagonal α-Ti phase, the four index Miller-Bravais indices must be converted to a three index orthogonal system. To accomplish this, we use a technique outlined by Niewczas [123]. First, the α-hex indices are converted to three index α rhombohedral (α-rhom) indices, which are non-orthogonal. Transformation from α-rhom to α-orth is then accomplished using the reported transformation matrix, $\mathbf{A}$,

$$\mathbf{A} = \begin{bmatrix} 1 & -\frac{1}{2} & 0 \\ 0 & \frac{\sqrt{3}}{2} & 0 \\ 0 & 0 & \frac{c}{a} \end{bmatrix} \tag{A.1}$$

where a and c are the lattice parameters of the hexagonal material. Conversion between a rhombohedral direction vector, $\mathbf{R}_{[UVW]}$, and an orthogonal direction vector, $\mathbf{R}_{[xyz]}$, is accomplished using the relationships

$$\mathbf{R}_{[xyz]} = \mathbf{A}\mathbf{R}_{[UVW]} \tag{A.2}$$

and

$$\mathbf{R}_{[UVW]} = \mathbf{A}^{-1}\mathbf{R}_{[xyz]} \tag{A.3}$$

Conversion between a rhombohedral plane normal, $\mathbf{n}_{(HKL)}$, and an orthogonal plane normal, $\mathbf{n}_{(xyz)}$, is accomplished using the relationships

$$\mathbf{n}_{[xyz]} = \mathbf{n}_{[HKL]}\mathbf{A}^{-1} \tag{A.4}$$

and

$$\mathbf{n}_{[HKL]} = \mathbf{n}_{[xyz]}\mathbf{A} \tag{A.5}$$

A.2 Conversion of β-mil to α-orth

The relative orientation of the β-phase and the α-phase in Ti is defined by the $(\bar{5}140)_\alpha||(\bar{3}34)_\beta$ interface plane and a $\langle 1\bar{2}10\rangle(0001)_\alpha||\langle 1\bar{1}1\rangle(110)_\beta$ Burgers orientation relationship. This relationship dictates that any direction vector or plane-normal vector in the β-phase is parallel to a unique vector in the α-phase. To enable easy calculation of the angle between a β-phase direction and an α-phase direction it is necessary to convert the β-phase vector into the α-orth system (this is equivalent to finding the α-phase direction that is parallel to a given β-phase direction). We accomplish this by calculating the direction cosines between the α-orth basis and the β-mil basis, then using the cosines as the rotation tensor between the systems. The components of the rotation tensor, Q_{ij}, are calculated as

$$Q_{ij} = \alpha_i \beta j \tag{A.6}$$

where $\alpha_i \beta j$ is the cosine of the angle between the basis vectors α_i and βj,

$$\alpha_1 = (2\bar{1}\bar{1}0)_{\alpha-hex} = (100)_{\alpha-orth}$$

$$\alpha_2 = (01\bar{1}0)_{\alpha-hex} = (010)_{\alpha-orth}$$

$$\alpha_2 = (0001)_{\alpha-hex} = (001)_{\alpha-orth}$$

and

$$\beta_1 = (100)_{\beta-mil}$$

$$\beta_2 = (010)_{\beta-mil}$$

$$\beta_3 = (001)_{\beta-mil}$$

We calculated the angles between these vectors to generate the rotation tensor, **Q**,

$$\mathbf{Q} = \begin{bmatrix} 0.6449 & -0.6449 & -0.4099 \\ -0.2899 & 0.2899 & -0.9121 \\ 0.7071 & 0.7071 & 0 \end{bmatrix} \tag{A.7}$$

which is then used to convert $\beta - mil$ indices to $\alpha - orth$ indices using the relationship

$$\alpha_{\mathbf{orth}} = \mathbf{Q}\beta_{\mathbf{mil}} \tag{A.8}$$

A.3 Calculation of the Indices of an Arbitrary Plane

The analysis performed in this study includes arbitrary rotations of the crystal orientation relative to the sample loading orientation; this is equivalent to moving the position of the loading axis to an arbitrary point on the stereographic projection.

The α_{orth} indices of an arbitrary point are therefore necessary in order to perform the rotations of the elastic compliance tensors and to calculate the resolved shear stresses. For this study, the loading axis was rotated in $10°$ increments away from the $(\bar{5}140)_{\alpha-hex}$ pole, then in $10°$ increments away from the $(\bar{1}3\bar{2}0)_{\alpha-hex}$ pole to generate the set of loading axis locations shown in Figure 3.4.

The α_{orth} indices of the orientations identified in Figure 3.4 were calculated using the relationship between the dot product of two vectors, $\vec{u}$ and $\vec{v}$, and the angle between the vectors, namely

$$\cos(\theta) = \frac{\vec{u} \cdot \vec{v}}{|\vec{u}|\,|\vec{v}|} = \frac{u_1 v_1 + u_2 v_2 + u_3 v_3}{\sqrt{(u_1^2 + u_2^2 + u_3^2)(v_1^2 + v_2^2 + v_3^2)}} \tag{A.9}$$

where θ is the angle between the vectors and u_i and v_j are the vector components. A system of two equations is established for each arbitrary point using the $\alpha - orth$ indices of the $(\bar{5}140)_{\alpha-hex}$ and $(\bar{1}3\bar{2}0)_{\alpha-hex}$ poles as the vectors $\vec{u}$ and assigning the unknown indices of the arbitrary point to the vector $\vec{v}$. The value of θ from both the $(\bar{5}140)_{\alpha-hex}$ and $(\bar{1}3\bar{2}0)_{\alpha-hex}$ poles is known owing to the $10°$ increments of rotation employed here. While there are three components of $\vec{v}$, a system of two equations is sufficient if we consider the characteristics of the α (0001) stereographic projection; for all points on the outer diameter of the stereographic projection (which are at $90°$ from α (0001)) the value of v_3 is 0. For all points inside the outer diameter of the stereographic projection the value of v_3 is something other than zero. The actual values of the components v_i are not important – only the ratio between the components is significant when determining the indices of a point on the stereographic projection. Therefore the value of v_3 can be set to 1 for any

point inside the outer diameter of the stereographic projection and 0 for any point on the outside diameter. Hence the system of two equations using the angles from the $(\bar{5}140)_{\alpha-hex}$ and $(\bar{1}3\bar{2}0)_{\alpha-hex}$ poles poles is sufficient to determine the vector $\vec{v}$ and the indices of the arbitrary point. After calculating the indices for each of the 91 orientation scenarios the elastic compliance matrices and resolved stresses are easily rotated to the required orientation as described above.

Appendix B: Appendix B: Simulating Twinning in ANSYS

Deformation twinning occurs by an eigenstrain which is stress free in the absence of a surrounding medium. However, real deformation twins grow while surrounded by a matrix which constrains the twinning process and produces complicated stress fields. Further, while real twins can take any number of complex shapes, they are often modeled as an ellipsoidal volume. This approximation is used both because the true shape of deformation twins is nearly ellipsoidal in many cases, and Eshelby produced a convenient analytical solution for the stress field due to an ellipsoidal volume experiencing a shear eigenstrain [54, 55]. However, Eshelby's solution is only valid for a twin deforming in an infinite matrix whereas twinning often occurs near boundaries in a real microstructure. This section describes a method for simulating twinning eigenstrain in ANSYS, as well as constructing a finite element model and mesh of an ellipsoidal volume near a boundary.

B.1   Constructing and Meshing and Ellipsoidal Volume

The primary challenge in modeling and meshing an ellipsoidal volume in ANSYS is to produce a twin volume that the ANSYS can successfully mesh without incurring tremendous computational cost due to a very fine mesh. While other paths towards

this outcome may exist, the following steps were applied in this study to produce a working model and mesh. These instructions assume that the user is familiar with the basics of modeling and meshing in ANSYS.

1. Select two element types in the preprocessor: the solid element for modeling (e.g. SOLID186) and the MESH200 element. In the MESH200 element options, set the "Element shape and # of nodes K1" to "QUAD 8-NODE."

2. Create a material model for the twin. First, input the elastic properties of the twin (e.g. modulus and Poisson's ratio). Second, add a "Thermal Expansion" model, select "Secant Coefficient", and select "Orthotropic." Set the reference temperature to 0 and create two temperature columns. In the first temperature column, set the temperature to zero and set each of the secant thermal expansion values to 0.0. In the second column, set the temperature to 10, set ALPX to negative one-tenth of one-half of the twinning shear, set ALPY to positive one-tenth of one-half of the twinning shear, and set ALPZ to 0.0. The final result should appear as shown in Figure B.1. Note that in this case the model simulates $(10\bar{1}2)$ twinning which has a characteristic shear of 0.174; one-tenth of one-half of this value is 0.0087. The purpose of this step is to use the ANSYS thermal expansion functionality to model twinning. Thermal expansion also occurs by an eigenstrain, and hence a carefully crafted set of material characteristics can result in thermal expansion behavior that produces a twinning shear eigenstrain.

3. Create a new coordinate system using the CLOCAL command as follows: "CLOCAL,20,0,0.0,0.0,0.0,45,0.0,0.0" then set the active coordinate system back to Global Cartesian (menu → WorkPlane → Set Active WP to... → Global Cartesian). As written here, the CLOCAL command assumes that the global origin is at the center of the ellipsoid. Adjust the XL, YL, and ZL values in the command to place the origin of the new coordinate system at the center of the ellipsoid, if it is not the global origin.

4. Construct a sphere centered at the origin with a radius equal to the desired length of the long axis for the ellipsoid.

5. Use the "scale" function to convert the sphere into an ellipsoid. For example, to produce an oblate ellipsoid with an axial ratio of 1:10, scale the x distance to 1, the y distance to 0.1, and the z distance to 1.

6. In order to facilitate meshing, it is necessary to slice the ellipsoid into sub-volumes; in this study, slicing the ellipsoid into quarters was found to yield the most computationally effective mesh. Create an area that passes through the center of the ellipse in the x-y plane, then use the "VSBA" command to slice the ellipse in half and delete the area. Repeat with an area passing through the center of the ellipse in the z-y plane.

7. In order to facilitate meshing, it is also necessary to create a sub-volume in the center of the ellipsoid. Create a cylindrical area that passes through the center of the ellipsoid, then use the "VSBA" command to slice the ellipse and

delete the cylindrical area. The final result of the slicing operations should produce a set of volumes as shown in Figure B.2.

8. Construct a box around the ellipsoid. The purpose of this box is to generate a region in the matrix, near the ellipsoid, that has a very fine mesh size; this box will also make it easier to mesh the final model. The box should be larger in all dimensions that the ellipsoid, however the extent of its size will depend on the model at hand. For example, in this study an ellipsoid measuring 20 x 2 x 20 units was surrounded by a box measuring 42 x 4 x 42 units.

9. The box will be solid, overlapping with the volume of the ellipsoid. Subtract the volume of the ellipsoid from the volume of the box in order to produce a box with an ellipsoidal void using the "VSBV" command.

10. Construct the remaining volumes for the model around the ellipsoid and box.

11. Glue all of the model volumes together.

12. Select one of the cross-section areas of the sliced ellipse (Fig B.3), set the mesh attributes to the MESH200 element, for the material model of the twin, in the coordinate system created using the CLOCAL command (system number 20 in the above command). Select the outer ellipsoid volumes and set the mesh attributes to the SOLID186 element for the material model of the twin in the coordinate system created using the CLOCAL command from above.

13. Open the MeshTool, Turn off SmartSize meshing, set the Global mesh size to a reasonable value, and mesh the cross-section area. Adjust the Global mesh
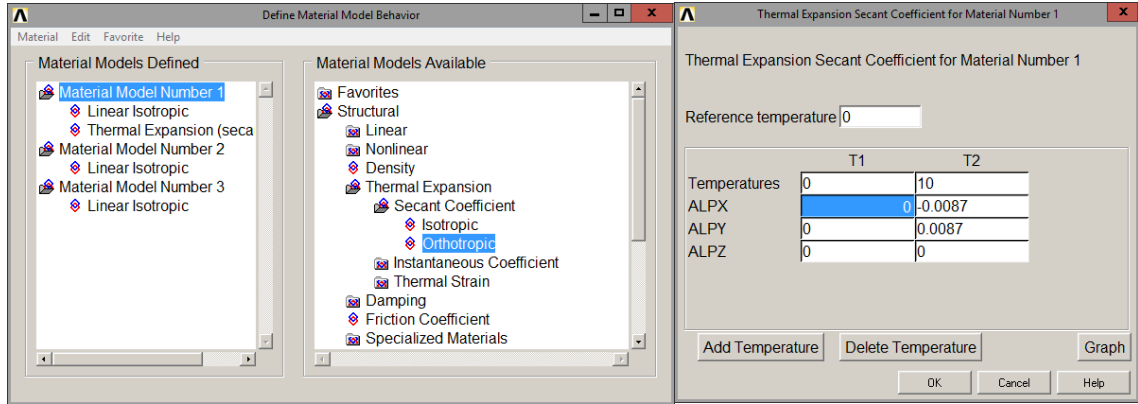
Figure B.1: Screenshot of material property settings necessary to induce a shear eigenstrain of 0.174 upon heating the material to a temperature of 10 (arbitrary units).

size and re-mesh until you produce an acceptable mesh.

14. Sweep the area mesh through the first quarter of the ellipsoid using the "VSWEEP" command. Repeat for each quarter of the ellipsoid.

15. Turn on SmartSize and mesh the center cylinder of the ellipsoid, adjusting the size until a reasonable mesh is achieved.

16. Turn off SmartSize and mesh the box surrounding the ellipsoid using the same mesh size as the ellipsoid.

17. Turn on SmartSize and mesh the remaining volumes in the model.

B.2 Simulating Twin Formation

After completing the model and mesh, the following steps will initiate a simulation of twin deformation by imposing a shear eigenstrain in the twin volume while capturing
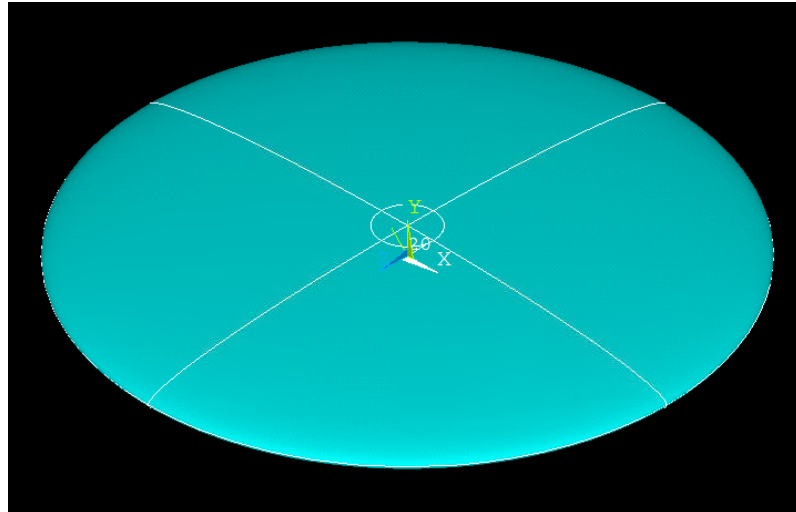
Figure B.2: Result of modeling steps to produce an ellipsoidal volume that can be meshed and simulated with reasonable computational effort.
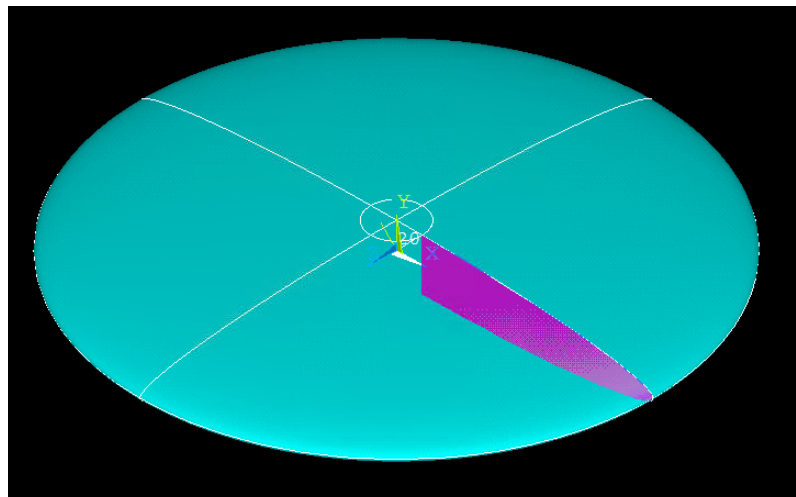
Figure B.3: Area produced by modeling operations suitable for meshing with MESH200 area elements. The resulting mesh should be swept around the short axis of the ellipsoid.

the influence of the surrounding volume on the twin.

1. Apply boundary conditions suitable for the particular scenario. In this study, the following boundary conditions yielded FEM results very similar to Eshelby's solution for twinning in an infinite matrix: constrain nodes at $x = 0$ to 0 displacement in the x-direction, couple nodes at $x = x_{max}$ to displace the same amount in the x-direction, constrain nodes at $y = 0$ to 0 displacement in the y-direction, couple nodes at $y = y_{max}$ to displace the same amount in the y-direction, constrain nodes at $z = 0$ to 0 displacement in the z-direction, couple nodes at $z = z_{max}$ to displace the same amount in the z-direction, where x_{max}, y_{max}, and z_{max} are the boundaries opposite $x = 0$, $y = 0$, and $z = 0$ boundaries.

2. In the solution menu, select Setting, Apply Loads, etc. Set the initial temperature to 10. The actual temperature is arbitrary, but it must match the value used in setting the thermal expansion properties.

3. Run the solution.

Appendix C: Appendix C: Mathematical Details of the Modified Embedded Atom Method

While the conceptual principles of the Modified Embedded Atom Method (MEAM) are common, there are differences in the mathematical construction of various MEAM implementations. He we provide the details of the MEAM implementation used in this study such that the reader can better understand and reproduce our results. We have generally followed the technique as described by Lee et al. [88, 89].

In the MEAM the total energy of a system is represented as the sum of energy across all atoms, i, by

$$E_{Tot} = \sum_i \left[F_i(\rho_i) + \Phi_i(R_{ij}) \right] \tag{C.1}$$

where ρ_i is the charge density at the location of an atom and R_{ij} is the distance between atoms i and j; the energy of each atom is due to an embedding energy that varies with charge density at an atom's position, $F_i(\rho_i)$, and an interatomic potential that varies with the distance between neighboring atoms, $\Phi_i(R_{ij})$.

Charge density in the MEAM is computed in several steps. First, each atom is surrounded by four components of atomic charge density $\rho^{\alpha(h)}$ for $h = (0-3)$,

described as a function of distance from the atom, R, by

$$\rho^{\alpha(h)}(R) = \exp\left[-\beta^{(h)}\left(\frac{R}{r_e} - 1\right)\right] \qquad \text{(C.2)}$$

where r_e is the equilibrium nearest neighbor distance in a reference structure and the four $\beta^{(h)}$ parameters describe the decay of the electron density for increasing R. The atomic electron densities from all atoms within a specific cutoff radius are then combined into partial electron densities $\rho_i^{(h)}$ for $h = (0 - 3)$ using the method described in Lee [88]. Finally, the total charge density at atom i, $\bar{\rho}_i$, is calculated as the combination of the partial charge densities by

$$\bar{\rho}_i = \rho_i^{(0)} G(\Gamma) \qquad \text{(C.3)}$$

where, from among several available methods, we use

$$G(\Gamma) = \frac{2}{1 + \exp(-\Gamma)} \qquad \text{(C.4)}$$

and

$$\Gamma = \sum_{h=1}^{3} t_i^{(h)} \left[\frac{\rho_i^{(h)}}{\rho_i^{(0)}}\right]^2 \qquad \text{(C.5)}$$

where $t_i^{(h)}$ are fitting constants. Finally, the embedding energy for each ion is calculated from the charge density by

$$F_i(\rho_i) = AE_c \frac{\bar{\rho}_i}{\bar{\rho}_0} \ln \frac{\bar{\rho}_i}{\bar{\rho}_0} \qquad \text{(C.6)}$$

where A is a fitting parameter, E_c is the cohesive energy of the reference structure, and $\bar{\rho}_0$ is a charge density scaling factor.

The interatomic potential in MEAM is given by considering the change in system energy as a function of nearest neighbor distance, R_{ij}. The change in energy

is calculated using the universal equation of state for metals by Rose [124],

$$E(R_{ij}) = -E_c(1 + a^* + da^{*3})\exp(-a^*) \tag{C.7}$$

where d is an adjustable parameter that we set to zero and

$$a^* = \alpha\left(\frac{R_{ij}}{r_e} - 1\right) \tag{C.8}$$

The parameter α is a function of the bulk modulus, B, and the equilibrium atomic volume, Ω, calculated as

$$\alpha = \left(\frac{9B\Omega}{E_c}\right)^{1/2} \tag{C.9}$$

We note for clarity that α in equation C.2 is unrelated to α in equations C.8 and C.9; we use the variable α in both cases for consistency with the standard description of the MEAM.

Several parameters described here are only necessary for single-element MEAM potentials; in this study we fit a new potential for the Ti-O system using a Ti potential from Kim, Lee, and Baskes [91] and an O potential from Baskes [92]. Because we are using existing single-element potentials, we do not report new values for the parameters $\beta^{(h)}$, $t_i^{(h)}$, and A, which can be found in the literature [91, 92]; however we include an explanation of these parameters here in order to provide a more comprehensive description of the technique and to clarify the particular implementation of the MEAM used in this study.

Bibliography

[1] G. Lutjering and J. Williams, *Titanium*. Berlin, New York: Springer, 2 ed., 2007.

[2] C. Leyens and M. Peters, *Titanium and Titanium Alloys*. Weinheim: Wiley-VCH, 2003.

[3] M. Peters, J. Kumpfert, C. H. Ward, and C. Leyens, "Titanium alloys for aerospace applications," *Adv. Eng. Mat.*, vol. 5, no. 6, pp. 419–427, 2003.

[4] C. Elias, J. Lima, R. Valiev, and M. Meyers, "Biomedical applications of titanium and its alloys," *JOM*, vol. 60, no. 3, pp. 46–49, 2008.

[5] R. Schutz, C. Baxter, P. Boster, and F. Fores, "Applying titanium alloys in drilling and offshore production systems," *JOM*, vol. 53, no. 4, pp. 33–35, 2001.

[6] R. A. Lindemann and C. J. Voorhees, "Mars exploration rover mobility assembly design, test and performance," in *Systems, Man and Cybernetics, 2005 IEEE International Conference on*, vol. 1, pp. 450–455, IEEE, 2005.

[7] J. Murray and H. Wriedt, "The O-Ti (oxygen-titanium) system," *J. Phase Equilib.*, vol. 8, no. 2, pp. 148–165, 1987.

[8] K. Chan, C. Wojcik, and D. Koss, "Deformation of an alloy with lamellar microstructure: Experimental behavior of individual Widmanstatten colonies of an $\alpha - \beta$ Titanium alloy," *Met. Trans. A*, vol. 12, pp. 1899–1907, 1981.

[9] S. Naka, A. Lasalmonie, P. Costa, and L. Kubin, "The low-temperature plastic deformation of α-titanium and the core structure of a-type screw dislocations," *Phil. Mag. A*, vol. 57, no. 5, pp. 717–740, 1988.

[10] F. Bridier, P. Villechaise, and J. Mendez, "Analysis of the different slip systems activated by tension in a α/β titanium alloy in relation with local crystallographic orientation," *Acta Mat.*, vol. 53, pp. 555–567, 2005.

[11] M. Battaini, E. Pereloma, and C. Davies, "Orientation effect on mechanical properties of commercially pure titanium at room temperature," *Met. Trans. A*, vol. 38, no. 2, pp. 276–285, 2007.

[12] N. Stanford, U. Carlson, and M. Barnett, "Deformation twinning and the Hall-Petch relation in commercial purity Ti," *Met. Trans. A.*, vol. 39, pp. 934–944, 2008.

[13] A. Jaworski and S. Ankem, "Influence of the second phase on the room-temperature tensile and creep deformation mechanisms of α-β Titanium alloys: Part I. tensile deformation," *Met. Trans. A*, vol. 37, pp. 2739–2754, 2006.

[14] P. Oberson and S. Ankem, "Why twins do not grow at the speed of sound all the time," *Phys. Rev. Lett.*, vol. 95, no. 16, p. 165501, 2005.

[15] A. Aiyangar, B. Neuberger, P. Oberson, and S. Ankem, "The effects of stress level and grain size on the ambient temperature creep deformation behavior of an alpha Ti-1.6 wt pct V alloy," *Met. Trans. A*, vol. 36, pp. 637–644, 2005.

[16] P. Oberson, Z. Wyatt, and S. Ankem, "Modeling interstitial diffusion controlled twinning in alpha titanium during low-temperature creep," *Scripta Mat.*, vol. 65, no. 7, pp. 638–641, 2011.

[17] Z. Wyatt, W. Joost, D. Zhu, and S. Ankem, "Deformation mechanisms and kinetics of time-dependent twinning in an α-titanium alloy," *International Journal of Plasticity*, vol. 39, pp. 119–131, 2012.

[18] C. Greene and S. Ankem, "Modelling of elastic interaction stresses in two-phase materials by fem," *Mat. Sci. Eng. A*, vol. 202, no. 1, pp. 103–111, 1995.

[19] S. Ankem and H. Margolin, "The role of elastic interaction stresses on the onset of plastic flow for oriented two ductile phase structures," *Met. Trans. A*, vol. 11, no. 6, pp. 963–972, 1980.

[20] Y. Guo, T. Britton, and A. Wilkinson, "Slip band-grain boundary interactions in commercial-purity titanium," *Acta Mat.*, vol. 76, pp. 1–12, 2014.

[21] A. Jenkins and H. Worner, "The structure and some properties of titanium-oxygen alloys containing 0-5 at.-% oxygen," *J. Inst. Metals*, vol. 80, 1951.

[22] A. Churchman, "The slip modes of titanium and the effect of purity on their occurrence during tensile deformation of single crystals," *Proc. R. Soc. Lond., A*, vol. 226, no. 1165, pp. 216–226, 1954.

[23] G. Welsch and W. Bunk, "Deformation modes of the α-phase of Ti-6Al-4V as a function of oxygen concentration and aging temperature," *Met. Trans. A*, vol. 13, no. 5, pp. 889–899, 1982.

[24] H. Conrad, "Effect of interstitial solutes on the strength and ductility of titanium," *Prog. Mater. Sci.*, vol. 26, no. 2, pp. 123–403, 1981.

[25] E. Metzbower, "X-ray-line-profile analysis of titanium alloys," *Met. Trans. A*, vol. 8, no. 2, pp. 279–282, 1977.

[26] P. Kwasniak, M. Muzyk, H. Garbacz, and K. Kurzydlowski, "Influence of C, H, N, and O interstitial atoms on deformation mechanism in titanium – first principles calculations of generalized stacking fault energy," *Materials Lett.*, vol. 94, pp. 92–94, 2013.

[27] M. Bhatia, X. Zhang, M. Azarnoush, G. Lu, and K. Solanki, "Effects of oxygen on prismatic faults in α-ti: a combined quantum mechanics/molecular mechanics study," *Scripta Mat.*, vol. 98, pp. 32–35, 2015.

[28] S. Ankem, C. Greene, and S. Singh, "Time dependent twinning during ambient temperature creep of α ti mn alloy," *Scripta Met. Mat.*, vol. 30, no. 6, pp. 803–808, 1994.

[29] C. Beevers and J. Robinson, "Some observations on the influence of oxygen content on the fatigue behaviour of α-titanium," *J. Less Comm. Met.*, vol. 17, no. 4, pp. 345–352, 1969.

[30] M. Biget and G. Saada, "Effect of interstitial impurities on twinning of titanium and zirconium," *J. de Physique III*, vol. 5, no. 11, pp. 1833–1840, 1995.

[31] R. G. Hennig, D. R. Trinkle, J. Bouchet, S. G. Srinivasan, R. C. Albers, and J. W. Wilkins, "Impurities block the α to ω martensitic transformation in titanium," *Nature Mat.*, vol. 4, no. 2, pp. 129–133, 2005.

[32] E. Cerreta, G. Gray Iii, R. Hixson, P. Rigg, and D. Brown, "The influence of interstitial oxygen and peak pressure on the shock loading behavior of zirconium," *Acta Mat.*, vol. 53, no. 6, pp. 1751–1758, 2005.

[33] M. Ghazisaeidi and D. Trinkle, "Interaction of oxygen interstitials with lattice faults in Ti," *Acta Mat.*, vol. 76, pp. 82–86, 2014.

[34] W. J. Joost, S. Ankem, and M. M. Kuklja, "A modified embedded atom method potential for the titanium-oxygen system," *Mod. Sim. Mat. Sci. Eng.* submitted for publication, 2014.

[35] E. Fisher and C. Renken, "Single-crystal elastic moduli and the hcp-bcc transformation in Ti, Zr, and Hf," *Phys. Rev.*, vol. 135, no. 2A, p. A482, 1964.

[36] C. Rhodes and J. Williams, "Observations of an interface phase in the α/β boundaries in titanium alloys," *Met. Mat. Trans. A*, vol. 6, no. 8, pp. 1670–1671, 1975.

[37] B. D. Cullity and S. R. Stock, *Elements of X-ray Diffraction*. Pearson, 2001.

[38] S. Ankem and H. Margolin, "A rationalization of stress-strain behavior of two-ductile phase alloys," *Met. Trans. A*, vol. 17, no. 12, pp. 2209–2226, 1986.

[39] S. Ankem and H. Margolin, "Finite element method (FEM) calculations of stress-strain behavior of alpha-beta Ti-Mn alloys: Part II. Stress and strain distributions," *Met. Trans. A*, vol. 13, no. 4, pp. 603–609, 1982.

[40] V. Hasija, S. Ghosh, M. J. Mills, and D. S. Joseph, "Deformation and creep modeling in polycrystalline Ti–6Al alloys," *Acta Mat.*, vol. 51, no. 15, pp. 4533–4549, 2003.

[41] W. Hutchinson and M. Barnett, "Effective values of critical resolved shear stress for slip in polycrystalline magnesium and other hcp metals," *Scripta Mat.*, vol. 63, no. 7, pp. 737–740, 2010.

[42] K. S. Chan, "A micromechanical analysis of the yielding behavior of individual widmanstätten colonies of an $\alpha+\beta$ titanium alloy," *Met. Trans. A*, vol. 35, no. 11, pp. 3409–3422, 2004.

[43] A. Ramesh and S. Ankem, "The effect of grain size on the ambient temperature creep deformation behavior of a beta Ti-14.8 V alloy," *Met. Trans. A*, vol. 33, no. 4, pp. 1137–1144, 2002.

[44] J. Weertman and J. Weertman, *Elementary Dislocation Theory*. New York: Oxford University Press, 1 ed., 1992.

[45] A. Head, "The interaction of dislocations and boundaries," *Phil. Mag.*, vol. 44, no. 348, pp. 92–94, 1953.

[46] E. Pacheco and T. Mura, "Interaction between a screw dislocation and a bimetallic interface," *J. Mech. Phys. Solids*, vol. 17, pp. 163–170, 1969.

[47] Y. Shen and P. M. Anderson, "Transmission of a screw dislocation across a coherent, non-slipping interface," *J. Mech. Phys. Sol.*, vol. 55, no. 5, pp. 956–979, 2007.

[48] S. I. Rao and P. M. Hazzledine, "Atomistic simulations of dislocation–interface interactions in the cu-ni multilayer system," *Phil. Mag. A*, vol. 80, no. 9, pp. 2011–2040, 2000.

[49] D. Tromans, "Elastic anisotropy of HCP metal crystals and polycrystals," *Int. J. of Res. Rev. App. Sci.*, vol. 6, no. 4, pp. 462–483, 2011. http://arpapress.com/Volumes/Vol6Issue4/IJRRAS_6_4_14.pdf.

[50] E. Date and K. Andrews, "Anisotropic and composition effects in the elastic properties of polycrystalline metals," *J. Phys. D: Appl. Phys.*, vol. 2, no. 10, p. 1373, 1969.

[51] S. Suri, G. Viswanathan, T. Neeraj, D.-H. Hou, and M. Mills, "Room temperature deformation and mechanisms of slip transmission in oriented single-colony crystals of an α/β titanium alloy," *Acta Mat.*, vol. 47, no. 3, pp. 1019–1034, 1999.

[52] M. Savage, J. Tatalovich, M. Zupan, K. Hemker, and M. Mills, "Deformation mechanisms and microtensile behavior of single colony ti–6242si," *Mat. Sci. Eng. A*, vol. 319, pp. 398–403, 2001.

[53] M. Savage, J. Tatalovich, and M. Mills, "Anisotropy in the room-temperature deformation of α–β colonies in titanium alloys: role of the α–β interface," *Phil. Mag.*, vol. 84, no. 11, pp. 1127–1154, 2004.

[54] J. Eshelby, "The determination of the elastic field of an ellipsoidal inclusion, and related problems," in *Proc. Roy. Soc. of London A.*, vol. 241, pp. 376–396, The Royal Society, 1957.

[55] J. Eshelby, "The elastic field outside an ellipsoidal inclusion," *Proc. Roy. Soc. of London A.*, vol. 252, no. 1271, pp. 561–569, 1959.

[56] M. Barnett, M. Setty, and F. Siska, "Estimating critical stresses required for twin growth in a magnesium alloy," *Met. Trans. A*, vol. 44, no. 7, pp. 2962–2969, 2013.

[57] A. Jaworski Jr and P. S. Ankem, "Influence of the second phase on the room-temperature tensile and creep deformation mechanisms of α-β titanium alloys, part ii: Creep deformation," *Met. Trans. A*, vol. 37, no. 9, pp. 2755–2765, 2006.

[58] T. Sakai and M. Fine, "Plastic deformation of ti-al single crystals in prismatic slip," *Acta Met.*, vol. 22, no. 11, pp. 1359–1372, 1974.

[59] J. Williams, R. Baggerly, and N. Paton, "Deformation behavior of hcp ti-al alloy single crystals," *Met. Mat. Trans. A*, vol. 33, no. 13, pp. 837–850, 2002.

[60] I. Jones and W. Hutchinson, "Stress-state dependence of slip in titanium-6al-4v and other hcp metals," *Acta Met.*, vol. 29, no. 6, pp. 951–968, 1981.

[61] A. Akhtar and E. Teghtsoonian, "Prismatic slip in α-titanium single crystals," *Met. Mat. Trans. A*, vol. 6, no. 12, pp. 2201–2208, 1975.

[62] S. Y. Betsofen, A. Ilyin, V. Plikhunov, A. Plotnikov, and A. Filatov, "Texture and anisotropy in the mechanical properties of titanium alloys caused by the mechanism of plastic deformation," *Russian Metallurgy (Metally)*, vol. 2007, no. 5, pp. 387–393, 2007.

[63] A. Salem, S. Kalidindi, and S. Semiatin, "Strain hardening due to deformation twinning in α-titanium: constitutive relations and crystal-plasticity modeling," *Acta Mat.*, vol. 53, no. 12, pp. 3495–3502, 2005.

[64] X. Wu, S. R. Kalidindi, C. Necker, and A. A. Salem, "Prediction of crystallographic texture evolution and anisotropic stress–strain curves during large plastic strains in high purity α-titanium using a taylor-type crystal plasticity model," *Acta Mat.*, vol. 55, no. 2, pp. 423–432, 2007.

[65] B. Hutchinson, J. Jain, and M. Barnett, "A minimum parameter approach to crystal plasticity modelling," *Acta Mat.*, vol. 60, no. 15, pp. 5391–5398, 2012.

[66] E. Anderson, D. Jillson, and S. Dunbar, "Deformation mechanisms in alpha titanium," *J. Met.*, vol. 197, pp. 1191–1198, 1953.

[67] S. Zaefferer, "A study of active deformation systems in titanium alloys: dependence on alloy composition and correlation with deformation texture," *Mat. Sci. Eng. A*, vol. 344, no. 1, pp. 20–30, 2003.

[68] S. Zherebtsov, G. Salishchev, and S. Lee Semiatin, "Loss of coherency of the alpha/beta interface boundary in titanium alloys during deformation," *Phil. Mag. Lett.*, vol. 90, no. 12, pp. 903–914, 2010.

[69] X. Chen and S. S. Mao, "Titanium dioxide nanomaterials: synthesis, properties, modifications, and applications," *Chem. Rev.*, vol. 107, no. 7, pp. 2891–2959, 2007.

[70] http://hdl.handle.net/11115/244.

[71] G. Kresse and J. Hafner, "Ab initio molecular dynamics for liquid metals," *Phys. Rev. B*, vol. 47, pp. 558–561, Jan 1993.

[72] G. Kresse and J. Hafner, "Ab initio molecular-dynamics simulation of the liquid-metal–amorphous-semiconductor transition in germanium," *Phys. Rev. B*, vol. 49, pp. 14251–14269, May 1994.

[73] G. Kresse and J. Furthmüller, "Efficiency of ab-initio total energy calculations for metals and semiconductors using a plane-wave basis set," *Comput. Mat. Sci.*, vol. 6, no. 1, pp. 15–50, 1996.

[74] G. Kresse and J. Furthmüller, "Efficient iterative schemes for ab initio total-energy calculations using a plane-wave basis set," *Phys. Rev. B*, vol. 54, pp. 11169–11186, Oct 1996.

[75] P. E. Blöchl, "Projector augmented-wave method," *Phys. Rev. B*, vol. 50, pp. 17953–17979, Dec 1994.

[76] G. Kresse and D. Joubert, "From ultrasoft pseudopotentials to the projector augmented-wave method," *Phys. Rev. B*, vol. 59, pp. 1758–1775, Jan 1999.

[77] J. P. Perdew, K. Burke, and M. Ernzerhof, "Generalized gradient approximation made simple," *Phys. Rev. Lett.*, vol. 77, pp. 3865–3868, Oct 1996.

[78] R. D. J. III, "NIST computational chemistry comparison and benchmark database, NIST standard reference database number 101, release 16a," August 2013. http://cccbdb.nist.gov/.

[79] M. J. Chase, C. Davies, J. J. Downey, D. Frurip, R. McDonald, and A. Syverud, "NIST JANAF thermochemical tables 1985 version 1.0, NIST standard reference database number 13," 1985. http://kinetics.nist.gov/janaf.

[80] Y. Mishin, M. Mehl, D. Papaconstantopoulos, A. Voter, and J. Kress, "Structural stability and lattice defects in copper: Ab initio, tight-binding, and embedded-atom calculations," *Phys. Rev. B*, vol. 63, no. 22, p. 224106, 2001.

[81] S. Shang, A. Saengdeejing, Z. Mei, D. Kim, H. Zhang, S. Ganeshan, Y. Wang, and Z. Liu, "First-principles calculations of pure elements: Equations of state and elastic stiffness constants," *Comput. Mat. Sci.*, vol. 48, no. 4, pp. 813–826, 2010.

[82] S. Ganeshan, S. Shang, Y. Wang, and Z.-K. Liu, "Effect of alloying elements on the elastic properties of Mg from first-principles calculations," *Acta Mat.*, vol. 57, no. 13, pp. 3876–3884, 2009.

[83] A. Wang, S. Shang, Y. Du, Y. Kong, L. Zhang, L. Chen, D. Zhao, and Z. Liu, "Structural and elastic properties of cubic and hexagonal TiN and AlN from first-principles calculations," *Comput. Mat. Sci.*, vol. 48, no. 3, pp. 705–709, 2010.

[84] M. I. Baskes, "Application of the embedded-atom method to covalent materials: A semiempirical potential for silicon," *Phys. Rev. Lett.*, vol. 59, pp. 2666–2669, Dec 1987.

[85] M. I. Baskes, J. S. Nelson, and A. F. Wright, "Semiempirical modified embedded-atom potentials for silicon and germanium," *Phys. Rev. B*, vol. 40, pp. 6085–6100, Sep 1989.

[86] M. Baskes, "Modified embedded-atom potentials for cubic materials and impurities," *Phys. Rev. B*, vol. 46, pp. 2727–2742, Aug 1992.

[87] M. Baskes and R. Johnson, "Modified embedded atom potentials for HCP metals," *Modell. Simul. Mater. Sci. Eng.*, vol. 2, no. 1, p. 147, 1994.

[88] B.-J. Lee and M. Baskes, "Second nearest-neighbor modified embedded-atom-method potential," *Phys. Rev. B*, vol. 62, no. 13, p. 8564, 2000.

[89] B.-J. Lee, M. Baskes, H. Kim, and Y. K. Cho, "Second nearest-neighbor modified embedded atom method potentials for BCC transition metals," *Phys. Rev. B*, vol. 64, no. 18, p. 184102, 2001.

[90] S. Plimpton, "Fast parallel algorithms for short-range molecular dynamics," *J. Comput. Phys.*, vol. 117, no. 1, pp. 1–19, 1995.

[91] Y.-M. Kim, B.-J. Lee, and M. Baskes, "Modified embedded-atom method interatomic potentials for Ti and Zr," *Phys. Rev. B*, vol. 74, no. 1, p. 014101, 2006.

[92] M. Baskes, "Modified embedded atom method calculations of interfaces," Tech. Rep. SAND–96-8484C; CONF-9603153–1, Sandia National Laboratories Livermore, USA, 1996. http://www.osti.gov/scitech/biblio/224267.

[93] Y.-M. Kim and B.-J. Lee, "Modified embedded-atom method interatomic potentials for the Ti–C and Ti–N binary systems," *Acta Mat.*, vol. 56, no. 14, pp. 3481–3489, 2008.

[94] B.-J. Lee, T.-H. Lee, and S.-J. Kim, "A modified embedded-atom method interatomic potential for the Fe–N system: A comparative study with the Fe–C system," *Acta Mat.*, vol. 54, no. 17, pp. 4597–4607, 2006.

[95] B.-J. Lee, "A modified embedded-atom method interatomic potential for the Fe–C system," *Acta Mat.*, vol. 54, no. 3, pp. 701–711, 2006.

[96] L. S. Marques, A. Fernandes, F. Vaz, M. Ramos, *et al.*, "Influence of oxygen addition on the structural and elastic properties of TiC thin films," *Plasma Proc. Poly.*, vol. 4, no. S1, pp. S195–S199, 2007.

[97] B. Jiang, G. Zhou, K. Huang, J. Hou, S. Jiao, and H. Zhu, "Structural stability of β-TiO with disordered vacancies: A first-principles calculation," *Phys. B: Cond. Matt.*, vol. 421, pp. 110–116, 2013.

[98] Y. O. Ciftci, Y. Ünlü, K. Colakoglu, and E. Deligoz, "The structural, thermodynamical and elastic properties of TiO," *Phys. Scripta*, vol. 80, no. 2, p. 025601, 2009.

[99] R. Ahuja, O. Eriksson, J. Wills, and B. Johansson, "Structural, elastic, and high-pressure properties of cubic TiC, TiN, and TiO," *Phys. Rev. B*, vol. 53, no. 6, p. 3072, 1996.

[100] R. Chauhan, S. Singh, and R. K. Singh, "Structural stability of TiO and TiN under high pressure," *Central Eur. J. Phys.*, vol. 6, no. 2, pp. 277–282, 2008.

[101] D. Watanabe, J. Castles, A. Jostsons, and A. Malin, "The ordered structure of TiO," *Acta Crystallogr.*, vol. 23, no. 2, pp. 307–313, 1967.

[102] S. Andersson, "The crystal structure of the so-called delta titanium oxide and its structural relations to the omega phases of some binary alloy systems of titanium," *Acta Chem. Scand.*, vol. 13, pp. 415–419, 1959.

[103] P. Waldner and G. Eriksson, "Thermodynamic modelling of the system titanium-oxygen," *CALPHAD*, vol. 23, no. 2, pp. 189–218, 1999.

[104] H. H. Wu and D. R. Trinkle, "Direct diffusion through interpenetrating networks: Oxygen in titanium," *Phys. Rev. Lett.*, vol. 107, no. 4, p. 045504, 2011.

[105] G. Henkelman, B. P. Uberuaga, and H. Jónsson, "A climbing image nudged elastic band method for finding saddle points and minimum energy paths," *J. Chem. Phys.*, vol. 113, p. 9901, 2000.

[106] G. Henkelman and H. Jónsson, "Improved tangent estimate in the nudged elastic band method for finding minimum energy paths and saddle points," *J. Chem. Phys.*, vol. 113, p. 9978, 2000.

[107] D. Sheppard, P. Xiao, W. Chemelewski, D. D. Johnson, and G. Henkelman, "A generalized solid-state nudged elastic band method," *J. Chem. Phys.*, vol. 136, p. 074103, 2012.

[108] W. Tang, E. Sanville, and G. Henkelman, "A grid-based Bader analysis algorithm without lattice bias," *J. Phys.: Condens. Matter*, vol. 21, no. 8, p. 084204, 2009.

[109] "Transition state tools for VASP." http://theory.cm.utexas.edu/vasp.

[110] S. Yamaguchi, "Interstitial order-disorder transformation in the Ti-O solid solution. I. ordered arrangement of oxygen," *J. Phys. Soc. Jap.*, vol. 27, pp. 155–163, 1969.

[111] A. D. Mah, K. Kelley, N. L. Gellert, E. King, and C. O'Brien, "Thermodynamic properties of titanium-oxygen solutions and compounds," Tech. Rep. 5316, Bureau of Mines, 1955.

[112] C. E. Rice and W. R. Robinson, "High-temperature crystal chemistry of Ti_2O_3: Structural changes accompanying the semiconductor-metal transition," *Acta Crystallogr. B*, vol. 33, no. 5, pp. 1342–1348, 1977.

[113] C. J. Howard, T. M. Sabine, and F. Dickson, "Structural and thermal parameters for rutile and anatase," *Acta Crystallogr. B*, vol. 47, no. 4, pp. 462–468, 1991.

[114] P. Kwasniak, M. Muzyk, H. Garbacz, and K. Kurzydlowski, "Influence of oxygen content on the mechanical properties of hexagonal Ti - first principles calculations," *Mat. Sci. Eng.: A*, vol. 590, pp. 74–79, 2014.

[115] F. Bregolin, M. Behar, and F. Dyment, "Diffusion study of 18o implanted into α-ti using the nuclear resonance technique," *Appl. Phys. A*, vol. 86, no. 4, pp. 481–484, 2007.

[116] Z. Liu and G. Welsch, "Literature survey on diffusivities of oxygen, aluminum, and vanadium in alpha titanium, beta titanium, and in rutile," *Met. Trans. A*, vol. 19, no. 4, pp. 1121–1125, 1988.

[117] W. Joost, S. Ankem, and M. Kuklja, "A modified embedded atom method potential for the titanium–oxygen system," *Mod. Sim. in Mat. Sci. and Eng.*, vol. 23, no. 1, p. 015006, 2015.

[118] A. Stukowski, "Visualization and analysis of atomistic simulation data with OVITO–the open visualization tool," *Modelling and Simulation in Materials Science and Engineering*, vol. 18, no. 1, p. 015012, 2010.

[119] G. Welsch, R. Boyer, and E. Collings, *Materials properties handbook: titanium alloys*. ASM international, 1993.

[120] T. Braisaz, P. Ruterana, G. Nouet, and A. Serra, "High-resolution electron microscopy study of the (1012) twin and defects analysis in deformed poly-crystalline alpha titanium," *Phil. Mag. Lett.*, vol. 74, no. 5, pp. 331–338, 1996.

[121] R. Bunshah, "Rates of deformation twinning in metals," in *Proceedings of the Conference on Deformation Twinning* (R. Reed-Hill, J. Hirth, and H. Rogers, eds.), pp. 390–392, TMS, 1964.

[122] M. V. Klassen-Neklyudova, *Mechanical twinning of crystals*. New York: Consultants Bureau, 1964.

[123] M. Niewczas, "Lattice correspondence during twinning in hexagonal close-packed crystals," *Acta Mat.*, vol. 58, no. 17, pp. 5848–5857, 2010.

[124] J. H. Rose, J. R. Smith, F. Guinea, and J. Ferrante, "Universal features of the equation of state of metals," *Phys. Rev. B*, vol. 29, no. 6, p. 2963, 1984.